COHERENT ELASTIC NEUTRINO NUCLEUS SCATTER RESPONSE OF SEMICONDUCTOR DETECTORS TO NUCLEAR REACTOR ANTINEUTRINOS AND SAFEGUARDS APPLICATIONS

A Dissertation

by

WEI ENG ANG

Submitted to the Graduate and Professional School of
Texas A&M University
in partial fulfillment of the requirements for the degree of

DOCTOR OF PHILOSOPHY

Chair of Committee,	Shikha Prasad
Committee Members,	Sunil S. Chirayath
	Craig Marianno
	Rupak Mahapatra
Head of Department,	Michael Nastasi

May 2022

Major Subject: Nuclear Engineering

ABSTRACT

In this work, semiconductor CEνNS detector response to reactor antineutrinos is studied. In particular, pulse height distributions and reaction rates are used for nonproliferation and power-monitoring analysis of a research and commercial reactor. The antineutrino spectrum of ^{235}U, ^{238}U, ^{239}Pu, and ^{241}Pu are modeled using summation method with corrections for the finite-size-nucleus, weak magnetism, and radiative losses. The modeled antineutrino spectrum is also compared to previous studies using the summation and conversion methods from the literature to validate the results.

Following the antineutrino spectrum modeling, the CEνNS and IBD cross-sections are calculated. The cross-sections are later used to calculate the detector response in terms of CEνNS-IBD detector reaction rates. Detector measurables such as distribution of recoil energies for a given incident antineutrino energy or CEvNS pulse height distribution for a threshold, detector size, and distance are also calculated to investigate the importance of background levels and resolution on antineutrino spectroscopy for nuclear security applications and nuclear physics studies.

The findings suggest that a CEνNS detector made of natural Ge with a mass of 100-kg and 20-eV$_{NR}$ thresholds is over 27 times more efficient compared to the IBD detector, and over 2 times more efficient compared to the Si detector. The results show that a threshold of 20-eV$_{NR}$ renders 33% of antineutrinos from a 1-MW TRIGA reactor undetected in natural Ge and 20% of antineutrinos undetectable in natural Si. In both natural Ge and natural Si, increasing the threshold to 100-eV$_{NR}$ renders 67% and 46% of

antineutrinos undetected, respectively. The current IBD threshold leaves 66% of the antineutrino population undetected.

A CEνNS Ge detector can be used to detect antineutrinos outside the AP1000-type reactor containment with 1,977 events/day, given a 100-$\mathrm{eV}_{\mathrm{NR}}$ threshold and background levels of 100-DRU can be achieved. The diversion detection is difficult with detection probability less than 7% when the operator intervenes and recovers the reactor power, or when the diverted fuel assemblies are substituted with fresh fuel assemblies. For the case of diversion without operator intervention by reducing reactor power, removing three or more fuel assemblies can be detected with detection probabilities of more than 30%.

ACKNOWLEDGEMENTS

I would like to thank my committee chair, Dr. Shikha Prasad, and my committee members, Dr. Sunil S. Chirayath, Dr. Craig Marianno, and Dr. Rupak Mahapatra, for their guidance and unwavering support at every stage of the research project.

Thanks also to my friends and colleagues, as well as the faculty and staff of the department, for making my time at Texas A&M University so enjoyable.

I'd like to thank my mother and late father and for their support. Finally, I would like to extend my sincere gratitude to my wife for her patience and support. It would have been difficult for me to finish my studies without her wonderful understanding and encouragement throughout the last few years.

CONTRIBUTORS AND FUNDING SOURCES

Contributors

This work was supervised by a dissertation committee consisting of Professor Shikha Prasad [advisor], Professor Sunil Chirayath, Professor Craig Marianno of the Department of Nuclear Engineering, and Professor Rupak Mahapatra of the Department of Physics and Astronomy.

The analyses depicted in Chapter 3 and Chapter 4 were published in 2021 and 2022.

All other work conducted for the dissertation was completed by the student independently.

Funding Sources

Graduate study was supported by a graduate assistantship funded by the Department of Nuclear Engineering from Texas A&M University. In addition, this graduate study was also supported by T3 (Texas A&M University) Round 4, and Texas A&M Engineering Experiment Station.

NOMENCLATURE

CEνNS	Coherent Elastic Neutrino-Nucleus Scattering
CSA	Comprehensive Safeguards Agreement
DA	Destructive Assays
DOE	U.S. Department of Energy
DRU	Differentiate Rate Unit
DUNE	Deep Underground Neutrino Experiment
FP	Fission Product
GDLS	Gadolinium-doped Liquid Scintillator
IAEA	International Atomic Energy Agency
ILL	Institut Laue-Langevin
IBD	Inverse Beta Decay
MCNP	Monte Carlo N-Particle Transport Code
MINER	Mitchell Institute Neutrino Experiment at Reactor
NC	Neutral Current
NDA	Non-Destructive Assays
NPT	Nuclear Non-Proliferation Treaty
ORNL	Oak Ridge National Laboratory
PMT	Photomultiplier Tube
PROSPECT	Precision Reactor Oscillation and Spectrum Experiment
SM	Standard Model

SNS	Spallation Neutron Source
SQ	Significant Quantity
TAGS	Total Absorption Gamma Spectroscopy
TAMU	Texas A&M University
TEXONO	Taiwan Experiment on Neutrino
TRIGA	Training, Research, Isotopes, General Atomic Reactor
ZIP	Z-sensitive Ionization and Phonon
SuperCDMS	Super Cryogenic Dark Matter Search

TABLE OF CONTENTS

Page

LIST OF FIGURES

Page

LIST OF TABLES

Page

1. INTRODUCTION

1.1. Background

1.1.1. Antineutrino production from fission and capture event

Antineutrinos are subatomic particles that have an infinitely tiny mass (less than 1 eV/c^2) and no electrical charge [1]. Antineutrinos can be produced via a number of radioactive decays such as beta decay reaction by the atomic nuclei, particle accelerators, and others. They are typically produced in nuclear reactors in beta minus decays of fission product isotopes when fissionable actinides such as ^{235}U undergo fission. Among these fission products, some will go on to undergo a type of radioactive decay called beta minus decay.

$$ {}^{A}_{Z}X \rightarrow {}_{Z+1}^{\;\;A}Y + e^{-} + \bar{\nu}_e \qquad (1\text{-}1) $$

In this process, the neutron emitted from a fission fragment is converted into a proton, an electron, and an electron antineutrino. Antineutrinos can travel through the shielding that surrounds a nuclear reactor core, as they have a high penetrating power. The number of antineutrinos produced in a nuclear reactor is determined by the reactor's power level and the fissioning isotopes.

In a reactor, antineutrinos also can also be produced from capture events. For example, a ^{238}U can capture a neutron to transmute into ^{239}U. Then, ^{239}U will beta decay into ^{239}Np; and ^{239}Np further beta decays into ^{239}Pu. Two antineutrinos can be produced from a ^{238}U neutron capture event. In a fission event, ^{235}U, ^{238}U, ^{239}Pu, and ^{241}Pu produce roughly 6.08, 7.17, 5.51, and 6.26 antineutrinos per fission, respectively.

1.1.2. Antineutrino detection

There are several methods to detect antineutrinos; and one of them is inverse beta decay (IBD)as shown in Eq. 1-2.

$$\bar{\nu}_e + p \rightarrow e^+ + n \tag{1-2}$$

IBD describes a process where an electron antineutrino interacts with a proton and produces a neutron and positron. IBD can only detect neutrinos over a threshold of 1.806 MeV [2]. The IBD detectors are generally large due to their low cross-section. Kamioka liquid scintillator antineutrino detector, has been used by Kamioka Observatory to detect antineutrinos via IBD mechanism [3] . The Precision Reactor Oscillation and Spectrum Experiment (PROSPECT) at the Department of Energy's (DOE) Oak Ridge National Laboratory (ORNL) are also another one of the experiments that use 4 tons lithium-loaded liquid scintillator utilizing IBD mechanism to study antineutrino [4]. In Daya Bay experiment, gadolinium-doped liquid scintillator (GdLS) is used for antineutrino detection study [5]. Lastly, the Double Chooz experiment located in France also detects antineutrinos, using the GdLS detector which relies on IBD [6].

The second antineutrino detection method is coherent elastic neutrino-nucleus scattering process (CEνNS). The CEνNS is a process that has been predicted by Freedman in 1974 but was not observed until 2017 [7]. In this fundamental process, an antineutrino can interact with the nucleus to produce low nuclear recoil energy, which later collects signals for antineutrino measurement. The cross-section of CEνNS has a quadratic dependence on the number of neutrons of the target material [8]. One of the advantages of CEνNS based detectors over the conventional detectors is that the size of CEνNS based detectors are small in general. For example, the cryogenic semiconductor detector developed by the Mitchell Institute Neutrino Experiment at Reactor (MINER) weighs only 10 kg [9]. Additionally, there is no minimum energy threshold for the CEνNS reaction. Thus, detectors that utilized CEνNS can offer a better alternative because of its small detector size, portability, and low energy threshold compared to a conventional detector. Several experiments have been established to study CEνNS reaction using reactor antineutrinos such as COHERENT, MINER, TEXONO, CONNIE, NU-CLEUS, RICOCHET, RED100, CONUS, and DAMIC [10] [11] [12] [13] [14] [15] [16] [17] [18]. The COHERENT collaboration at ORNL has developed several detectors using different technologies to observe CEνNS using the Spallation Neutron Source (SNS) facility. By using 1 GeV per proton generated from an accelerator-based system, a liquid mercury target is irradiated to produce neutrons and π mesons. During the process, the π mesons will stop in the target volume and produce electron-neutrinos, muon-neutrinos, and tau-neutrinos via decay. In SNS, electron antineutrinos with energies up to 52.6 MeV can be produced [19]. Some of their detectors include CsI[Na] scintillator detector, CENNS-10 single-phase liquid Ar detector, NaI[Tl] scintillator detector, and P-type contact germanium detector [20].

The CsI[Na] scintillator detector was the first detector that observed CEνNS for the first time in 2017 and was later confirmed with liquid Ar detector. Both CsI[Na] and liquid Ar are good candidates for CEνNS target material because of their high light yield, with 64 photons/keVee, and 40 photons/keVee, respectively. The liquid Ar detector has another property where it has two energy states, which can use pulse shape discrimination to separate the nuclear recoil signal from the background. However, the downside to these detectors is their relatively high recoil energy threshold, being 6.5 keV_{NR} and 20 keV_{NR}, respectively [20]. Also, the source of Ar is usually contaminated with ^{39}Ar, which is produced by cosmic rays and can affect the measurement of the detector.

MINER experiment utilizes cryogenic germanium and silicon detectors technology to detect antineutrinos, using 1 MW(th) TRIGA research reactor located at Nuclear Science Center, Texas A&M University [21]. The MINER collaboration has developed several detectors such as Interleaved, Z-dependent Ionization and Phonon Detector (iZIP), and HV-type detectors. The iZIP-type detector has the ability to discriminate nuclear and electron recoils via phonon and charge production. On the other hand, the HV-type detector doesn't have discrimination ability and is used to measures charge production indirectly through amplified phonon production [11].

Taiwan Experiment on Neutrino (TEXONO) is another collaboration that studied CEνNS located at the Kuo-Sheng Reactor Neutrino Laboratory in Taiwan. TEXONO uses high purity GE as the target detectors for the CEνNS study. Some of their detectors include high purity Ge, n-type Ge detector (ULEGE), p-type point-contact Ge detector (pPCGe), and n-type point-contact Ge (nPCGe) detector. The analysis threshold for the nPCGe is approximately 300 eV_{NR} and weighs about 500g [12].

Coherent Neutrino-Nucleus Interaction Experiment (CONNIE) at Brazil focuses on Charge Coupled Devices (CCD) technology with silicon nuclei to detect CEvNS with very low thresholds (of order ~10 eV). The CCDs are stacked in a high purity copper box and cooled to a temperature of -124^{0}C inside the detector [13]. The CONNIE experiment is located at 3.95 GWth Angra-II reactor of the Almirante Alvaro Alberto nuclear power plant in Angra dos Reis, reactor building. Similarly, CCD is also used in the DAMIC experiment at Canada's SNOLAB facility to look for dark matter interactions [18]. It is worth noting that experiments such as NUCLEUS (France), RICOCHET (France), and RED100 (Russia) have different technologies to study CEνNS, such as cryogenic calorimeter, bolometer, and liquid xenon. NUCLEUS detectors use cryogenic calorimeter technology with the target materials such as $CaWO_4$, Al_2O_3, Ge, and Si. The NUCLEUS experiment has simulated that a gram-scale Al_2O_3 detector has a recoil energy threshold of 20 eV_{NR}, which required a minimum incident antineutrino energy of 0.50 MeV [14]. RICOCHET is another CEνNS experiment located at Chooz Nuclear power plant. They focus on the detector that is composed of both Ge and metallic Zn with a total mass of 10 kg using the bolometer principle. The recoil energy threshold of the bolometer-based detector is about 50 eV_{NR}, which can detect incident antineutrino energy of 1.30 MeV [15]. The XENON100 detector, developed by the RED-100 experiment in Russia, contains 100 kg of liquid Xenon with a recoil energy threshold of 300 eV_{NR}, which requires a minimum antineutrino energy of 4.28 MeV to trigger the recoil [16]. Lastly, the CONUS experiment located in Brokdorf nuclear power plant located, Germany uses a 4 kg Ge semiconductor with 300 eV_{NR} threshold to study the CEνNS [17].

Overall, semiconductor-based CEνNS based detectors are widely used in the CEνNS experiments and have a relatively low energy threshold and weight compared to scintillator-based CEνNS detectors. Therefore, this research will focus on the application of the semiconductor-based CEνNS based detectors because scintillation-based CEνNS detectors developed at this time, have a very high nuclear recoil energy threshold. The detector response comparison of semiconductor-based and scintillator-based detector can be found in section 1.3.1.

Lastly, antineutrino can be detected using the antineutrino-electron scattering mechanism, first observed by Gargamelle bubble chamber in 1973 [22]. The CHARM is one of the collaborations that study the neutrino-electron scattering event using a CHARM-II detector [23]. However, antineutrino-electron scattering is beyond the scope of this work and therefore will not be discussed. The BOREXINO experiment, which is housed at the Laboratori Nazionali del Gran Sasso, was another collaboration utilizing antineutrino-electron scattering mechanism to detect solar neutrinos [24].

1.1.3. Safeguards and IAEA requirements

The IAEA has established significant quantities (SQ) for its detection goals. It is defined as the amount of nuclear material for which the possibility of manufacturing a nuclear explosive device cannot be excluded. The value of the significant quantity depends on the type of nuclear material, as shown in Table 1-1 [25].

Table 1-1 Significant quantities of direct and indirect use special nuclear material.

Material	Significant Quantity
Direct use nuclear material	
Pu	8 kg
^{233}U	8 kg
HEU (^{235}U 20%)	25 kg
Indirect use nuclear material	
U (^{235}U 20%)	75 kg
Natural U	10 t
Depleted U	20 t
Th	20 t

Direct use nuclear material is defined as a nuclear material that can be utilized to make nuclear explosive devices without needing to be further enriched or transmuted. Direct use nuclear material can be further categorized into two groups: unirradiated and irradiated. Unirradiated direct use nuclear material is nuclear material that does not contain significant amounts of fission products; thus, it requires less time to convert into nuclear explosive devices. On the other hand, irradiated direct use nuclear material is nuclear material that still contains a sufficient amount of fission products, which make the conversion process longer and harder due to their high doses.

Table 1-2 The detection goals of unirradiated direct use material, irradiated direct use material, and indirect use material.

Material	Detection goals
Unirradiated direct use material	1 month
Irradiated direct use material	3 months
Indirect use material	1 year

Table 1-2 shows the detection goals of unirradiated direct use material, irradiated direct use material, and indirect use material [25]. In most cases, the plutonium and uranium contained in spent fuels of the reactor fall into the irradiated the direct use material category. Therefore, this research focuses on a 3-month detection goal for the diversion case study as discussed in Chapter 5.

It is important to understand IAEA's safeguards requirement in order to conduct nonproliferation analysis using CEvNS detector. The IAEA requires a detection probability of greater than 20% for low probability events, and 90% for high probability events. In this dissertation, the detection probability, P_{det} is calculated to determine the likelihood that IAEA will detect if a specific amount of nuclear material has been diverted. The detection probability is given an equation as below:

$$P_{det} = 1 - \beta \tag{1-3}$$

where β is the non-detection probability.

1.2. Motivation and research objectives

As discussed in section 1.1.1, the characteristic of the reactor has enabled the possibility of using antineutrinos for reactor monitoring [26]. Furthermore, antineutrinos are sensitive to a reactor's burnup, power, and enrichment. Therefore, antineutrino detectors can serve as an alternative means for nuclear fuel monitoring. One of the main characteristics of antineutrinos is that antineutrinos have a very high penetrating power. Therefore, it is possible to carry out remote/offsite monitoring on a nuclear reactor. For example, the Deep Underground Neutrino Experiment (DUNE) hosted by U.S. Department of Energy's (DOE) Fermilab has conducted antineutrino detection over a distance of 1,300 km between the detectors and a neutrino source [27].

Throughout the history of nuclear safeguards, there have been several instances when countries such as Iran and North Korea have refused or denied inspection visits to United Nations' International Atomic Energy Agency (IAEA) [28] [29]. Under those circumstances, a small portable antineutrino detector could be deployed outside the reactor site to monitor the reactor power in order to investigate any suspicious activities such as the diversion of nuclear materials. Ideally, antineutrino detectors also can be used in emergency situations such as reactor core meltdowns of the Chernobyl disaster in 1986 and the Fukushima accident in 2011, where first responders could not safely access the reactor. By deploying an antineutrino detector, the exposure risk of radiation workers or first responders can be significantly decreased [30] [31].

The study of small portable antineutrino detectors in safeguards application is not well established despite its numerous benefits due to the limitations that will be discussed in the literature review section, Section 2. This research is intended to explore that the possibility of using small, portable, high detection efficiency antineutrino detectors as one of the non-destructive assays (NDA) techniques that can be implemented in the area of safeguards and nonproliferation.

One of the main objectives of this research is to provide a preliminary study of the new antineutrino detection technology: coherent-elastic-neutrino-nucleus-scatter (CEνNS) based type detectors and investigate their application in nuclear safeguards and nonproliferation. The study also aims to compare the CEνNS based detector with a conventional antineutrino detector that uses IBD mechanism. The study will explore the possibilities of deploying a small, portable, high detection efficiency CEνNS based detector and their practical usages to various reactors. The research objectives are to:

i. Compare CEνNS semiconductor-based detector response, the CEνNS liquid scintillator-based detector, and the IBD based detector using pulse height distributions;
ii. Conduct operation analysis on operational feasibility of CEvNS such as measurement time and distance from a reactor for a given size of a detector at a specified threshold; and
iii. Assess nonproliferation measurables (in terms of significant quantities and material accounting) and sensitivity of CEνNS to burnup, isotopic composition, reactor power, and cooling time at various nuclear facilities such as a research reactor, a commercial reactor, and a nuclear spent fuel facility.

The outcomes of this study will help to determine if CEνNS based detectors can be used to effectively measure reactor antineutrinos, improve nuclear safeguards and nonproliferation detection for the IAEA, and enable reactor power monitoring without entering the reactor containment. Such applications can help in the detection of covert operations or the misuse of nuclear materials and technology.

1.2.1. Dissertation outline

Chapter 2 will discuss improvements to the antineutrino spectrum calculation using the summation method by including fission product excited states (with TAGS data when available) and other corrections. This chapter will also discuss the detector reaction rates and pulse height distributions.

Chapter 3 discusses the preliminary work of modeling the antineutrino spectrum using the approximation method. This paper provides an overview of CEvNS detection and its benefits compared to IBD using the Texas A&M 1 MW TRIGA reactor as a case study. Chapter 4 shows how a detector can be used to distinguish burnup in a commercial reactor fuel with detection probabilities and compare to the IAEA requirements.

Lastly, Chapter 5 will discuss the results of diversion cases from a reactor core by providing the detection probabilities for each case. The diversion cases are diversion with operator intervention, without operator intervention, and substitution with fresh fuel. This chapter will also provide the detection probability for the case where power is reduced without any diversion. Lastly, this chapter will provide the antineutrino spectrum of the reactor fuel 1 day, 1 week, 1 month, 1 year, and 10 years after shutdown.

1.3. Literature review and previous work

1.3.1. Detection mechanism of antineutrinos

In an IBD reaction, the antineutrino will interact with a proton to produce a positron and neutron. This process requires a minimum energy of 1.806 MeV to trigger the process. The detection principle of IBD is based on the coincidence measurement of 511 keV from positron annihilation and neutron capture reaction. During the positron annihilation, 511 keV photon will be emitted and yield the prompt photon. Following the positron annihilation, the neutrons are captured by the protons of the material, giving a delayed photon [32]. This delayed coincidence provides the signature of IBD and allows discrimination from the background.

In this dissertation, the detector responses are calculated in terms of nuclear recoil energy. The calculation such as phonon energy and charge energy produced from the CEνNS interaction is beyond the scope of the study. However, the general CEνNS detection mechanism using semiconductor-based and liquid scintillator-based CEνNS detectors is discussed here for a better understanding of the CEνNS interaction. when an antineutrino enters the CEνNS detector, two types of energy will be produced: phonon energy and charge energy. For phonon energy, the primary phonon energy is created when the energy is deposited directly into the crystal lattice. This energy vibrates through the crystal and creates secondary phonons. At the same time, the charge energy also creates more secondary phonons (also called as Neganov-Trofimov-Luke [NTL] phonons) as the motion of charges are accelerated due to the bias voltage. The phonon energy is usually collected by Transitioning Edge Sensors (TES) [26].

For charge energy, the energy of the particle will be deposited inside the detector. Then, the electrons will be liberated from the atoms and produce electron-hole pairs. Due to the bias voltage, those electron-hole pairs are accelerated and create more electron-hole pairs. At the end of the detector, charge is collected. During the acceleration of electron-hole pairs, more phonons are also created as secondary phonons, which further contribute to the phonon energy. The charge energy is collected by a field-effect transistor (FET).

Some of the semiconductor CEνNS based detectors has the ability to discriminate between an electron recoil or nuclear recoil. Generally, ionization yield, which is the ratio of the measured charge and phonon recoil energy, is used to differentiate electron recoil and nuclear recoil events. Electron recoil interaction is mainly caused by background radiation such as electrons, photons, and muons. Electron recoil event happens when an electron in the lattice is liberated from the lattice and creates electron-holes pairs. In an electron recoil interaction, charge energy is approximately the same as phonon energy. On the other hand, nuclear recoil is an interaction where neutral particles such as a neutron or a neutrino interacts with the nuclei, inducing vibrations propagating as phonon. In a nuclear recoil interaction, only a few electron-holes can be created from the primary phonon: thus the charge energy is lower than phonon energy, thus lowering the ionization yield [33].

In scintillators, the CEνNS the detection mechanism is slightly different. There are two ways in which the scintillation process can occur when an antineutrino deposits its energy in a scintillator. First, the atom of the scintillator can be excited and then de-excited to emit scintillation photons. Secondly, the antineutrino can deposit its energy to the atoms of the scintillator and ionization occurs. During the ionization process, electrons will be emitted. The ionized atoms will eventually recombine with emitted electrons and undergo a de-excitation process leading to scintillation photon emission. This process is also called recombination. As the liquid scintillator such as argon excites into the single or triplet stage, the difference of singlet/triplet ratio can be used to discriminate between nuclear recoil and electron recoil events [34].

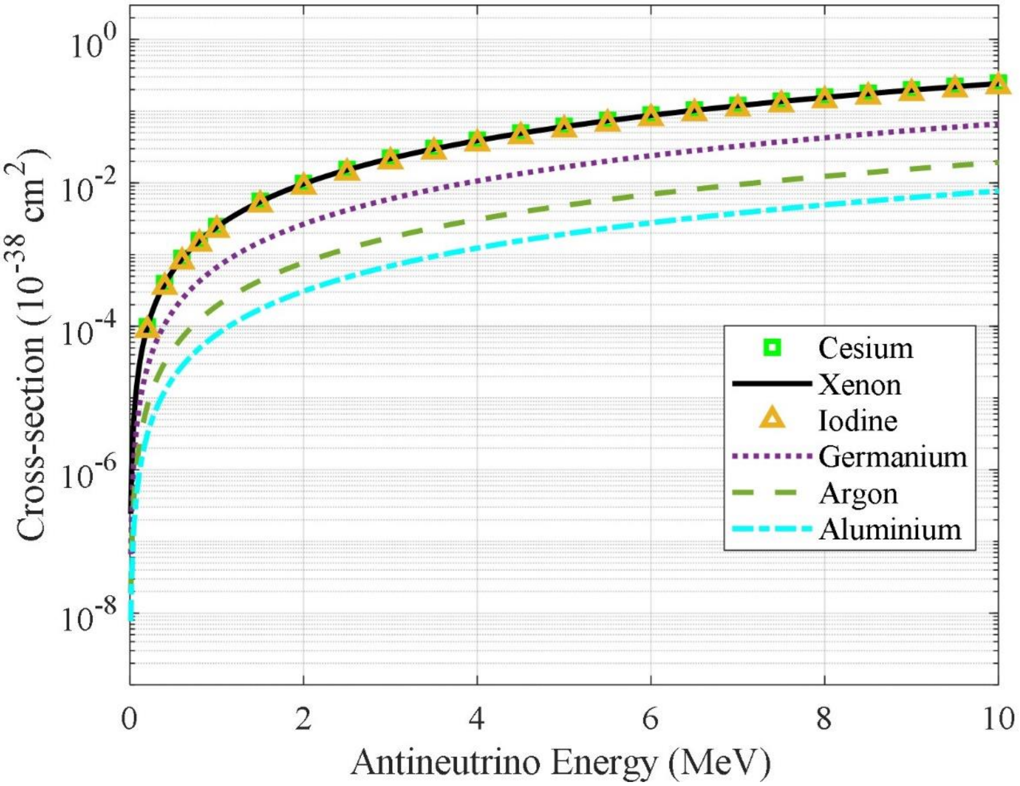

Figure 1-1 The CEνNS cross-section of cesium, xenon, iodine, germanium, argon and silicon.

Figure 1-1 shows the example of CEνNS for some of the materials discussed in section 1.1.2. Overall, the higher the atomic mass number, the higher its cross-section. Detailed CEνNS cross-section calculation can be found in section 1.3.2 and Chapter 2. The flux weighted average cross-section for cesium (Cs), xenon (Xe), iodine (I), germanium (Ge), argon (Ar), and silicon (Si) are 1.61 x 10^{-39} cm^2, 1.59 x 10^{-39} cm^2, 1.45 x 10^{-39} cm^2, 4.35 x 10^{-40} cm^2, 1.26 x 10^{-40} cm^2, and 5.09 x 10^{-41} cm^2, respectively. Of these, Cs has the highest flux weighted average cross-section and has the highest atomic mass number among the others; while Si has the lowest flux weighted average cross-section.

Table 1-3 The nuclear recoil threshold and required minimum antineutrino energy of targeted material in CEvNS process.

Material	Nuclear recoil threshold (eV_{NR})	Minimum antineutrino required
CsI	6,500	20.06 MeV (Cs) 19.60 MeV (I)
Xe	300	4.28 MeV
Ge	100	1.84 MeV
Ar	20,000	19.30 MeV
Si	50	0.82 MeV

Table 1-3 shows typical nuclear recoil thresholds and required minimum antineutrino energies for various detection materials in the CEvNS process. CsI[Na] was the first to be used in CEvNS detection, which has a 6,500 eV_{NR} threshold which is not suitable for use in reactor core monitoring at this threshold because the minimum antineutrino energy required for detection is 19.60 MeV for iodine and 20.06 MeV for Cs. Argon is another detection material that is also not suitable for reactor antineutrino monitoring at present because it requires a minimum energy of 19.30 MeV for a 20,000 eV_{NR} threshold. Germanium, Xe, and Si are the better candidates as the required minimum antineutrino energies for detection are low. This is because the average antineutrino energies in the reactor is between 0.54 MeV to 1.65 MeV, depending on the antineutrino production from the fissionable isotopes. Next, the parameters used in detector response comparisons are shown in Table 1-4. The detailed calculations of the detector response can be found in Chapter 2 and Chapter 4.

Table 1-4 AP1000 parameters for detector response calculation.

Parameters		Values
Reactor		AP1000 type reactor
Fission rate		1.0474 x 10^{20} s^{-1}
Detector distance from the core		25 m
Fission Fraction	^{235}U	0.7621
	^{238}U	0.0638
	^{239}Pu	0.1496
	^{241}Pu	0.0244
	^{238}U to ^{239}Pu	0.5534

Table 1-5 Gross counts, counts with threshold, and net counts with threshold and 100 DRU background for each detection material.

Material	Gross counts (Events/day)	Net counts with threshold (Events/day)	Net counts with threshold and 100 DRU background (Events/day)
CsI	28,278.64	0	0
Xe	29,034.64	938.30	0
Ge	14,381.95	5,606.16	1,977.33
Ar	7,595.46	0	0
Si	4,355.90	3,355.59	83.98

Table 1-5 shows the gross counts, net counts with threshold, and net counts with threshold and 100 DRU for each detection material. Although Xe has the highest gross count with 2,8278.64 events/day, the potential of Xe was limited by the current threshold limitation, which only allows energy above 4.28 MeV to be detected resulting in only 938,30 events/day. Both CsI and Ar also have a very high threshold, thus it is not possible to detect antineutrinos from the regular reactor. Ge and Si are more suitable for detecting reactor antineutrinos as they have relatively low thresholds compared to CsI, Xe, and Ar. When applying 100 DRU to the detector response, Ge and Si are still able to detect antineutrinos with 1,977.33 events and 83.98 events. The comparisons above have shown that the detector responses are highly affected by the detector threshold and background. Thus, a low threshold detector and low background noise are highly favorable in order to improve detection efficiency. In this work, Ge and Si are mainly used as a case study.

1.3.2. Calculation of the antineutrino spectrum

One can model the reactor antineutrino spectrum using either the "ab-initio" summing approach or the beta spectrum conversion method. The summation method uses information from nuclear data libraries to predict the reactor antineutrino spectrum. First, antineutrino spectra of all contributing fission products from ^{235}U, ^{238}U, ^{239}Pu, and ^{241}Pu are modeled and later summed together to form a total reactor antineutrino spectrum. The benefit of the summation method is this method can be used to construct low-energy antineutrino spectra. However, there are also large uncertainties in the cumulative yield, Q values, beta intensities, and the pandemonium effect tampering with the spectrum discussed in Chapter 2. Vogel *et al.* (1985) and Hayes *et al.* (2016) has modeled the reactor antineutrino spectra using the summation approach [35] [36]. Vogel *et al.* has also used the summation method to predict the antineutrino spectrum arising from both thermal and fast fissions.

On the other hand, the beta spectrum conversion method requires experimentally determined beta spectrum and converting it into the antineutrino spectrum. The beta spectra are obtained from the Institut Laue-Langevin (ILL) in Grenoble, France. As the individual branch information is not accessible from the observed integral beta spectrum, Schreckenbach *et al*. developed a method by dividing the beta spectrum into 30 virtual branches. The virtual branches here can also be referred to as beta intensities of excited states as the beta spectrum is continuous, the Q-values are different for each excited state. Once the virtual branches have been obtained from the beta spectrum, the total antineutrino spectrum can be calculated by adding all 30 virtual antineutrino spectra. Mueller *et al.* (2011) and Huber *et al.* (2011) have used the conversion approach to predict antineutrino spectra for ^{235}U, ^{239}Pu, and ^{241}Pu [37] [38]. The conversion approach is relatively more accurate but only available for the energy range of 2 to 8 MeV. Haag *et* (2013) *al.* has demonstrates the antineutrino spectrum of ^{238}U using conversion approach [39].

Ishimoto *et al*. (2002) created an estimation method to model antineutrino without including the transitions of fission products. Alternatively, they introduced a correction factor, that modified the spectrum to make it match with the other experimental antineutrino spectra [40]. The detailed discussion of antineutrino spectrum modeling comparison using summation method, conversion, and approximation method can be found in Chapter 2.

1.3.3. The CEvNS cross-section calculation

CEvNS has been long predicted by D. Z. Freedman in 1974 and it has cross-section differential equation:

$$\frac{d\sigma(E_v)}{dT_R(E_v)} = \frac{G_F^2 M}{2\pi}\left[(q_v + q_A)^2 + (q_v - q_A)^2 \left(1 - \frac{T_R}{E_v}\right)^2 - (q_v^2 - q_A^2)\frac{MT_R}{E_v^2}\right] \qquad (1\text{-}4)$$

where G_F denotes the Fermi constant, *M* is the mass of the targeted nucleus, q_v and q_A are vector and axial charges respectively, T_R is recoil energy and E_v is the incident antineutrino energy. For most nuclei, the vector contribution is dominant; and axial contributions are minor. Axial terms can be conveniently neglected as they are small for most nuclei, and have a value of zero for nuclei that have even number of protons and neutrons. The CEvNS cross-section is proportional to N^2, the number of the nuclei, and it is larger than IBD cross-section. The comparison of CEvNS and IBD cross-section comparison with their impacts on the detector response are discussed in Chapter 3.

1.3.4. References

[1] J. Lesgourgues and S. Pastor, Neutrino Mass from Cosmology, *Advances in High Energy Physics* 2012, doi:10.1155/2012/608515.

[2] A. Oralbaev, M. Skorokhvatov, and O. Titov, The Inverse Beta Decay: A Study of Cross Section, *J. Phys.: Conf. Ser.* 675, 012003, 2016, doi:10.1088/1742-6596/675/1/012003.

[3] トップページ | Kamioka Observatory, ICRR, University of Tokyo. [Online]. Available: http://www-sk.icrr.u-tokyo.ac.jp/index-e.html.

[4] PROSPECT Collaboration et al., The PROSPECT Reactor Antineutrino Experiment, *Nuclear Instruments and Methods in Physics Research Section A: Accelerators, Spectrometers, Detectors and Associated Equipment* 922, 287, 2019, doi:10.1016/j.nima.2018.12.079.

[5] F. P. An et al., Measurement of the Reactor Antineutrino Flux and Spectrum at Daya Bay, *Phys. Rev. Lett.* 116, 061801, 2016, doi: 10.1103/PhysRevLett.116.061801.

[6] F. Suekane, A High Precision Reactor Neutrino Detector for the Double Chooz Experiment, *Nuclear Instruments and Methods in Physics Research Section A: Accelerators, Spectrometers, Detectors and Associated Equipment* 623, 440, 2010, doi: 10.1016/j.nima.2010.03.029.

[7] D. Akimov et al., Observation of Coherent Elastic Neutrino-Nucleus Scattering, *Science* 357, 1123, 2017, doi: 10.1126/science.aao0990.

[8] K. Scholberg, Observation of Coherent Elastic Neutrino-Nucleus Scattering by COHERENT, 2018. ArXiv:1801.05546 [Astro-Ph, Physics:Hep-Ex, Physics:Hep-Ph, Physics:Nucl-Ex, Physics:Physics].

[9] R. Mahapatra, MINER Coherent Neutrino Scattering with SuperCDMS Cryogenic Detector Technology, Mitchell Workshop on Collider, Dark Matter and Neutrino Physics (2016). [Online]. Available:https://indico.cern.ch/event/518614/contributions/1198829/attachments/1296922/1934207/MINER_MI_workshop.pdf.

[10] D. Akimov et al., COHERENT Experiment: Current Status, *J. Phys.: Conf. Ser*. 798, 012213, 2017, doi:10.1088/1742-6596/798/1/012213.

[11] Workshop on Fundamental Physics at the Second Target Station (FPSTS19) | Shull Wollan Center. [Online]. Available: https://conference.sns.gov/event/171/.

[12] H. T. Wong, Low Energy Neutrino and Dark Matter Physics with Sub-KeV Germanium Detectors, *J. Phys.: Conf. Ser.* 309, 012024, 2011, doi: 10.1088/1742-6596/309/1/012024.

[13] A. Aguilar-Arevalo et al., The CONNIE Experiment, *J. Phys.: Conf. Ser. 761*, 012057, 2016, doi:10.1088/1742-6596/761/1/012057.

[14] L. Thulliez et al., Calibration of Nuclear Recoils at the 100 EV Scale Using Neutron Capture, *J. Inst.* 16, P07032, 2021, doi: 10.1088/1748-0221/16/07/P07032.

[15] J. Billard et al., Coherent Neutrino Scattering with Low Temperature Bolometers at Chooz Reactor Complex, J. *Phys. G: Nucl. Part. Phys.* 44, 105101, 2017, doi: 10.1088/1361-6471/aa83d0.

[16] K. Ni, Feasibility of a Liquid Xenon Detector for Reactor Neutrino Detection via CEvNS, Magnificent CevNS 2020. [Online]. Available: https://indico.cern.ch/event/943069/contributions/4103991/attachments/2144259/3613800/Ni-CEvNS2020-Xe.pdf.

[17] J. Billard, J. Johnston, and B. J. Kavanagh, Prospects for Exploring New Physics in Coherent Elastic Neutrino-Nucleus Scattering, *J. Cosmol. Astropart. Phys.* 2018, 016, 2018, doi: 10.1088/1475-7516/2018/11/016.

[18] S. J. Lee, B. Kilminster, and A. Macchiolo, Dark Matter in CCDs at Modane (DAMIC-M): A Silicon Detector Apparatus Searching for Low-Energy Physics Processes, *J. Inst.* 15, C02050, 2020, doi: 10.1088/1748-0221/15/02/C02050.

[19] Y. Efremenko and W. R. Hix, Opportunities for Neutrino Physics at the Spallation Neutron Source (SNS), *J. Phys.: Conf. Ser.* 173, 012006, 2009, doi: 10.1088/1742-6596/173/1/012006.

[20] D. Akimov et al., COHERENT 2018 at the Spallation Neutron Source, 2018. ArXiv:1803.09183 [Hep-Ex, Physics:Nucl-Ex, Physics:Physics].

[21] B. Dutta, R. Mahapatra, L. E. Strigari, and J. W. Walker, Sensitivity to Z-Prime and Non-Standard Neutrino Interactions from Ultra-Low Threshold Neutrino-Nucleus Coherent Scattering, *Phys. Rev.* D 93, 013015, 2016, doi: 10.1103/PhysRevD.93.013015.

[22] G. Radel and R. Beyer, Neutrino Electron Scattering. [Online]. Available: https://cds.cern.ch/record/248487/files/ppe-93-065.pdf.

[23] D. Geiregat, P. Vilain, and G. Wilquet, Calibration and Performance of the CHARM-II Detector CHARM-II Collaboration, *Nuclear Instruments and Methods in Physics Research* A, 92, 1993, doi: 10.1016/0168-9002(93)91010-K.

[24] Z. Chen, T. Li, and J. Liao, Constraints on General Neutrino Interactions with Exotic Fermion from Neutrino-Electron Scattering Experiments, *J. High Energ. Phys.* 2021, 131, 2021, doi: 10.1007/JHEP05(2021)131.

[25] International Atomic Energy Agency, IAEA Safeguards Glossary 2001 Edition. [Online].
Available: https://www.iaea.org/sites/default/files/iaea_safeguards_glossary.pdf.

[26] C. Stewart, A. Abou-Jaoude, and A. Erickson, Employing Antineutrino Detectors to Safeguard Future Nuclear Reactors from Diversions, *Nat. Commun.* 10, 3527, 2019, doi: 10.1038/s41467-019-11434-z.

[27] Deep Underground Neutrino Experiment. [Online]. Available: https://www.dunescience.org/.

[28] IAEA and Iran: Chronology of Key Events. [Online]. Available: https://www.iaea.org/newscenter/focus/iran/chronology-of-key-events.

[29] IAEA and DPRK: Chronology of Key Events. [Online]. Available: https://www.iaea.org/newscenter/focus/dprk/chronology-of-key-events.

[30] The 1986 Chornobyl Nuclear Power Plant Accident. [Online]. Available: https://www.iaea.org/topics/chornobyl.

[31] Fukushima Daiichi Status Updates. [Online]. Available: https://www.iaea.org/newscenter/focus/fukushima/status-update.

[32] A. Cabrera et al., Neutrino Physics with an Opaque Detector, *Commun. Phys.* 4, 1, 2021, doi: 10.1038/s42005-021-00763-5.

[33] M. Mendoza and J. Daniel, Simulation of the Charge Measurements for the SuperCDMS Soudan Experiment, Thesis, 2020, doi: 10.2172/1605577.

[34] J. C. Zettlemoyer, First Detection of Coherent Elastic Neutrino-Nucleus Scattering on an Argon Target, 2020, doi: 10.5967/3wza-6w73.

[35] P. Vogel, G. K. Schenter, F. M. Mann, and R. E. Schenter, Reactor Antineutrino Spectra and Their Application to Antineutrino-Induced Reactions. II, *Phys. Rev.* C 24, 1543, 1981, doi: 10.1103/PhysRevC.24.1543.

[36] A. C. Hayes and P. Vogel, Reactor Neutrino Spectra, *Annual Review of Nuclear and Particle Science* 66, 219. 2016, doi: 10.1146/annurev-nucl-102115-044826.

[37] T. A. Mueller et al., Improved Predictions of Reactor Antineutrino Spectra, *Phys. Rev.* C 83, 054615, 2011, doi: 10.1103/PhysRevC.83.054615.

[38] P. Huber, On the Determination of Anti-Neutrino Spectra from Nuclear Reactors, *Phys. Rev.* C 84, 024617, 2011, doi: 10.1103/PhysRevC.84.024617.

[39] N. Haag, A. Gütlein et al., Experimental Determination of the Antineutrino Spectrum of the Fission Products of ^{238}U, *Phys. Rev. Lett.* 112, 122501, 2014, doi: 10.1103/PhysRevLett.112.122501.

[40] S. Ishimoto, T. Omori, H. Arima, and K. Ishibashi, Simple Calculation of Reactor Antineutrino Energy Spectrum by the Use of Nuclear Data Libraries, J*ournal of Nuclear Science and Technology* 39, 670, 2002, doi: 10.1080/18811248.2002.9715248.

2. IMPROVEMENTS IN ANTINEUTRINO DETECTOR RESPONSE BY INCLUDING FISSION PRODUCT EXCITED STATES AND CORRECTIONS USING NEW DATA*

2.1. Introduction

The first observation of coherent-elastic-neutrino-nucleus-scattering (CEνNS) in 2017 has offered many possibilities to further nuclear physics frontiers and applications such as alternative nuclear safeguards possibilities using reactor antineutrinos [1] [2]. This is because the intrinsic cross-section of CEνNS is significantly higher than the current state-of-practice inverse beta decay (IBD), which utilizes the reaction as shown below [3]:

$$\bar{\nu}_e + p \rightarrow e^+ + n \qquad (2\text{-}1)$$

where an antineutrino interacts with a proton to produce a positron and a neutron. Since the CEνNS has a higher probability to interact with antineutrinos, intrinsic detection efficiency can be improved and a smaller detector size can be achieved [4].

In a previous study, we demonstrated that a CEνNS based semiconductor detector has greater intrinsic detection efficiency compared to an IBD based detector [4]. However, CEνNS events lead to small energy depositions which are difficult to detect. New technological breakthroughs such as the Z-sensitive Ionization and Phonon (ZIP) detector and the Super Cryogenic Dark Matter Search (SuperCDMS) have enabled detecting these

---

*Reprinted from "Improvements in antineutrino detector response by including fission product isomeric transitions and corrections using new data," by W. E. Ang, S. Lee, and S. Prasad Dec. 2021, *arXiv:2112.12250v1* with minor updates.

signatures [5]. Therefore, we explore the application of CEνNS based semiconductor detectors for a reactor antineutrino measurement, as such a measurement remains to be accomplished [2].

Modeling and understanding a source detector scenario requires accurate knowledge of both the source and the detector. In antineutrino detection, the source term determination is subject to large uncertainties emanating from nuclear data [6]. However, in nonproliferation analysis, a precise reactor antineutrino energy spectrum calculation is highly desirable to obtain an accurate detector response. Thus, it is imperative to understand the sources of uncertainties in the calculation of the antineutrino spectrum using the summation method and the nuclear data libraries. Evaluating these uncertainties is the objective of our study [7].

2.2. Literature review and previous work

2.2.1. Summation method and beta spectrum conversion method

Currently, there are two ways to model the reactor antineutrino spectrum: the "ab-initio" summation method and the beta spectrum conversion method [8]. In the beta spectrum conversion method, an experimentally determined beta spectrum from the reactor core is used to determine the antineutrino spectrum. This is usually done by using the beta spectra that have been measured at the Institut Laue-Langevin (ILL) in Grenoble, France. Since individual β-branches information is not available from the measured integral beta spectrum, Schreckenbach *et al.* developed a conversion method to obtain 30 virtual β branches by dividing the beta spectrum [9]. The β-branches are referred to as beta intensities of excited states as the beta spectrum is continuous, so the Q-values are different for each excited state. An excited state of a nucleus is any energy state higher than its ground state. Then, the antineutrino spectrum is modelled by summing all 30 virtual antineutrino spectra by replacing $E_e = E_0 - E_\nu$, where E_e is total electron energy, E_0 is the endpoint energy, and E_ν is antineutrino energy. The conversion method has been revisited by Mueller *et al.* (2011) [10] and Huber *et al.* (2011) [11] to predict antineutrino spectra for ^{235}U, ^{239}Pu and ^{241}Pu. The beta spectrum of ^{238}U was measured for the first time at Forschungsreaktor München II (FM II) in Garching bei München, Germany in 2013. Haag *et al.* has presented the ^{238}U antineutrino spectrum using conversion method in 2013 [12]. The beta spectrum conversion method is considered a more precise measurement method to calculate the antineutrino spectrum compared to the summation method and will serve as our benchmark [13]. However, the conversion data is only available in the energy range of 2 to 8 MeV [10].

On the other hand, the summation method relies on the information from nuclear data libraries and models the antineutrino spectral from all the contributing fission products. The summation method can be used to calculate the low energy antineutrino spectra, but this method often overestimates the higher part energy of the antineutrino spectrum due to the pandemonium effect [14]. The summation method also suffers from large uncertainties in the cumulative yield, Q values, and beta intensities [13]. Reactor antineutrino spectral prediction using summation method has been performed by Vogel *et al.* (1985) [15] and Hayes. *et al.* (2016) [8]. Vogel *et al.* used the summation method to predict the antineutrino spectrum resulting from both thermal and fast fissions.

2.2.2. TAGS data and pandemonium effect

When a fission product β decays with a large amount of available Q-value, the resulting daughter nuclide can have several different excitation energies, resulting in high energy gamma-rays (or internal conversion electrons) which take away from the kinetic energy of the beta-particle. However, it is well known that measuring high energy gamma-rays is a challenge since not only are these gamma-rays less frequent, but detection efficiency of gamma-rays at higher energies decreases exponentially as a function of energy. Therefore, measurements using high-resolution gamma-ray detectors often over-estimate the contribution of lower energy states and assign them higher beta intensity values, called the pandemonium effect [16]. Figure 2-1 shows the pandemonium effect and how it affects the beta intensity values [17]. The beta intensity is the probability of a β decay to a given excited state with its own unique Q-value.

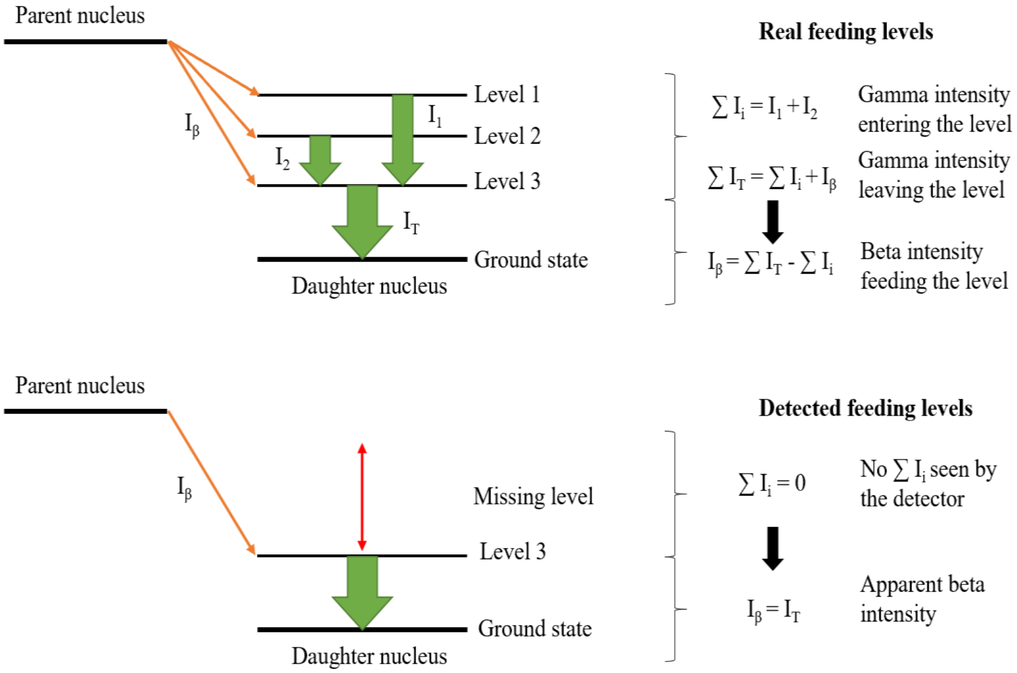

Figure 2-1 An illustration of the apparent pandemonium effect due to the inability to accurately measure gamma-rays and contributions from the higher excited states of a nucleus (adapted from Aguado and Esther, 2012) [17]. This figure incorporates only the gamma emissions from the excited states.

In this paper, we intend to simplify and model the reactor antineutrino spectrum using the summation method with latest nuclear libraries and the fission fragments data that have been measured in recent years using the total absorption gamma spectroscopy (TAGS) technique [18]. TAGS is a technique used to obtain beta intensity info from an isotope, which is free from the pandemonium effect [19]. Without using TAGS, the beta intensities can be determined incorrectly because the detection efficiency of high-purity-germanium (HPGe) detectors begins to decrease beyond 100 keV, which leads to missing information and incorrect calculation on the beta intensities. M. Fallot *et al.* (2017) and M. Estienne *et al.* (2019) have reconstructed the antineutrino spectrum using TAGS data [17] [19]. In this study, we have included the newest TAGS data with additions made after 2019's reactor antineutrino spectra study involving TAGS data [20].

Some of the beta intensity information, especially for those neutron-rich isotopes are not available in nuclear libraries such as ENDF/B-VIII.0 [21]. Thus, we use predicted continuous beta spectra from JENDL-2015 [22] and convert it into antineutrino spectra, which will be discussed in Section 2.3.2. Finally, we demonstrate the impact of including fission fragment transitions and various types of corrections in the summation method to the antineutrino detector response in Section 2.4. We also present pulse height distributions for germanium and silicon detectors in response to the reactor antineutrino spectrum from Texas A&M's 1 MW research reactor.

2.3. Methodology

In our study, we used the summation method to calculate the antineutrino spectra of ^{235}U, ^{238}U, ^{239}Pu and ^{241}Pu from various fissions fragments, using cumulative fission yields data from JEFF-3.3 [23] and decay data (such as Q values and beta intensities) from ENDF/B-VIII.0 [21]. Both fission yields and decay data were extracted and processed using both Python and Matlab programs. One of the challenges of using summation method is to obtain beta intensities of some neutron-rich isotopes because this information is not available in either ENDF/B-VIII.0 or ENSDF [24]. Several methods such as the quasiparticle random phase approximation (QRPA) model and statistical Hauser-Feshbach method [25] have been used to predict the beta intensities and delayed-neutron energy spectra. However, these methods often involve tedious calculations. Thus, for the sake of simplification, our study used continuous beta spectra from JENDL-2015 and converted them into antineutrino spectra. These continuous beta spectra are modeled using the Gross Theory, a theory based on the sum rule of beta strength to calculate beta decay rates and the delayed neutron in the nuclear mass region [26] [27]. Only those fission fragments with cumulative yield more than 10^{-6} [28] were selected in this study as the cumulative yield lower than that will not impact the spectra significantly. The priority order of data selection is used as below:

(i) Decay data from ENDF/B-VIII.0 [21]
(ii) The TAGS decay data sets [29] [30] [31] [32] [33] [34] [35]
(iii) Continuous beta spectra from JENDL-2015 [22]

The data from above are cross-checked with the ENSDF library to ensure the latest data is being used. If latest TAGS data are available, then they will be included in this analysis.

Lastly, one shall not ignore the contribution of the ^{238}U breeding event as it also produces antineutrino during the neutron capture reaction. The ^{238}U will first capture one neutron to produce ^{239}U. Next, ^{239}U will be beta decaying into ^{239}Np and lastly to ^{239}Pu with another beta decay reaction [36]. The contribution of ^{238}U neutron capture to detector response and pulse height distribution will also be included in our study.

2.3.1. Antineutrino spectrum calculation and corrections

An antineutrino spectrum of the fissionable isotopes (^{235}U, ^{238}U, ^{239}Pu and ^{241}Pu) is the sum of all fission fragments that undergo β- decay with all their, i-th branches [15] [8]:

$$\frac{dN}{dE_v} = \sum_n Y_n(Z, A, t) \sum_i b_{n,i}(E_0^i) P_v(E_v, E_0^i, Z) \qquad (2\text{-}2)$$

The beta intensities, $b_{n,i}$ are normalized to unity ($\sum_i b_{n,i} = 1$, unless the fission fragments have additional decay modes) and P_v is the normalized antineutrino spectrum with endpoint energy, E_0^i. The $Y_n(Z, A, t)$ is number of β decays of fission fragment Z and A at time t. After a reactor burns for sufficient time, Y_n is approximately cumulative yield and independent of t. In this study, the fission fragments with cumulative yields greater than 10^{-6} were used in this study [28]. The antineutrino emission spectrum for a fission product can be written as [8]:

$$P_v\left(E_v, E_0^i, Z\right) = k p_e (E_0 - E_e)^2 F(Z, E_e) C(Z, E_e)[1 + \delta(Z, A, E_e)] \qquad (\text{2-3})$$

In our calculation, k is the normalization constant, p_e is electron momentum, $F(Z, E_v)$ is the Fermi function, Z is the atomic number, E_v is the initial antineutrino energy incident on the detector, E_e is the total electron energy, $m_0$is electron rest mass and $C(Z, E_e)$ is shape factor. For allowed decay, $C(Z, E_e)$ is equal to 1. The notation E_0 here is the endpoint energy and approximately equal to $Q + m_0 c^2$, where Q is reaction Q-value. The function $\delta(Z, A, E_e)$ expresses the corrections that should be considered to the shape of the spectrum including finite size correction, radiative correction, and weak magnetism correction, which have been discussed in Huber *et al.* (2011) and Hayes *et al.* (2016) papers [8] [11]. To obtain antineutrino spectrum, Eq. 2-3 is required to substitute with $E_v = E_0 - E_e$.

The Fermi function, $F(Z, E_v)$ here is used to account for the Coulomb field on the shape of the beta spectrum. The Fermi Function is given by [8]:

$$F(Z, E_e) = 4(2 p_e R)^{-2(1-\gamma)} \left| \frac{\Gamma(\gamma + iy)}{\Gamma(2\gamma + 1)} \right|^2 e^{\pi y} \qquad (\text{2-4})$$

where:

$\gamma = \sqrt{1-(\alpha Z)^2}$ and $y = \propto ZE_e/p_e$. The R is the nucleus radius and is given as $R = 1.2A^{1/3} fm,$ α is the fine structure constant (~1/137), Z is the nuclear charge of daughter nucleus. The notation i is an imaginary number and Γ is the gamma function.

The finite size correction, δ_{FS}, is used to correct for the electric charge spatial distribution and hypercharge distribution (from the point-charge treatment) of the nucleus [11]. The equation of a finite size correction is given by [37]:

$$\delta_{FS} = -\frac{8}{5}\frac{Z\alpha RE_e}{\hbar c}\left(1+\frac{9}{28}\frac{m_e^2 c^4}{E_e^2}\right) \tag{2-5}$$

Where $\hbar$ is reduced Plank's Constant, m_e the mass of electron, and c is the speed of light. Next, an approximation for weak magnetism correction is used in this study and defined as [8]:

$$\delta_{WM} = 0.5\%\, E_e\, MeV^{-1} \tag{2-6}$$

The weak magnetism correction is used to account the effect of the interaction of the outgoing electron with magnetic moment [8] [11]. Lastly, the radiative correction is used to account for the effect that arise from the interaction of the photon field and the electron-positron field [38]. The radiative correction can be defined as [8]:

$$\delta_{QED} = \frac{\alpha}{2\pi} h\left(\hat{E}, E_0\right) \tag{2-7}$$

The function $h\left(\hat{E}, E_0\right)$ has been computed by Sirlin (2011) is written as [39]:

$$\begin{aligned} h\left(\hat{E}, E_0\right) = 3\ln\left(\frac{m_p}{m_e}\right) + \frac{23}{4} - \frac{8}{\hat{\beta}} Li_2\left(\frac{2\hat{\beta}}{1+\hat{\beta}}\right) \\ + 8\left(\frac{tanh^{-1}\hat{\beta}}{\hat{\beta}} - 1\right) ln\left(\frac{2\hat{E}\hat{\beta}}{m}\right) \\ + 4\frac{tanh^{-1}\hat{\beta}}{\hat{\beta}}\left[\frac{7+3\hat{\beta}^2}{8} - 2tanh^{-1}\hat{\beta}\right] \end{aligned} \quad (2\text{-}8)$$

where $\hat{E} = E_0 - E_v$, $\hat{p} = \left(\hat{E}^2 - m_e^2\right)^{1/2}$, and $\hat{\beta} = \hat{p}/\hat{E}$. The function $L_2(x)$ is the dilogarithm and defined as $L_2(x) = -\int_o^x (\frac{dt}{t}) \ln(1-t)$. Huber *et al.* has done a detail analysis on finite size, radiative and weak magnetism correction with the antineutrino spectra using conversion method [11].

2.3.2. Conversion of continuous beta spectrum to antineutrino spectrum

For simplification, an empirical method is used to obtain antineutrino spectrum from continuous beta spectrum (JENDL-2015) by using equation below [12]:

$$N_v(E) = N_\beta(E - 511\ keV - 50\ keV) \cdot k(E) \quad (2\text{-}9)$$

The antineutrino spectra can be corrected by shifting the beta spectrum with the rest mass of the electron, and 50 keV to account the Coulomb attraction of nucleus and electron. The correction function $k(E)$ here is expected to be close to unity and in the order of 5% [12].

2.3.3. CEνNS Cross-Section Calculation

The differentiate equation of CEνNS cross-section over the recoil energy is defined as [35]:

$$\frac{d\sigma(E_v)}{dT_R(E_v)} = \frac{G_F^2 M}{2\pi}[(q_v + q_A)^2 + (q_v - q_A)^2\left(1 - \frac{T_R}{E_v}\right)^2 - (q_v^2 - q_A^2)\frac{MT_R}{E_v^2}] \qquad (\text{2-10})$$

The Eq. 2-10 is integrated into Eq. 2-11 to obtain the CEνNS cross-section as a function of the incident antineutrino energy. The integrated CEνNS is shown as below:

$$\sigma(E_v) = \int_{T_R min}^{T_R max} A_1 T_R + A_2 T_R - \frac{A_2 T_R^2}{E_v} + \frac{A_2 T_R^3}{3{E_v}^2} - \frac{A_3 M T_R^2}{2{E_v}^2} \qquad (\text{2-11})$$

where G_F denotes the Fermi constant, M is the mass of targeted nucleus, q_v and q_A are vector and axial charges respectively, T_R is recoil energy and E_v is incident neutrino energy. The maximum recoil energy can be calculated by [36]:

$$T_R^{Max} = \frac{2E_v^2}{M + 2E_v} \qquad (\text{2-12})$$

A_1, A_2 and A_3 here are constants where:

$$A_1 = \frac{G_F^2 M}{2\pi}(q_v + q_A)^2 \qquad (\text{2-13})$$

$$A_2 = \frac{G_F^2 M}{2\pi}(q_v - q_A)^2 \qquad (\text{2-14})$$

$$A_3 = \frac{G_F^2 M}{2\pi}(q_v^2 - q_A^2) \qquad (\text{2-15})$$

The vector charges, q_v is defined as:

$$q_v = g_v^p Z + g_v^n N \tag{2-16}$$

where g_v^p and g_v^n are vector proton and neutron weak neutral current couplings respectively where $g_v^p = 0.0298$ and $g_v^n = -0.5117$ [40]. The axial term q_A, is usually smaller by a factor 1/N^2 and it is 0 for the spin zero nuclei [41] [42] [43]. Thus, the axial term is neglected in our calculation [2]. The weights and abundances of Ge and Si are obtained from the Nuclear Data Center, Japan Atomic Energy Agency to assist the CEνNS cross-section calculation and tabulated into the table below [44].

Table 2-1 Natural Germanium and natural Silicon with its isotopes and abundance.

Ge nuclides	Weight (amu)	Abundance (%)	Si nuclides	Weight (amu)	Abundance (%)
^{70}Ge	69.92	20.57	^{28}Si	27.98	92.223
^{72}Ge	71.92	27.45	^{29}Si	28.98	4.685
^{73}Ge	72.92	7.75	^{30}Si	29.97	3.092
^{74}Ge	73.92	36.50			
^{76}Ge	75.92	7.73			

2.3.4. Detector response calculation

We defined the detector response reaction rates in terms of incident antineutrino energy as:

$$R(E_v) = N\sigma(E_v)\phi(E_v) \tag{2-17}$$

where N is the number of nuclides, σ is the CEνNS cross-section and ϕ is the antineutrino flux. In our study, we also calculate the minimum antineutrino energy required to trigger a 20 eV nuclear recoil for both natural Ge and natural Si, which defined as [36]:

$$E_{min} = \frac{T_R + \sqrt{2MT_R + T_R^2}}{2} \tag{2-18}$$

2.3.5. Pulse height distribution calculation

Once we obtained the detector response rate from above section, we can use this information to calculate the distribution of the recoil energies deposited in the detector for a given incident antineutrino energy. The calculation of pulse height distribution as a function of recoiled nucleus' energies uses Eq. 2-19 which provides the probability, $P(E_v \rightarrow T_R)$, that given an incident antineutrino with energy, E_v, undergoes a CEνNS interaction, the nucleus will recoil with energy T_R. We define the distribution of recoiled energies for a given incident antineutrino energy as below:

$$P(E_v \rightarrow T_R) = \frac{d\sigma(E_v, T_R)}{dT_R} / \sigma(E_v) \tag{2-19}$$

Then, we can define pulse height distribution, C as a function of T_R:

$$C(T_R) = \int_{E_v} N\sigma(E_v)\phi(E_v)P(E_v \rightarrow T_R)dE_v \tag{2-20}$$

We assume a 100 kg of natural Ge and natural Si detectors with 20 eV nuclear recoil thresholds are placed 10 m away from the 1 MW TRIGA rector core at Nuclear Science Center, Texas A&M University. Fission parameters and assumptions used to calculate detector response and pulse height distribution are shown in Table 2-2 [36]:

Table 2-2 Parameters and assumptions used for detector response and pulse height distribution calculation.

Parameters		Values
Fission rate		3.1×10^{16} s^{-1}
Antineutrino production rate		1.8×10^{17} s^{-1}
Fission Fraction	^{235}U	0.967
	^{238}U	0.013
	^{239}Pu	0.02
	^{241}Pu	0.001
	^{238}U to ^{239}Pu	0.16

2.4. Result and discussion

A total of 535 fission fragments from ^{235}U, 575 fission fragments from ^{238}U, 558 fission fragments from ^{239}Pu and 595 fission fragments from ^{241}Pu are selected in our analysis. Many of these fission fragments are common to all four fissionable isotopes. Table 2-3 shows the number of fission fragments obtained from ENDF/B-VIII.0 and JENDL-2015. A total of 210 isotopes are missing beta intensities in ENDF/B-VIII.0; for these isotopes their continuous beta spectra in Eq. 2-9 using data from JENDL-2015 will be used, as presented in Appendix B.

Table 2-3 The number of fission fragments data obtained from ENDF/B-VIII.0 library and JEDNL-2015 library.

Fissionable Isotopes	ENDF/B-VIII.0	JENDL-2015
^{235}U	393	142
^{238}U	385	190
^{239}Pu	421	137
^{241}Pu	411	184

In this study, we present four type of corrections to demonstrate the impact of the corrections to the antineutrino spectrum. We will first model the spectrum without considering any excited states; then we apply the corrections one at a time as shown below:

(a) Including of excited states using the data variable in ENDF/B-VIII.0;

(b) Improving of excited states using TAGS data from published literature;

(c) Including of missing excited states correction with continuous beta spectrum as in Eq. 2-9 (Gross Theory); and

(d) Correcting for the nucleus' finite size, radiative and weak magnetism

2.4.1. Including excited states

Once a fission product is formed, it may not be formed directly in its ground state. The newly formed nucleus usually stays at a different excited state and de-excites by emitting gamma rays. Thus, it is important to include all transitions (β branches) with their beta intensities when computing the antineutrino spectrum. Figure 2-2 shows the comparison between the antineutrino spectra without considering the transitions (ground state beta intensity = 1) and the spectra including all transitions that are available in the ENDF/B-VIII.0 data library, for ^{235}U, ^{238}U, ^{239}Pu, and ^{241}Pu.

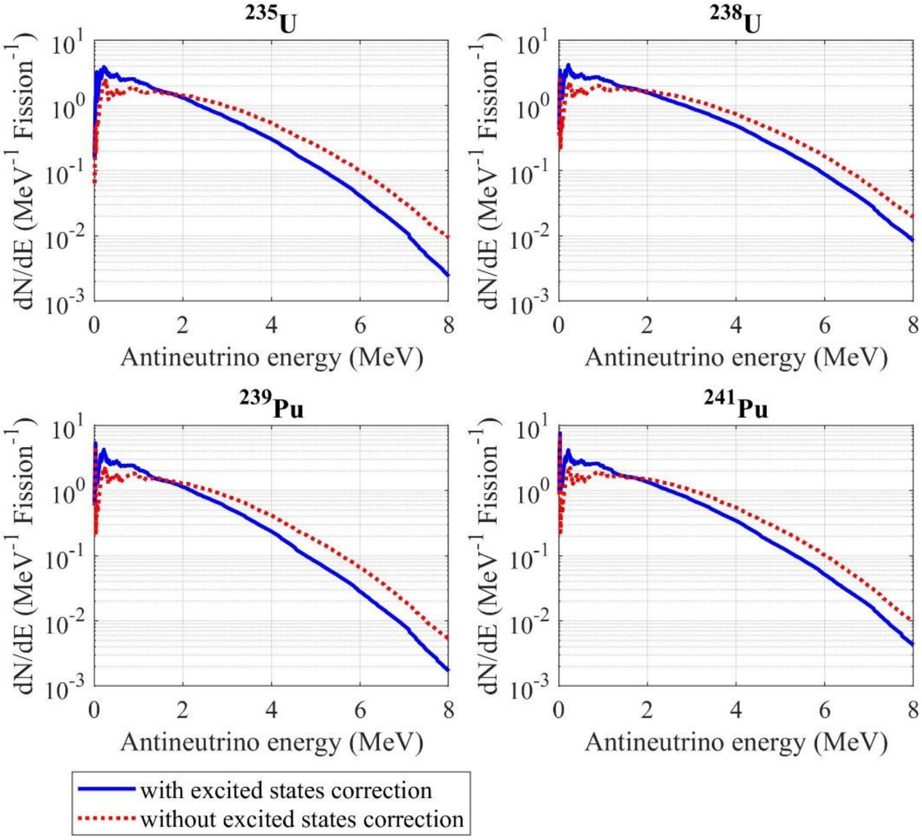

Figure 2-2 A comparison between the spectra without excited states correction and the spectra with all excited states available in the ENDF/B-VIII.0 data library included, for major fissionable isotopes.

The inclusion of excited states shifts the spectra to lower energies in Fig. 2-2, as expected, since the excess energy of excited states is being rightly discounted. The antineutrino spectra after the excited state corrections have noticeable deviations where the corrected spectra are shifted to lower energies compared to the spectra without the transition corrections in the range 2 to 8 MeV. For ^{235}U, the discrepancy can be up to a 75.38% deficit at 8 MeV. This deficit at higher energies in the corrected spectra can also found in ^{238}U, ^{239}Pu and ^{241}Pu, where the differences are 57.36%, 67.95% and 56.23%, respectively. On the other hand, the spectra without transition corrections tend to underestimate the low energy range (0 - 2 MeV). In the range of 0.5 MeV – 2 MeV, the spectra for all four fissionable isotopes are enhanced 29% to 37% on average. In the range of 2 MeV – 8 MeV, the spectra for ^{235}U, ^{238}U, ^{239}Pu, and ^{241}Pu shifted to lower energies with an average of 49.35%, 39.09%, 47.94% and 41.07%, respectively. Thus, inclusion of excited states shows a significant impact and corrections to the shape of spectra.

2.4.2. Consideration of TAGS data set

In our study, we have identified TAGS data sets based on availability found in published literature and included them in our calculations. We included TAGS data sets from Greenwood *et al.* from 1997 to the most recent TAGS data sets by J. Gombas *et al.* (2021) to obtain the antineutrino spectra. This section is intended to demonstrate the improvement before and after including the TAGS data, once the excited states have been included.

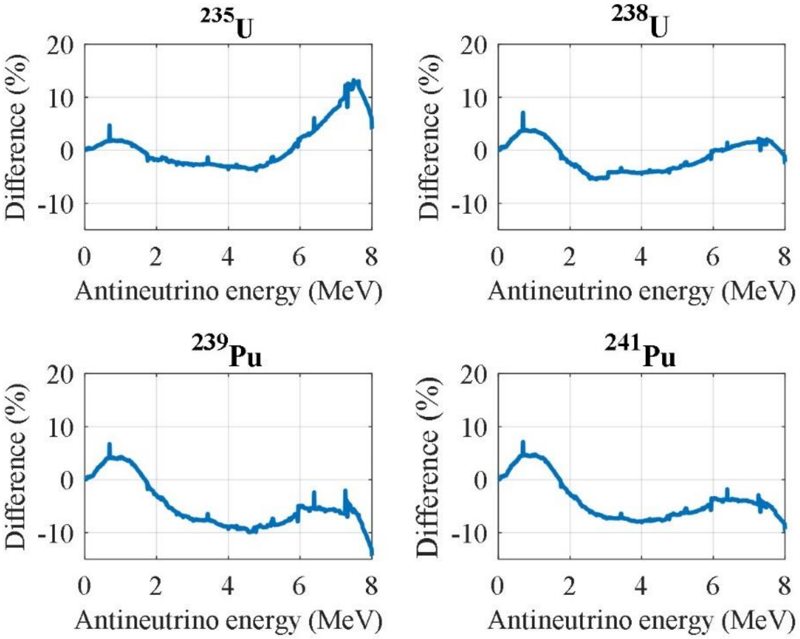

Figure 2-3 Percent differences observed in the antineutrino spectra as a function of antineutrino energy, for all four fissionable isotopes, after including the TAGS data set.

Fig. 2-3 shows the spectra before and after correcting for the pandemonium effect with the TAGS data sets from the Appendix A obtained from the literature review. Overall, there is a noticeable enhancement of the antineutrino spectrum in the energy range of 0 to 2 MeV. For ^{241}Pu, the deviation is the highest among all four fissionable isotopes, where the discrepancy is 7.13% in the energy range 0 to 2 MeV whereas, the other spectra increased to 4.71% for ^{235}U, 7.09% for ^{238}U and 6.72% for ^{239}Pu. In the range 2 to 6 MeV, the spectra for all four fissionable isotopes decreased by less than 10%. In the range 6 to 8 MeV, the corrected spectra increased for ^{235}U and ^{238}U such that the largest difference observed are 13.25% and 2.20%, respectively. The corrected ^{239}Pu and ^{241}Pu spectra are decreased in the range of 6 to 8 MeV, where the highest differences are 14.37% and 9.54%, respectively. One of the major contributors of this discrepancy is ^{92}Rb as the difference of their ground state beta intensity between ENDF/B-VIII.0 and TAGS data is 71.57%. Table 2-4 shows the different ground-state-Q values quoted in ENDF/B-VIII.0 and TAGS.

Table 2-4 The difference in beta intensity values between ENDF/B-VIII.0 and TAGS.

Nuclide	Q value (MeV)	Ground state beta intensity (%) – ENDF/B-VIII.0	Ground state beta intensity (%) - TAGS
^{92}Rb	8.095	51 ± 18	87.5 ± 2.5
^{142}CS	7.308	43 ± 3	$46.4^{+2.7}_{-3.0}$
^{100}Nb	6.396	50 ± 7	$46.0^{+8.0}_{-15.0}$

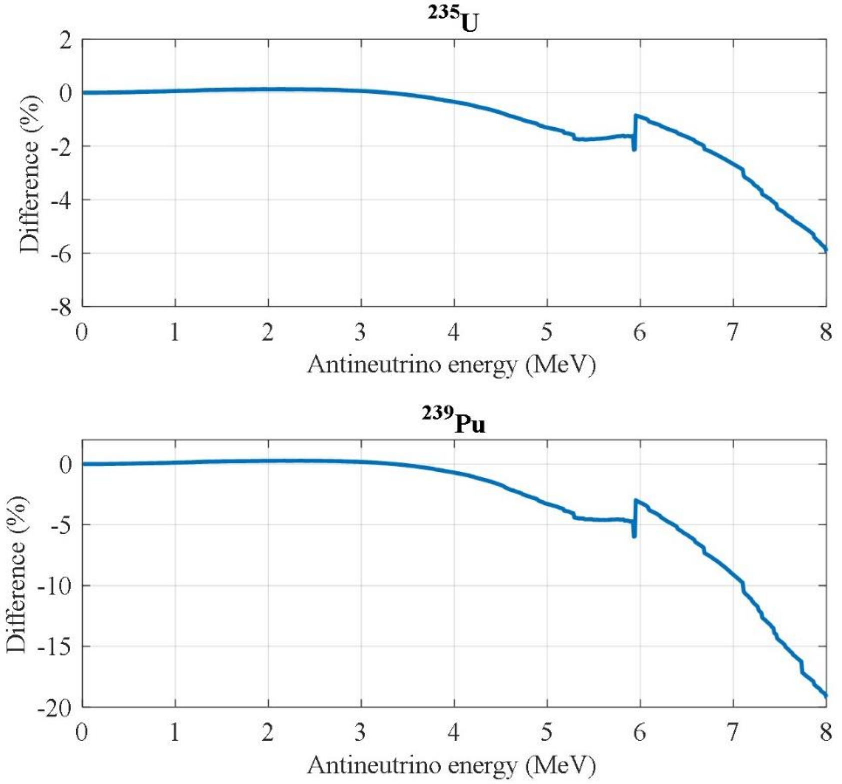

Figure 2-4 A comparison between the antineutrino spectra with the most recent TAGS data set by J. Gombas *et al.* (2021).

The spectra with the 2021 TAGS data sets have significant impact on energy in the range 6 – 8 MeV. For ^{235}U and ^{239}Pu, the average difference with and without the 2021

TAGS data sets in the range 6 – 8 MeV is 3% and 10%, respectively. The highest discrepancies can be observed at 8 MeV for both ^{235}U and ^{239}Pu, with 5.95% and 19.22% deviation, as shown in Fig. 2-4. The reason for these high discrepancies at high energies is due to the missing excited states information of ^{103}Nb and ^{104m}Nb in ENDF/B-VIII.0 nuclear library.

2.4.3. Missing excited states data correction

Some beta intensities and excited states are not available in ENDF/B-VIII.0, especially for neutron-rich isotopes. Thus, we have used the predicted beta continuous spectrum in Eq. 2-9 from JENDL-2015 and integrated them into our study. Figure 2-5 below shows the difference of the spectra using data from JENDL-2015 and the spectra without using the continuous spectrum (assuming the beta intensity to the ground state is 100%).

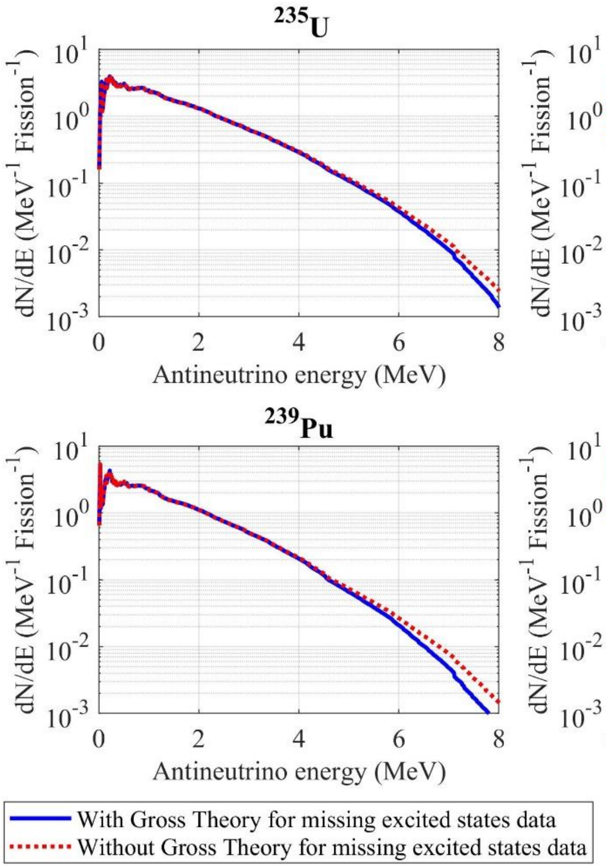

Figure 2-5 A comparison of the antineutrino energy spectra with the neutron-rich fission products correction, and the spectra without the correction. The corrected antineutrino spectra reduce the counts at higher energies.

For ^{235}U, the spectrum without neutron-rich fission products (FPs) correction is reduced by an average of 4.43% in the range of 3 MeV to 6 MeV. This discrepancy gets larger from 6 MeV to 8 MeV, where the spectrum without the correction is reduced by 11.56% to 43.56% after considering the continuous spectrum from JENDL-2015. The ^{238}U spectrum without the correction is also reduced by an average of 11.69% from 3 MeV to 6 MeV. The discrepancy is even higher where the spectrum before the correction is reduced by 27.78% to 61.74% within 6 – 8 MeV. The uncorrected ^{239}Pu and ^{241}Pu spectra are decreased by 7.57% and 13.6% respectively, after the missing excited states data correction for neutron rich isotopes in the range of 3 MeV to 6 MeV. However, between 6 and 8 MeV, the discrepancy of the corrected and uncorrected ^{241}Pu is the highest among all four fissionable isotopes, where the uncorrected spectrum is reduced by 34.76% to 69.46%

2.4.4. Finite size, radiative and weak magnetism corrections

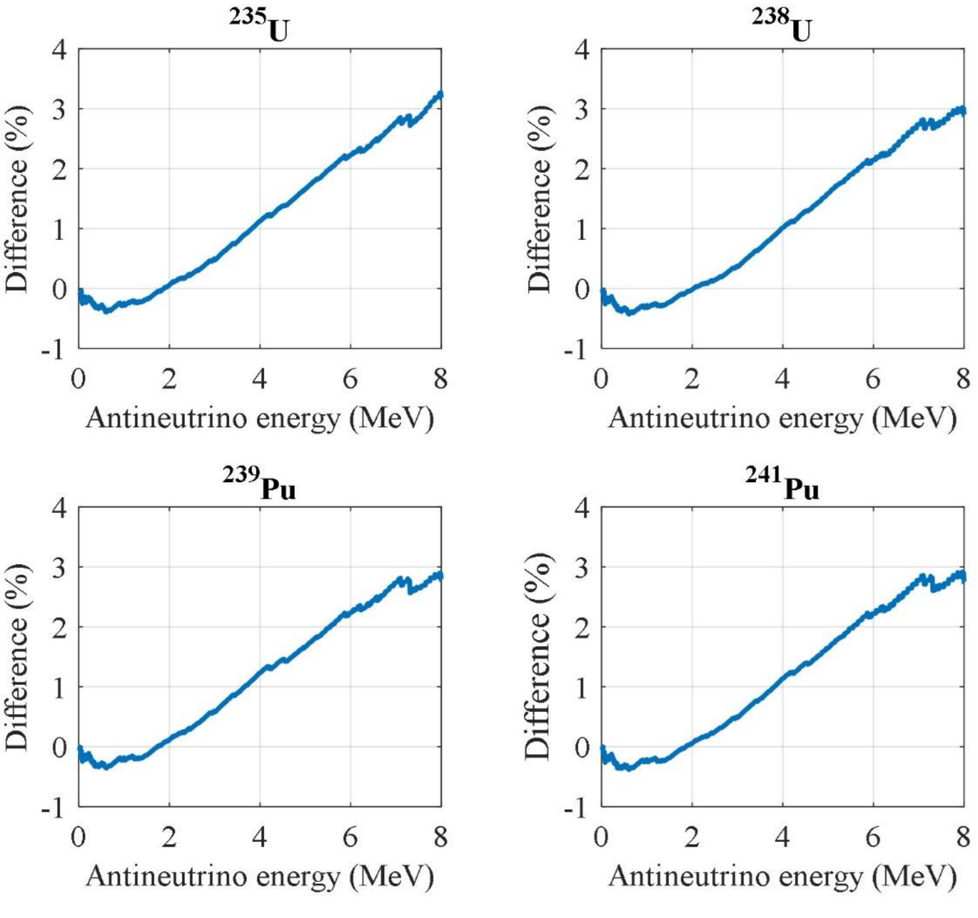

Figure 2-6 Percent difference of the corrected antineutrino spectra as a function of the antineutrino energy. Corrections were made for finite size, weak magnetism and radiative corrections. The corrected spectrum sees an increase in counts towards higher energies.

Next, we applied finite size, radiative and weak magnetism corrections on the result from section 2.3.1 given by Eq. 2-5 – 2-8. The differences of the spectrum with and without finite size, weak magnetism and radiative are shown in Fig. 2-6. In the energy range of 0 to 2 MeV, the differences between corrected and uncorrected spectrum for all four fissionable isotopes are no more than 0.43% smaller. From 2 MeV, the difference between corrected and uncorrected spectrum for all four fissionable isotopes start to increase gradually to less than 3.27% at 8 MeV. In Fig. 2-6, we find that the finite size, weak magnetism and radiative corrections have greater impact on the spectrum in the high energy range. The finite size correction is the main contributor where 2.04% to 2.20% average enhancement can be observed from all four fissionable isotopes from 2 – 8 MeV. In the energy range 0 – 2 MeV, only 0.22% and 0.31% average deficit are observed with finite size correction. For weak magnetism correction, 0.61% to 0.71% average deficit deviations are found after the correction for all four fissionable isotopes at 2 – 8 MeV. On the other hand, 0.06% to 0.08% enhancement are observed in the energy range 0 to 2 MeV. Lastly, radiative correction contributes about 0.20% to 0.24% increment from 2 – 8 MeV for ^{235}U, ^{238}U, ^{239}Pu and ^{241}Pu. However, from 0 to 2 MeV, there are 0.02% to 0.03% average deficit with radiative correction.

2.4.5. Comparison corrected spectrum with previous work

To establish the validity of our method, we compared our modeled spectra with previous works from Hayes *et al.* (summation method) and Huber *et al.* (conversion method) in this section. It is worth mentioning, that Ishimoto *et al.* (2002) developed an estimation method without including all transitions from the fission fragments [45]. By introducing a correction factor, $F_a(E_v) = C(1 - \frac{E_v}{Q})^n$ into Eq. 2-3 which alters the spectrum such that it matches with the others experimental spectra. The notation C is the normalization factor and n is an adjustable parameter. Our previous preliminary study was performed using this method to model the antineutrino spectra, and the results can be found from the reference [4]. We also present our result using Ishimoto's method here for comparison purposes.

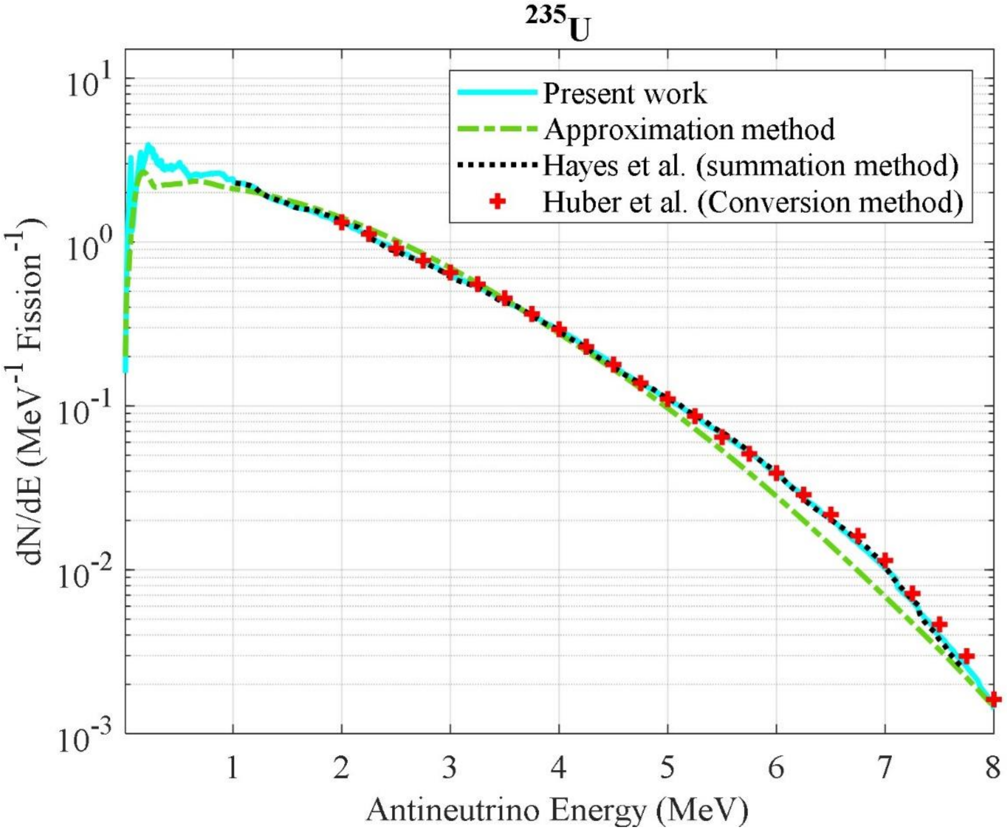

Figure 2-7 The ^{235}U spectra from this study (summation and approximation method), Hayes *et al.* (summation method) and Huber *et al.* (conversion method).

Fig. 2-7 shows the comparison of calculated ^{235}U antineutrino spectrum with Huber *et al.* (2011) [11] and Hayes *et al.* (2016) spectrum, which used the conversion and summation method, respectively [11] [8]. Our calculated ^{235}U antineutrino spectrum agrees with Huber *et al.* spectrum with an average 2.07% discrepancy in the range of 2 – 6 MeV. The discrepancy is higher between 6 and 8 MeV, where 3 to 18% deviation is observed. Our calculated spectrum has lower discrepancies when compared to spectra by Hayes *et al.*, where an average of 1.28% is calculated in the energy range 1 – 7.5 MeV. The ^{235}U spectrum using the Ishimoto's approximation method underestimates the spectrum at the energy range lower than 1.5 MeV with an average of 16.78% difference compared to the present work. The approximated ^{235}U spectrum has better agreement with our ^{235}U spectrum using summation method in the range of 4 and 5 MeV with an average of 7% difference. The deviation of the approximation methods becomes greater in the range 5 - 8 MeV where 11% to 33% is observed.

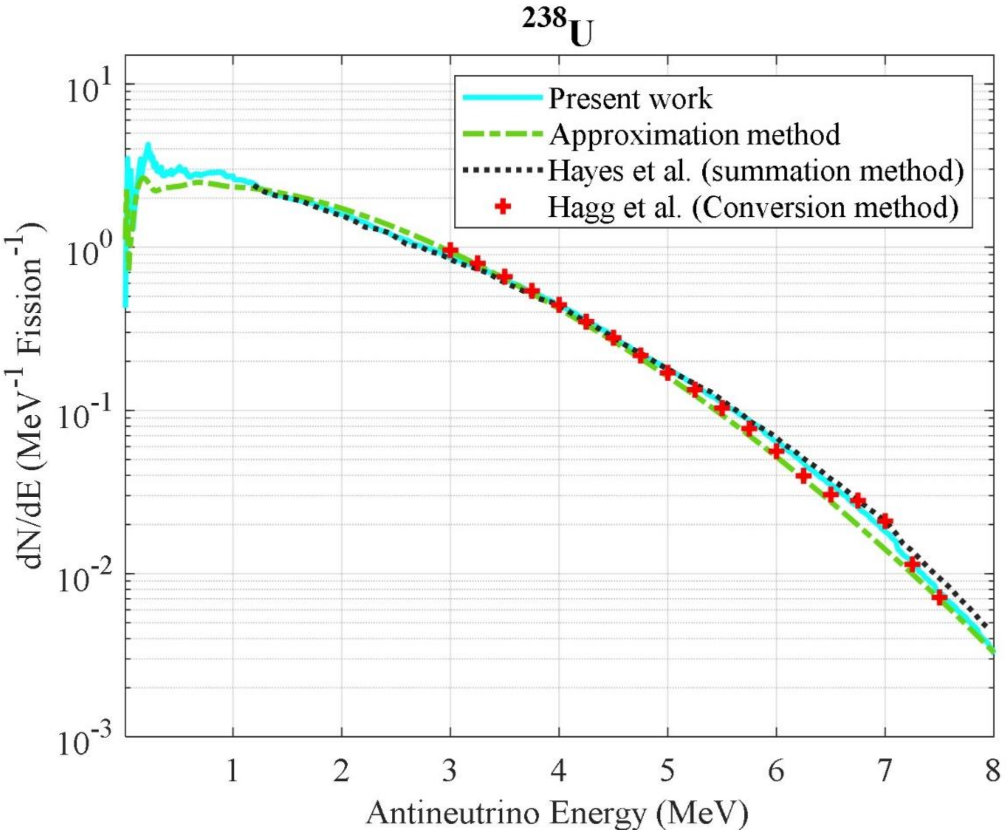

Figure 2-8 The ^{238}U spectra from this study (summation and approximation method), Hayes *et al.* (summation method) and Haag *et al.* (conversion method).

Overall, the corrected ^{238}U spectrum has lower discrepancies when compared to Hayes *et al.* (2016) conversion result than Haag *et al.* (2013) spectrum [12]. From 1 to 6 MeV, the discrepancy with Hayes *et al.* spectrum is no more than 3.6%. However, from 6 MeV to 8 MeV, the deviation gradually increases from 6% to 30%. On the other hand, our calculated results have larger deviations from Haag *et al.* (2013) results from 3 to 7 MeV where there is an average of 7.51% difference. Beyond 7 MeV, our results have better agreement with Hagg *et al.* results with no more than 7% difference. Overall, the ^{238}U spectrum using Ishimoto's method underestimates the spectrum by an average of 16.34%

difference at low energies (< 1.5 MeV). The difference is greater from 5 MeV to 8 MeV where 10% to 24% deviation is observed.

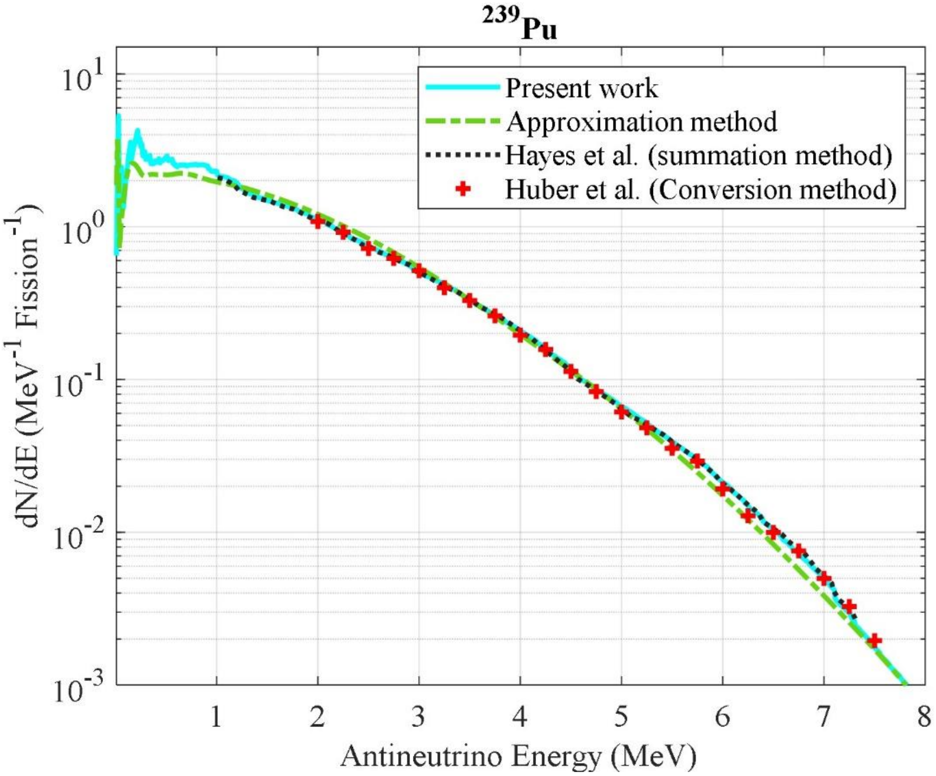

Figure 2-9 The ^{239}Pu spectra from this study (summation and approximation method), Hayes *et al.* (summation method) and Huber *et al.* (conversion method).

From 2 – 8 MeV, the spectrum by Huber *et al.* spectrum has an average deviation of 5.96% with our calculated ^{239}Pu results, where the highest deviation is at 7.75 MeV with 25.81% difference. Hayes *et al.* spectrum has an average difference of 2.17% from our results in the range 1 MeV – 7.25 MeV. The decrepanies between our results and Hayes *et al.* are no more than 3.4% from 1.25 MeV to 6.5 MeV. For ^{239}Pu spectrum using the Ishimoto's approximation method, the spectrum is underestimated with an average of 21.22% compared to our spectrum using summation method. In the energy range 4 to 8

MeV, the approximated spectrum is underestimated with the highest deviation of 22% difference at 7 MeV.

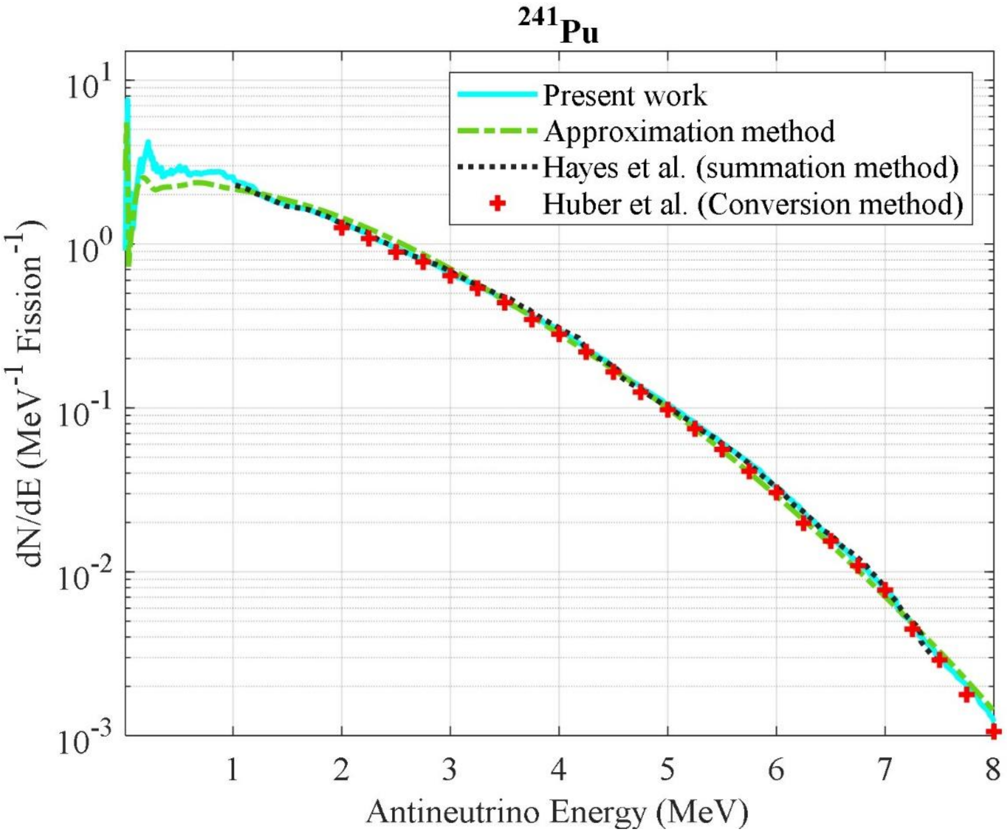

Figure 2-10 The ^{241}Pu spectra from this study (summation and approximation method), Hayes *et al.* (summation method) and Huber *et al.* (conversion method).

Our calculated ^{241}Pu spectrum has larger discrepancies with Huber *et al.* result than with Hayes *et al.* spectrum. Overall, the calculated spectrum has an average discrepancy of 6.61% with Huber *et al.* spectrum from 2 – 8 MeV, where the highest difference is observed at 6.25 MeV with a 14.88% deviation. For Hayes *et al.*, our results agreed with no more than 3.5% difference, except at 1 MeV with 6.59% and 7.5 MeV with 14.24%. Overall, the average discrepancy between our corrected spectrum and Hayes *et al.* spectrum is about 2.01%. The result of the spectrum using the Ishimoto approximation method is underestimated at low energy range less than 1 MeV with an average of 20.84% deviation.

2.4.6. Detector response and pulse shape distribution

In this section, we would like to demonstrate the impact of various corrections to the detector response. We also present pulse shape distribution with our corrected spectra using the results from the detector response.

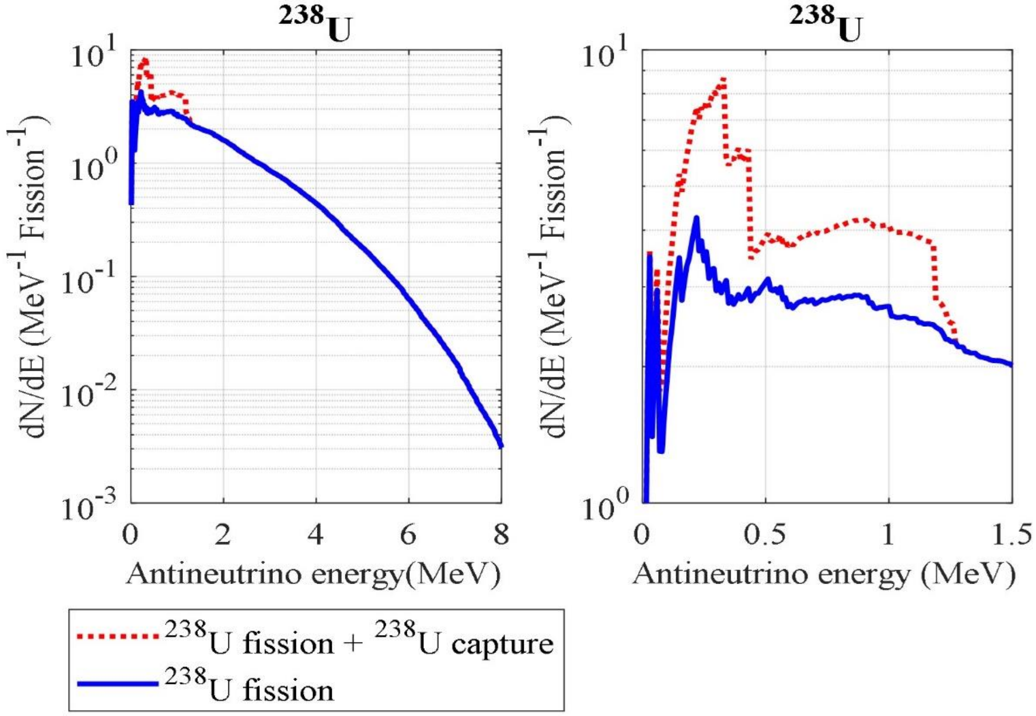

Figure 2-11 The antineutrino spectrum from ^{238}U fission event and the ^{238}U capture event. The breeding information due to capture lies below the 1.3 MeV.

The contribution ^{238}U capture event to antineutrino production should be taken into consideration when calculating the detector response with CEνNS because it has the potential to measure these energies. In 1 MW TRIGA reactor, the capture event of ^{238}U contributes about 0.16 of fission fraction. In a typical power reactor, the fraction of ^{238}U capture events is even higher with 0.6 [35]. Figure 2-11 shows the antineutrino spectrum of ^{238}U with and without neutron capture events. A ^{238}U neutron capture event will produce two antineutrinos from two beta decay of ^{239}U with an average energy of 0.54 MeV, each. Table 2-5 shows the average number of antineutrino emitted and its average energies from our corrected spectra.

Table 2-5 The average number of antineutrino emission ($\boldsymbol{N_\nu}$) and its average energies ($\boldsymbol{E_\nu}$) for ^{235}U, ^{238}U, ^{239}Pu and ^{241}Pu.

Fissionable Isotopes	E_ν (MeV)	N_ν (per fission)
^{235}U	1.49	6.08
^{238}U	1.65	7.17
^{239}Pu	1.36	5.51
^{241}Pu	1.48	6.26
^{238}U to ^{239}Pu	0.54	2.00

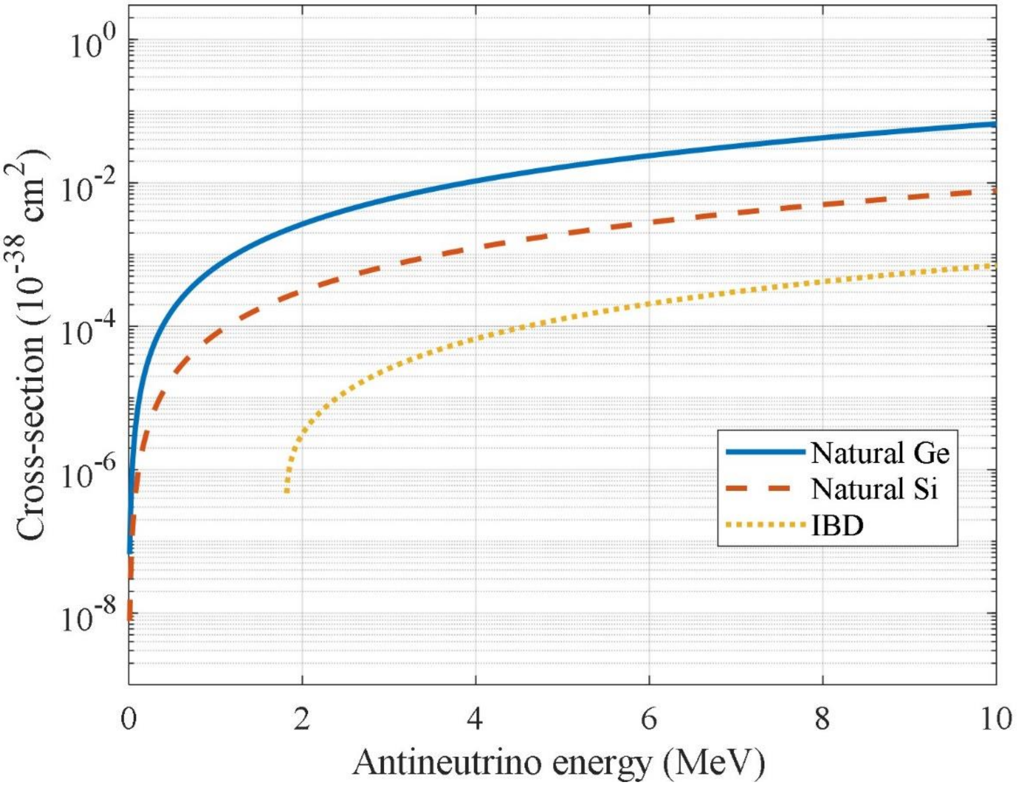

Figure 2-12 CEνNS cross-section as a function energy for natural Ge, natural Si, and IBD.

Fig. 2-12 shows the CEνNS cross-section of natural Ge and natural Si as a function of incident antineutrino energy, calculated using Eq. 2-11. For comparison purposes, the IBD cross-section is also included in Fig. 2-10. There is no energy intrinsic threshold of CEνNS cross-section for natural Ge and natural Si, its threshold is determined by the sensor. In contrast, the IBD cross-section has an intrinsic threshold of 1.806 MeV to initiate the reaction. Overall, the flux weighted average CEνNS cross-sections for natural Ge and natural Si are 4.35×10^{-40} cm^2 and 5.09×10^{-41} cm^2, respectively. The IBD flux weighted average cross-section is 4.56×10^{-42} cm^2. In our study, we assume that the detectors are placed 10 m away from the outer core of the 1 MW(th) TRIGA reactor and the detectors weight 100 kg. Additionally, the CEνNS detectors have a detection threshold of 20 eV nuclear recoil. This corresponds to 0.82 MeV incident antineutrino energy in natural Ge and 0.51 MeV incident antineutrino energy in natural Si. The table below shows comparison between the difference before and after the various corrections:

Table 2-6 The detector response of natural Ge and natural Si detectors in events/day with various type of corrections implemented sequentially, one after another.

Types of correction	Detector response (Events/day)	
	Natural Ge	Natural Si
Case 1 a) ENDF/VIII.0 data - No transition is considered	36.62	12.24
Case 2 a) Excited states - ENDF/VIII.0 excited states	21.58	7.50
Case 3 a) Excited states - ENDF/VIII.0 excited states - TAGS corrected excited states	21.19	7.37
Case 4 a) Excited states - ENDF/VIII.0 excited states - TAGS corrected excited states - Gross Theory for missing excited states data	20.38	7.13
Case 5 a) Excited states - ENDF/VIII.0 excited states - TAGS corrected excited states - Gross Theory for missing excited states data b) Finite size, radiative and weak magnetism correction	20.57	7.18

Types of correction	Detector response (Events/day)	
	Natural Ge	Natural Si
<u>Case 6</u> a) ENDF/VIII.0 data - No transition is considered - Ishimoto’s approximation method	20.39	7.15

Natural Ge and natural Si detectors response rate after all corrections (including ^{238}U neutron captures) are 20.38 events/day and 7.13 events/day. The biggest impact on the detector responses is due to the inclusion of the excited states from ENDF/B-VIII.0. The difference in the detector response with and without excited states consideration in both natural Ge and natural Si is about 38 to 41%. The finite size, radiative, weak magnetism corrections are the least contributors, where only a 0.7 to 0.9% difference is observed in the detector response when accounting for these factors. Next, our results show that taking TAGS data set into consideration contribute a 1.7 to 1.8% deviation in the detector response. Additionally, the detector response for natural Ge and natural Si without J. Gombas *et al.* TAGS data sets are 21.3 events/day and 7.41 events/day, respectively. The difference in the detector response for natural Ge and natural Si with and without J. Gombas *et al.* TAGS data sets are 0.52% and 0.54% deviation. The spectra with excited states correction using the Gross Theory contributes to a 3.3 to 3.8% increment in the detector response.

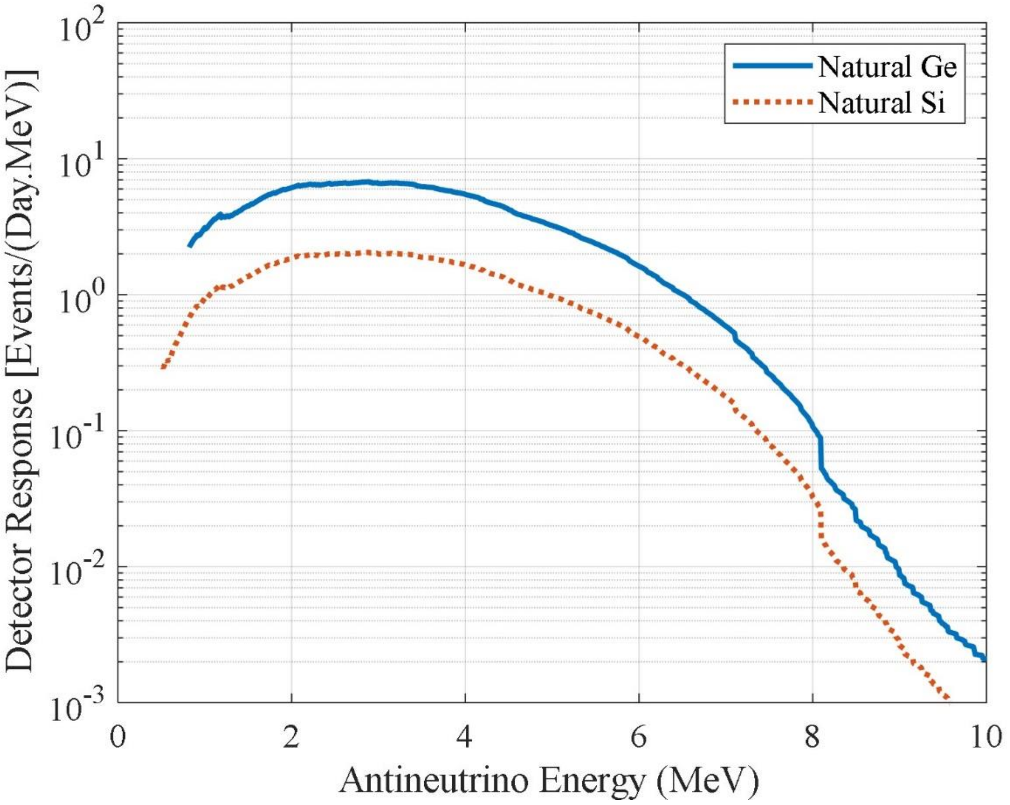

Figure 2-13 Detector response as a function antineutrino energy for natural Ge and natural Si with a threshold (20 eV nuclear recoil), for a 100 kg detector, 10 m from the core.

Figure 2-13 shows the detector response as a function antineutrino energy for natural Ge and natural Si with an energy threshold of 20 eV nuclear recoil energy. The detector response was calculated using corrected spectra and it yields 20.57 events/day for natural Ge and 7.18 events/day for natural Si. Overall, the detector response of natural Ge detector is higher than natural Si detector by a factor 2.86. However, the natural Si detector is more sensitive at lower energies where it can detect anything above 0.51 MeV, corresponding to a 20 eV recoil energy threshold compared to 0.82 MeV of natural Ge detector.

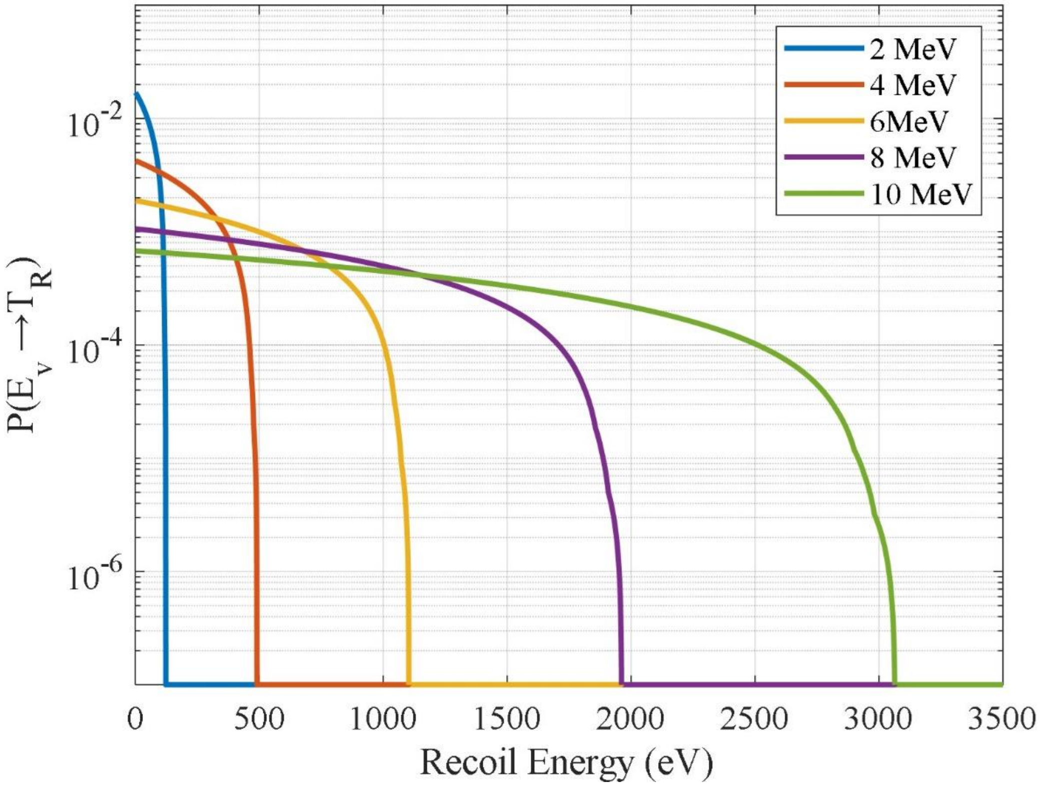

Figure 2-14 The probability distribution of nuclear recoil energies for a given incident antineutrino energy in a natural Ge detector.

Figure 2-14 shows the probability distribution of nuclear recoil energies for a given incident antineutrino energy with a natural Ge detector. Figure 2-14 also shows the maximum recoil energies that can be limited by the incident antineutrino energy and the type of materials. The maximum recoil energies that can be produced in a natural Ge detector for 2 MeV, 4 MeV, 6 MeV, 8 MeV and 10 MeV are 122 eV, 490 eV, 1104 eV, 1962 eV and 3066 eV, respectively. These values will change with different incident antineutrino energies and different types of semiconductor materials.

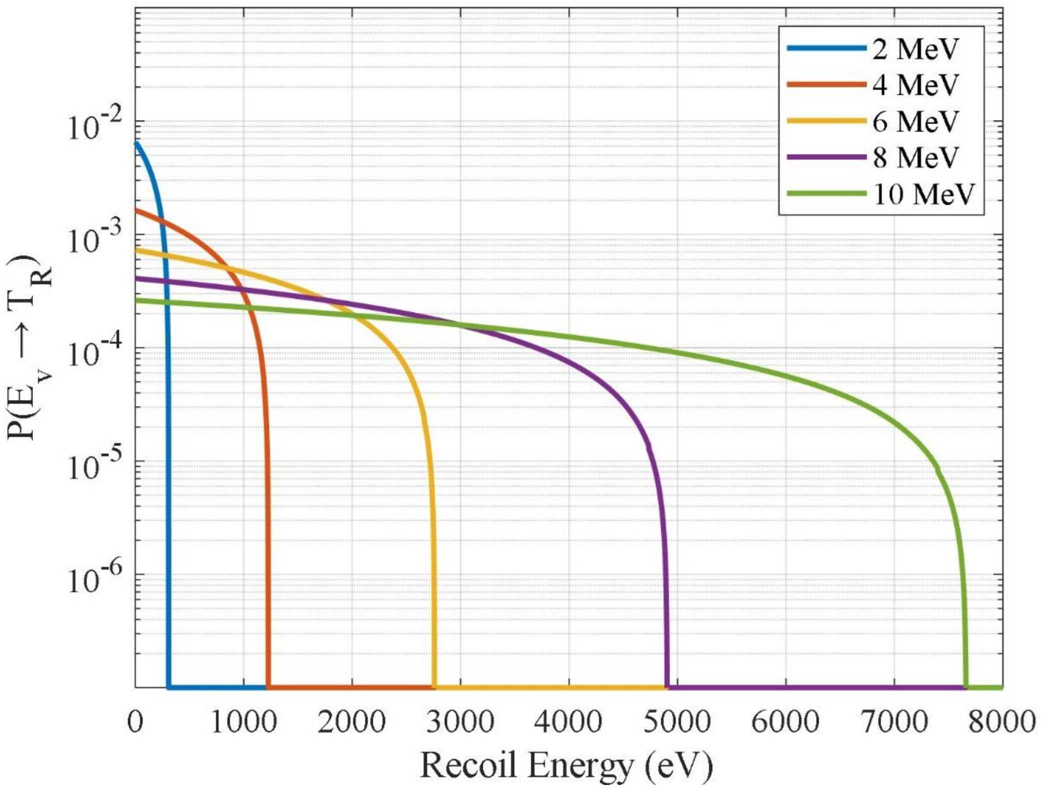

Figure 2-15 The probability distribution of nuclear recoil energies for a given incident antineutrino energy in a natural Si detector.

For natural Si, Fig. 2-15 shows the probability of nuclear recoil energies for a given incident antineutrino energy has the same trend as natural Ge, where the probability of recoil energy decreases at higher recoil energy. However, the maximum recoil energy of natural Si is higher because the mass of Si is lighter than natural Ge, as in Eq. 2-12. The maximum recoil energies that can be produced in a natural Si detector for 2 MeV, 4 MeV, 6 MeV, 8 MeV and 10 MeV are 306 eV, 1226 eV, 2759 eV, 4904 eV and 7662 eV, respectively. These values will change with different incident antineutrino energies and different types of semiconductor materials.

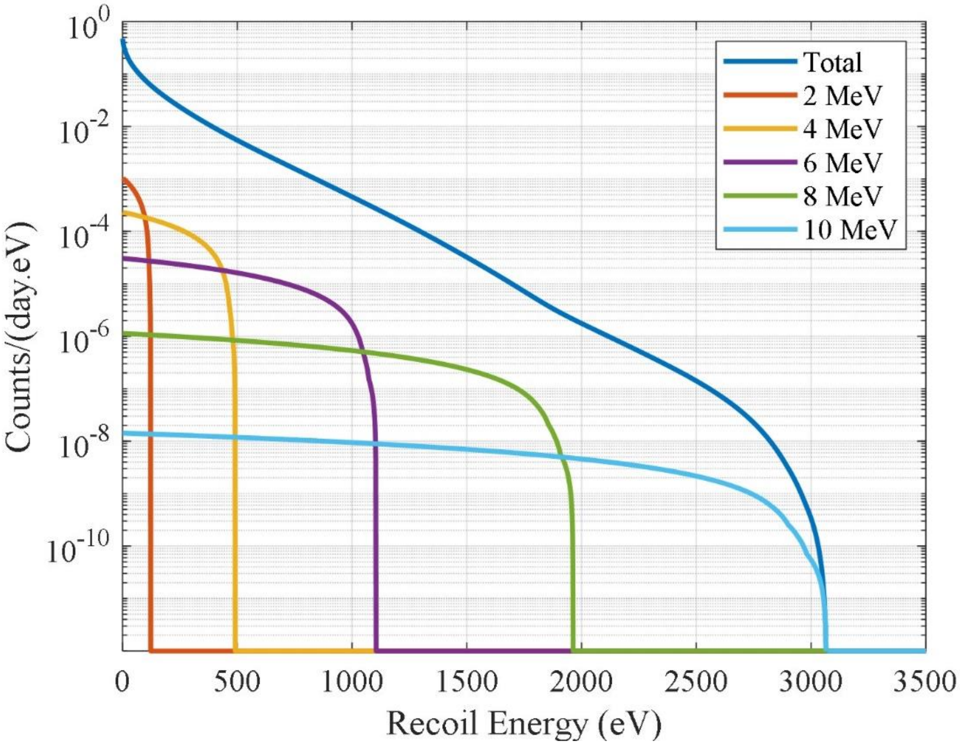

Figure 2-16 The calculated pulse height distribution from a natural Ge detector.

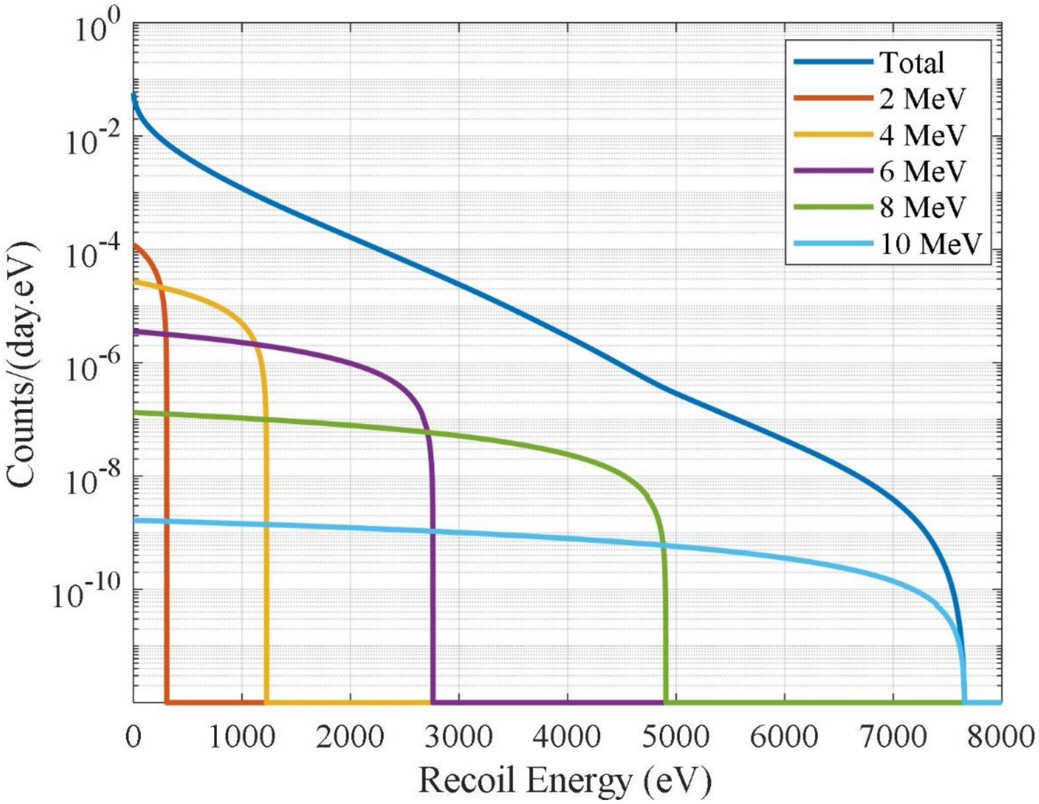

Figure 2-17 The calculated pulse height distribution from a natural Si detector.

Lastly, Figs. 2-16 and 2-17 show the pulse height distribution as a function of recoil energy, when a 100 kg natural Ge or natural Si detectors are placed 10 m away from the reactor. Overall, the pulse height distributions decrease when the nuclear recoil energies increase. The maximum threshold of recoil energies is different for both natural Ge and natural Si due to the difference in their masses

2.5. Conclusion

In this work, we demonstrate the sensitivity of the reactor antineutrino spectrum in the calculation of the CEνNS detector response to a 1 MW research reactor at Texas A&M University. We show that the antineutrino spectrum from a nuclear reactor is very sensitive to the excited states of the various fission products isotopes. The reactor antineutrino spectrum is obtained using the summation method where the individual antineutrino spectra from all fission products undergoing beta-decay are summed. The detector responses and pulse height distributions are obtained by convolving the calculated CEνNS macroscopic cross-sections and the antineutrino spectrum emitted from the reactor.

The antineutrino spectrum without the excited states results in overestimation of detector response by more than 38%. First, most excited states were included using the beta-decay data available in ENDF/B-VIII.0. Some beta intensity data are not available in the ENDF/B-VIII.0, and assuming 100% beta intensity due to the ground state only, results in a 3.3 to 3.8% error in the results. Thus, contributions of missing excited states were included using the Gross Theory. In our study, we have used the continuous beta spectrum from JENDL-2015 to fill-in those isotopes that don't have beta intensity information in the ENDF/B-VIII.0 library. The finite size, radiative, and weak magnetism corrections result in a 0.7 to 0.9% increment in the detector response. To mitigate the issue of the pandemonium effect, not possible using the ENDF/B-VIII.0 library for some isotopes, we included the TAGS data from published literature including the newest TAGS results from J. Gombas *et al.* (2021). Our analysis shows there is a 1.7 to 1.8% decrease in the detector response by including the TAGS data set. In conclusion, excited states correction should be given priority when modelling the reactor antineutrino spectra, as their contributions to the detector response are high compared to others. On the other hand, Ishimoto's approximation method provides a similar result to the summation method such that only

0.88% and 0.42% deviation is observed for natural Ge and natural Si response, respectively. We note that the approximation method using Ishimoto's approach can be a faster way to model antineutrino spectrum for preliminary research study purposes.

In this paper, we also demonstrate that natural Ge detector has better detection efficiency with 20.57 events/day when compared to 7.18 events/day from natural Si detector. However, the natural Si detector (0.51 MeV with 20 eV nuclear recoil threshold) is more sensitive at lower energies compared to the natural Ge detector (0.82 MeV with 20 eV nuclear recoil threshold). We present the probability distribution of recoil energies for a given incident antineutrino energy, where the probability of nuclear recoil energy is a decreasing function. The pulse shape distribution for both natural Ge and natural Si detectors also show a similar behaviour where the number of counts is higher at lower nuclear recoil energies. The study also demonstrates different materials have different recoil thresholds. Overall, lower mass nuclides have higher lower nuclear recoil thresholds in terms of minimum detectable incident antineutrino energy.

2.6. References

[1] D. Akimov, J. B. Albert, P. An et al., Observation of Coherent Elastic Neutrino-Nucleus Scattering, *Science* 357, 1123, 2017, doi:10.1126/science.aao0990.

[2] M. Bowen and P. Huber, Reactor Neutrino Applications and Coherent Elastic Neutrino Nucleus Scattering, *Phys. Rev.* D 102, 053008, 2020, doi: 10.1103/PhysRevD.102.053008.

[3] A. Oralbaev, M. Skorokhvatov, and O. Titov, The Inverse Beta Decay: A Study of Cross Section, *J. Phys.: Conf. Ser.* 675, 012003, 2016, doi: 10.1088/1742-6596/675/1/012003.

[4] W. E. Ang, S. Prasad, and R. Mahapatra, Coherent Elastic Neutrino Nucleus Scatter Response of Semiconductor Detectors to Nuclear Reactor Antineutrinos, *Nuclear Instruments and Methods in Physics Research Section* A: Accelerators, Spectrometers, Detectors and Associated Equipment 1004, 165342, 2021, doi: 10.1016/j.nima.2021.165342.

[5] H. Neog, R. Mahapatra, N. Mirabolfathi et al., Phonon-Mediated High-Voltage Detector with Background Rejection for Low-Mass Dark Matter and Reactor Coherent Neutrino Scattering Experiments, 2020. ArXiv:2006.13139 [Hep-Ex, Physics:Physics].

[6] C. Stewart and A. Erickson, Antineutrino Analysis for Continuous Monitoring of Nuclear Reactors: Sensitivity Study, *Journal of Applied Physics* 118, 164902, 2015, doi: 10.1063/1.4934638.

[7] G. F. Knoll, Radiation Detection and Measurement, 4th ed. (Wiley, 2010).

[8] A. C. Hayes and P. Vogel, Reactor Neutrino Spectra, *Annual Review of Nuclear and Particle Science* 66, 219, 2016, doi: 10.1146/annurev-nucl-102115-044826.

[9] K. Schreckenbach, G. Colvin, W. Gelletly, and F. Von Feilitzsch, Determination of the Antineutrino Spectrum from ^{235}U Thermal Neutron Fission Products up to 9.5 MeV, *Physics Letters* B 160, 325, 1985, doi: 10.1016/0370-2693(85)91337-1.

[10] T. A. Mueller, D. Lhuillier, M. Fallot et al., Improved Predictions of Reactor Antineutrino Spectra, *Phys. Rev.* C 83, 054615, 2011, doi: 10.1103/PhysRevC.83.054615.

[11] P. Huber, On the Determination of Anti-Neutrino Spectra from Nuclear Reactors, *Phys. Rev.* C 84, 024617, 2011, doi: 10.1103/PhysRevC.84.024617.

[12] N. Haag, A. Gütlein, M. Hofmann et al., Experimental Determination of the Antineutrino Spectrum of the Fission Products of ^{238}U, *Phys. Rev. Lett.* 112, 122501, 2014, doi: 10.1103/PhysRevLett.112.122501.

[13] P. Novella, The Antineutrino Energy Structure in Reactor Experiments, *Advances in High Energy Physics* 2015, 364392, 2015, doi: 10.1155/2015/364392.

[14] A. Algora, J. L. Tain, B. Rubio et al., Beta-Decay Studies for Applied and Basic Nuclear Physics, *Eur. Phys. J.* A 57, 85, 2021, doi: 10.1140/epja/s10050-020-00316-4.

[15] P. Vogel, G. K. Schenter, F. M. Mann et al., Reactor Antineutrino Spectra and Their Application to Antineutrino-Induced Reactions. II, *Phys. Rev.* C 24, 1543, 1981, doi: 10.1103/PhysRevC.24.1543.

[16] S. Rice, E. Valencia, A. Algora et al., Decay Heat Measurements Using Total Absorption Gamma-Ray Spectroscopy, *J. Phys.: Conf. Ser.* 381, 012056, 2012, doi: 10.1088/1742-6596/381/1/012056.

[17] E. Aguado and M. Esther, TAS measurements for neutrino physics and nuclear structure: study of the beta decays of 150Er, 152, 156Yb, and 188, 190, 192Pb, Thesis, 2012.

[18] M. Fallot, A. Porta, L. L. Meur et al., Total Absorption Spectroscopy of Fission Fragments Relevant for Reactor Antineutrino Spectra, *EPJ Web Conf.* 146, 10002, 2017, doi: 10.1051/epjconf/201714610002.

[19] J. C. Hardy, L. C. Carraz, B. Jonson, and P. G. Hansen, The Essential Decay of Pandemonium: A Demonstration of Errors in Complex Beta-Decay Schemes, *Physics Letters* B 71, 307, 1977, doi: 10.1016/0370-2693(77)90223-4.

[20] M. Estienne, M. Fallot, L. Giot et al., Summation Calculations for Reactor Antineutrino Spectra, Decay Heat and Delayed Neutron Fractions Involving New TAGS Data and Evaluated Databases, *EPJ Web Conf.* 211, 01001, 2019, doi: 10.1051/epjconf/201921101001.

[21] ENDF/B-VIII.0 Evaluated Nuclear Data Library. [Online]. Available: https://www.nndc.bnl.gov/endf/b8.0/.

[22] JENDL/DDF-2015. [Online].
Available: https://wwwndc.jaea.go.jp/ftpnd/jendl/jendl-ddf-2015.html.

[23] JEFF-3.3. [Online].
Available: https://www.oecd-nea.org/dbdata/jeff/jeff33/index.html.

[24] Evaluated and Compiled Nuclear Structure Data. [Online].
Available: https://www.nndc.bnl.gov/ensdf/.

[25] T. Kawano, P. Möller, and W. B. Wilson, Calculation of Delayed-Neutron Energy Spectra in a Quasiparticle Random-Phase Approximation--Hauser-Feshbach Model, *Phys. Rev.* C 78, 054601, 2008, doi: 10.1103/PhysRevC.78.054601.

[26] K. Takahashi and M. Yamada, Gross Theory of Nuclear β-Decay, *Progress of Theoretical Physics* 41, 1470, 1969, doi: 10.1143/PTP.41.1470.

[27] H. Koura, T. Yoshida, T. Tachibana et al., Improvement of Gross Theory of Beta-Decay for Application to Nuclear Data, *EPJ Web Conf.* 146, 12003, 2017, doi: 10.1051/epjconf/201714612003.

[28] V. I. Kopeikin, Flux and Spectrum of Reactor Antineutrinos, *Phys. Atom. Nuclei* 75, 143, 2012, doi: 10.1134/S1063778812020123.

[29] R. C. Greenwood, M. H. Putnam, and K. D. Watts, Ground-State β−-Branching Intensities of Several Fission-Product Isotopes Measured Using a Total Absorption γ-Ray Spectrometer, *Nuclear Instruments and Methods in Physics Research Section A: Accelerators, Spectrometers, Detectors and Associated Equipment* 378, 312, 1996, doi: 10.1016/0168-9002(96)00209-4.

[30] A. Algora, D. Jordan, J. L. Taín et al., Reactor Decay Heat in ^{239}Pu: Solving the γ Discrepancy in the 4–3000-s Cooling Period, *Phys. Rev. Lett.* 105, 202501, 2010, doi: 10.1103/PhysRevLett.105.202501.

[31] A. A. Zakari-Issoufou, M. Fallot, A. Porta et al., Total Absorption Spectroscopy Study of ^{92}Rb Decay: A Major Contributor to Reactor Antineutrino Spectrum Shape, *Phys. Rev. Lett.* 115, 102503, 2015, doi: 10.1103/PhysRevLett.115.102503.

[32] S. Rice, A. Algora, J. L. Tain et al., Total Absorption Spectroscopy Study of the β Decay of ^{86}Br and ^{91}Rb, *Phys. Rev.* C 96, 014320, 2017, doi: 10.1103/PhysRevC.96.014320.

[33] L. M. Loic, Thesis, L'Universite de Nantes, 2018.

[34] V. Guadilla, A. Algora, J. L. Tain et al., TAGS Measurements of ^{100}Nb Ground and Isomeric States and ^{140}Cs for Neutrino Physics with the New DTAS Detector, *EPJ Web Conf.* 146, 10010, 2017, doi: 10.1051/epjconf/201714610010.

[35] J. Gombas, P. A. DeYoung, A. Spyrou et al., β-Decay Feeding Intensity Distributions for ^{103,104m}Nb, *Phys. Rev.* C 103, 035803, 2021, doi: 10.1103/PhysRevC.103.035803.

[36] B. Dutta, R. Mahapatra, L. E. Strigari et al., Sensitivity to Z-Prime and Non-Standard Neutrino Interactions from Ultra-Low Threshold Neutrino-Nucleus Coherent Scattering, *Phys. Rev.* D 93, 013015, 2016, doi: 10.1103/PhysRevD.93.013015.

[37] A. C. Hayes, J. L. Friar, G. T. Garvey et al., Systematic Uncertainties in the Analysis of the Reactor Neutrino Anomaly, *Phys. Rev. Lett.* 112, 202501, 2014, doi: 10.1103/PhysRevLett.112.202501.

[38] V. B. Berestetskii, E. M. Lifshitz, and L. P. Pitaevskii, Chapter XII - Radiative Corrections, in Quantum Electrodynamics (Second Edition), edited by V. B. Berestetskii, E. M. Lifshitz, and L. P. Pitaevskii (Butterworth-Heinemann, Oxford, 1982), pp. 501–596.

[39] A. Sirlin, Radiative Correction to the $\bar{\nu}_e(\nu_e)$ Spectrum in β Decay, *Phys. Rev.* D 84, 014021, 2011, doi: 10.1103/PhysRevD.84.014021.

[40] J. Erler and S. Su, The Weak Neutral Current, *Progress in Particle and Nuclear Physics* 71, 119, 2013, doi: 10.1016/j.ppnp.2013.03.004.

[41] P. Coloma, I. Esteban, M. C. Gonzalez-Garcia et al., Determining the Nuclear Neutron Distribution from Coherent Elastic Neutrino-Nucleus Scattering: Current Results and Future Prospects, *J. High Energ. Phys.* 2020, 30, 2020, doi: 10.1007/JHEP08(2020)030.

[42] K. Scholberg, Observation of Coherent Elastic Neutrino-Nucleus Scattering by COHERENT, 2018. ArXiv:1801.05546 [Astro-Ph, Physics:Hep-Ex, Physics:Hep-Ph, Physics:Nucl-Ex, Physics:Physics].

[43] D. A. Sierra, V. De Romeri, and N. Rojas, COHERENT Analysis of Neutrino Generalized Interactions, *Phys. Rev.* D 98, 075018, 2018, doi: 10.1103/PhysRevD.98.075018.

[44] Tables of Nuclear Data. [Online]. Available: https://wwwndc.jaea.go.jp/NuC/.

[45] S. Ishimoto, T. Omori, H. Arima, and K. Ishibashi, Simple Calculation of Reactor Antineutrino Energy Spectrum by the Use of Nuclear Data Libraries, *Journal of Nuclear Science and Technology* 39, 670, 2002, doi: 10.1080/18811248.2002.9715248.

3. COHERENT ELASTIC NEUTRINO NUCLEUS SCATTER RESPONSE OF SEMICONDUCTOR DETECTORS TO NUCLEAR REACTOR ANTINEUTRINOS*

3.1. Introduction

The existing methods of antineutrino detection utilize inverse beta decay (IBD). However, recently CEνNS based detectors have shown promising results that make them candidates for measuring antineutrino energies in the sub-MeV region (corresponding to detection of nuclear recoil energy from 10 eV to 20 eV) [1]. Another benefit of CEνNS is that the cross-section can be two-four orders of magnitude higher than IBD, thus, small detectors weighing a few kilograms can be fabricated in contrast to IBD detector weighing several tons, if not kilo-tons [2]. The CEνNS detectors, however, require additional cooling to very low temperature such as 30 mK [3]. Background radiation can seriously hinder the CEνNS detector capability to discriminate electron-recoil and nuclear-recoil interactions, which is beyond the scope of this study. This study was conducted using the 1 MW(th) TRIGA reactor Nuclear Science Center at Texas A&M University as a reference. The objective of this study is to demonstrate CEνNS detector response as a function of initial antineutrino energy using a 100 kg detector and placed 10 m away from the core. Nuclear reactors have long been used to study antineutrino and their characteristics in the past 50 years [4]. Fission products produced from ^{235}U, ^{238}U, ^{239}Pu

---

*Reprinted with permission from "Coherent elastic neutrino nucleus scatter response of semiconductor detectors to nuclear reactor antineutrinos," by W. E. Ang, S. Prasad, and R. Mahapatra July 2021. *Nuclear Instruments and Methods in Physics Research Section A: Accelerators, Spectrometers, Detectors and Associated Equipment*, Vol. 1004, p. 165342 with minor updates.

and ^{241}Pu via fission reaction will undergo β− decay, followed by electron and antineutrino production. Therefore, antineutrino detection can be used to determine information such as nuclear power, fuel composition and burnup [5]. Two semiconductor candidates: germanium and silicon are compared to determine their detection efficiency and energy sensitivity [6]. In this work, only the CEνNS reaction rates in semiconductor materials are modeled. The ionization process, quenching, and phonon production rates have not been included. Fig. 3-1 shows a cryogenic detector developed for the SuperCDMS experiment [7].

Figure 3-1 Cryogenically cooled Ge/Si detectors with photo lithographically patterned Transition Edge Sensors provide energy and position information. These detectors utilize the technology developed for the Super CDMS experiment. Each detector measures about 1.6 kg [8].

3.2. Methodology

There are two approaches to model a fission antineutrino spectrum, either using '*ab initio*' summation method or the electron spectrum conversion method [9]. The '*ab initio*' summation method is a method where all the normalized antineutrino spectra contributed from the various (several hundred) fission fragments are summed together. The electron spectrum conversion method is an experimental approach in which the samples of ^{235}U, ^{238}U, ^{239}Pu and ^{241}Pu are irradiated and the electron spectrum from each is measured. Then, electron spectrum from each isotope is converted into antineutrino spectrum by using conservation of energy by substituting E_β with $\left(E_{\beta max} - E_v\right)$ using Eq. 3-2. In our study, we used the summation method to calculate the antineutrino spectra from various fissions fragments, using fission yields data from JEFF-3.3 and decay data from ENDF/B-VIII.0 [10] [11]. Both fission yields and decay data were extracted and processed using both Python and Matlab programs.

3.2.1. Antineutrino spectrum calculation

An antineutrino spectrum of mixture of fission products can be expressed as:

$$\rho(E_v) = \sum\nolimits_i CY_i \sum\nolimits_i BR_i P_i(E_v) \qquad (3\text{-}1)$$

where i is individual fission product, CY is the cumulative yield of the fission product, BR_i is the branching ratio of β decay, and P_i is the antineutrino spectrum for a fission product [9]. A total of 654 fission products from each isotope: ^{235}U, ^{238}U, ^{239}Pu and ^{241}Pu (whose cumulative yields were greater than 10^{-6}) were used in this study [12]. The antineutrino emission spectrum for a fission product, i can be written as [13]:

$$P_i(E_v)dE_v = F(Z, E_v)\left[\left(E_{\beta max} - E_v\right)^2 - m_0^2c^4\right]^{\frac{1}{2}} \times E_v^2\left(E_{\beta max} - E_v\right) \qquad (3\text{-}2)$$
$$\times F_a(E_v) \times dE_v/F_i$$

In our calculation, $F(Z, E_v)$ is the Fermi function, Z is the atomic number, E_v is the initial antineutrino energy incident on the detector, m_0 is electron rest mass, c is the speed of light, $E_{\beta max}$ is approximately $Q + m_0c^2$ where Q is reaction Q-value. F_i is defined as:

$$F_i = \int_{m_0c^2}^{E_{\beta max}} F(Z, E_\beta) \times \left(E_\beta - m_0^2c^4\right)^{\frac{1}{2}} \times \left(E_{\beta max} - E_\beta\right)^2 E_\beta dE_\beta \tag{3-3}$$

$F_a(E_v)$ is a correction factor that is used to adjust the uncertainties that arise from spin, parity, allowed and forbidden transitions, which are energy dependent. $F_a(E_v)$ is proposed by Shunsuke Ishimoto *et al.* (2012) and the equation is defined as [13]:

$$F_a(E_v) = C(1 - E_v/E_{max})^n \tag{3-4}$$

where *C* is a constant, E_{max} is beta-decay Q value, and *n* is an adjustable parameter. In our study, *n*=1.5 is used, as suggested by Shunsuke Ishimoto *et al.* [13]. Fig. 3-2 shows the number of antineutrinos produced from each actinide based on summation method.

The Fermi function, $F(Z, E_v)$ here is used to account for the Coulomb field on the shape of the beta spectrum as the daughter nucleus slows down the electron and accelerates the positron. The relativistic Fermi Function is given by [14]:

$$F(Z, W) = \frac{2(1 + S)}{\left((2S)!\right)^2}(2p\rho)^{2S-2}e^{\pi\eta}|(S - 1 + i\eta)!|^2 \tag{3-5}$$

where $S = (1 - \alpha^2Z^2)^{\frac{1}{2}}$, $\rho = R/(\hbar/mc)$, and $\eta = \pm(Ze^2/\hbar V)$. Here *R* is the radius of nucleus, α is the fine structure constant (~1/137), Z is the nuclear charge of daughter nucleus, $\hbar$ is reduced Plank's Constant, and *V* is the speed of the beta particle. The + sign corresponds to electron while – sign correspond to positron.

However, the calculation of relativistic Fermi function can be complicated. Thus, several simplified Fermi functions have been proposed to make calculations easier. The simplified Fermi function used in this study are proposed by Nilsson (1956) which has one-half percent error [14].

$$F(Z,W) \approx a\frac{W}{p} + \left[\frac{c}{1+(d/\,p^2)}\right] \tag{3-6}$$

where $a = 2\pi\alpha Z$, $C = b - a$, $b = a/(1 - e^{-a})$, and $d = (\frac{1}{2})(b - 1)$.

3.2.2. CEνNS cross-section calculation

CEνNS cross-section has a direct Standard Model (SM) prediction as shown below [1]:

$$\frac{d\sigma}{dT_R} = \frac{G_F^2 M}{2\pi}[(q_v + q_A)^2 + (q_v - q_A)^2\left(1 - \frac{T_R}{E_v}\right)^2 - (q_v^2 - q_A^2)\frac{MT_R}{E_v^2}] \tag{3-7}$$

Integrating Eq. 3-7 one obtains Eq. 3-8 in order to obtain the CEνNS cross-section as a function of the incident antineutrino energy. The integrated CEνNS is shown below:

$$\sigma(E_v) = \int_{T_R min}^{T_R max} A_1T_R + A_2T_R - \frac{A_2T_R^2}{E_v} + \frac{A_2T_R^3}{3{E_v}^2} - \frac{A_3MT_R^2}{2{E_v}^2} \tag{3-8}$$

where G_F denotes the Fermi constant, M is the mass of targeted nucleus, q_v and q_A are vector and axial charges respectively, T_R is detectable recoil energy and E_v is incident neutrino energy. The maximum recoil energy can be calculated by [1]:

$$T_R^{Max} = \frac{2E_v^2}{M + 2E_v} \tag{3-9}$$

A_1, A_2 and A_3 here are constants where:

$$A_1 = \frac{G_F^2 M}{2\pi}(q_v + q_A)^2 \qquad (3\text{-}10)$$

$$A_2 = \frac{G_F^2 M}{2\pi}(q_v - q_A)^2 \qquad (3\text{-}11)$$

$$A_3 = \frac{G_F^2 M}{2\pi}(q_v^2 - q_A^2) \qquad (3\text{-}12)$$

The vector charges, q_v is defined as [15]:

$$q_v = g_v^p Z + g_v^n N \qquad (3\text{-}13)$$

where g_v^p and g_v^n are vector proton and neutron weak neutral current (NC) couplings respectively. The SM weak parameters were obtained from Jens Erler *et al.* (2013) and used in study: $g_v^p = 0.0298$ and $g_v^n = -0.5117$ [15]. The nuclear scattering will typically be dominated by the vector charge and axial terms are small by a factor $1/N^2$, where N is number of neutrons in the target nucleus [1]. In addition, nuclei with even number of protons and neutrons have a zero spin, thus the axial terms, q_A vanish [16]. Figure 3-3 in the "Results and Discussion" session shows the CEvNS cross-section as a function of incident antineutrino energy for natural Ge and natural Si. Table 3-1 and 3-2 are tabulated from Nuclear Data Center, Japan Atomic Energy Agency to assist the CEvNS cross-section calculation [18].

Table 3-1 Natural Ge with its isotopes and abundance.

Nuclides	Weight (amu)	Abundance (%)
^{70}Ge	69.92	20.57
^{72}Ge	71.92	27.45
^{73}Ge	72.92	7.75
^{74}Ge	73.92	36.50
^{76}Ge	75.92	7.73

Table 3-2 Natural Si with its isotopes and abundance.

Nuclides	Weight (amu)	Abundance (%)
^{28}Si	27.98	92.223
^{29}Si	28.98	4.685
^{30}Si	29.97	3.092

The IBD cross-section is also calculated for comparison purpose. IBD cross-section^2 is defined as below according to A. Oralbaev (2016):

$$\sigma_0(E_v) = \frac{1}{\pi}(G_V^2 + 3G_A^2)\bar{p}\bar{E} \tag{3-14}$$

where $\bar{E}$ and $\bar{p}$ is momentum, G_V and G_A are the effective beta decay constants defined through the Fermi constant. The IBD calculation was made based on Precision Reactor and Spectrum Experiment (PROSPECT) which using ^{6}Li-doped liquid scintillator EJ-309 for antineutrino detection [19].

3.2.3. Detector response calculation

We calculate the detector response reaction rates in terms of incident antineutrino energy:

$$R(E_v) = N\sigma(E_v)\phi(E_v) \tag{3-15}$$

where N is the number of nuclides, σ is the CEνNS cross-section and ϕ is the antineutrino flux. By convolving the results of antineutrino flux spectrum and CEνNS cross-sections as shown in Fig. 3-2 and Fig. 3-3, the detector responses of natural Ge and natural Si in Fig. 3-4 are generated.

In our study, we also demarcated the minimum antineutrino energy required to trigger a 20 eV nuclear recoil for both Ge and Si, which is defined as [1]:

$$E_{min} = \frac{T_R + \sqrt{2MT_R + T_R^2}}{2} \tag{3-16}$$

3.3. Result and discussion

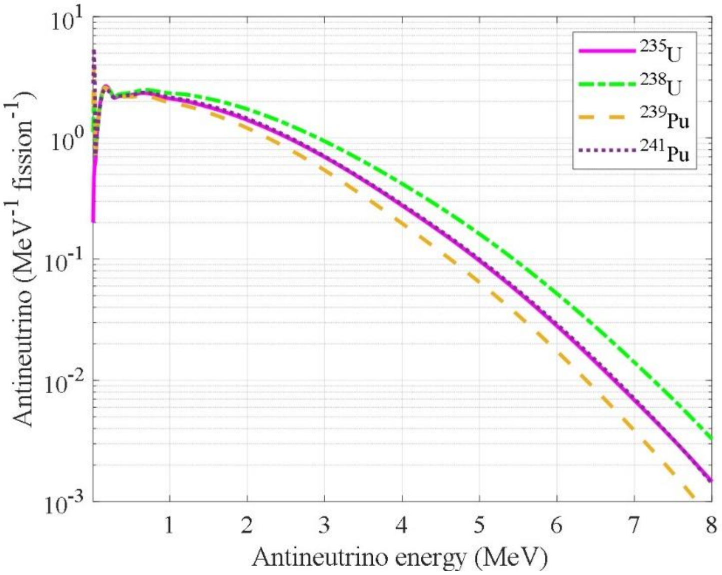

Figure 3-2 Calculated antineutrino spectra as a function of energy for the primary fissionable isotopes.

Fig. 3-2 shows the antineutrino spectra as a function of energy for each, ^{235}U, ^{238}U, ^{238}Pu, and ^{241}Pu. The ^{238}U has the hardest spectrum and ^{239}Pu has the softest spectrum. Based on our calculation using nuclear data from JEFF-3.3, ^{238}U has the highest antineutrino production rate at 7.11 antineutrinos per fission while ^{239}Pu is the least with 5.46 antineutrinos per fission. Additionally, the ^{238}U will also breed ^{239}Pu through neutron capture after capturing a neutron to produce ^{239}U, which then decays to ^{239}Np, finally yielding ^{239}Pu, via a beta decay reaction. This capture event also contributes to antineutrino production. The average number of antineutrino emissions per fission (N_ν) and its average energies (E_ν) produced by these isotopes are tabulated into Table 3-3.

Table 3-3 The average number of antineutrino emission ($\boldsymbol{N_\nu}$) and its average energies ($\boldsymbol{E_\nu}$) for ^{235}U, ^{238}U, ^{239}Pu and ^{241}Pu.

Actinides	E_ν (MeV)	N_ν (per fission)
^{235}U	1.53	6.04
^{238}U	1.67	7.11
^{239}Pu	1.40	5.46
^{241}Pu	1.51	6.23
^{238}U to ^{239}Pu	0.60	2.00

The production rates of antineutrino depend on the fission fraction of ^{235}U, ^{238}U, ^{239}Pu and ^{241}Pu. A detailed fission fraction calculation requires knowledge of core fuel composition, neutron flux, fuel burnup and the reactor's operation history (such as refueling period, fuel assembly layout etc.). Typical fission fractions of the TAMU TRIGA reactor for ^{235}U, ^{238}U, ^{239}Pu, ^{241}Pu and capture event are 0.967, 0.013, 0.020, 0.001, and 0.16 respectively. The fission rate of this TRIGA reactor is 3.1×10^{16} s^{-1}. The calculated antineutrino production rate of TAMU reactor is 1.88×10^{17} s^{-1} and antineutrino flux is approximately 1.50×10^{10} cm^{2}s^{-1} at a distance of 10 m. Overall, 1 MW(th) TRIGA reactor yields about 6.01 antineutrinos per fission.

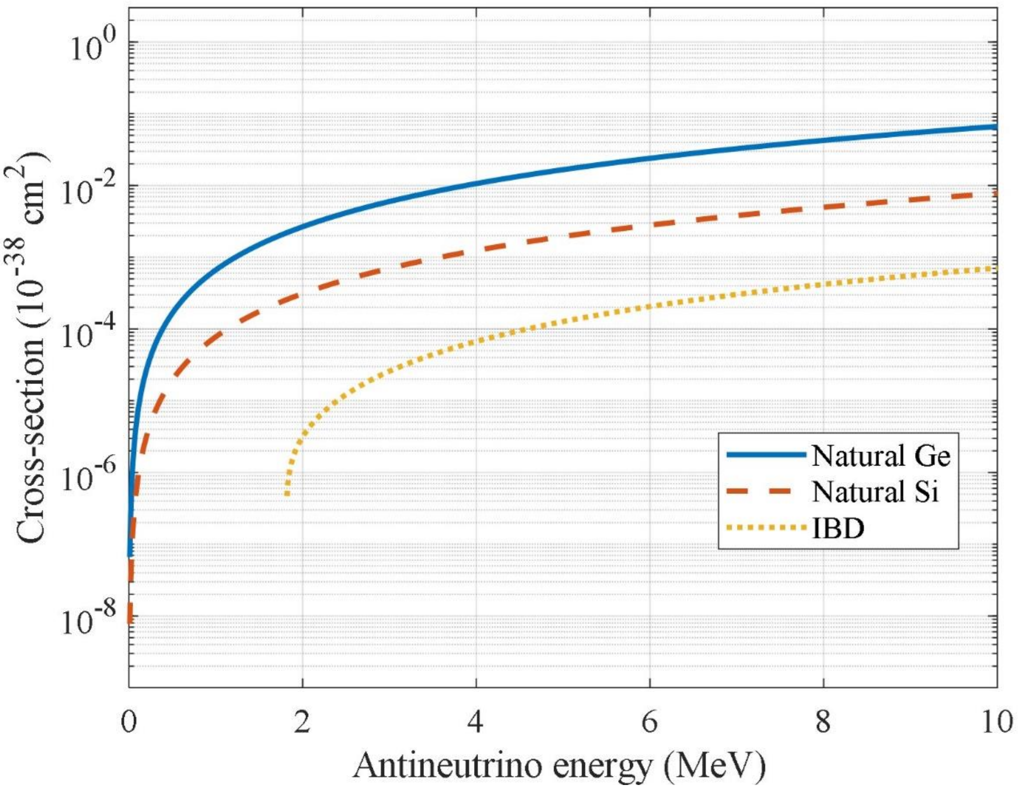

Figure 3-3 Calculated CEνNS microscopic cross-section as a function of energy for natural Ge, natural Si and IBD. Natural Ge projects the highest cross-section for energies of interest.

Fig. 3-3 shows the difference of CEνNS cross-section between natural Ge, natural Si and IBD. The flux weighted average CEνNS cross-section for natural Ge is 4.35×10^{-40} cm^2 and natural Si is 5.09×10^{-41} cm^2. The average cross-section of natural Ge is approximately one order of magnitude higher than natural Si and two orders of magnitude higher than IBD, which has an average cross-section of 4.56×10^{-42} cm^2. From this result, natural Ge has a higher probability to interact with antineutrinos compared to both natural Si and IBD. The CEνNS cross-sections monotonically increase with increasing incident antineutrino energy above 0.5 MeV. There is no minimum energy threshold for the CEνNS reaction in natural Ge and natural Si. Unlike CEvNS cross-section, IBD cross-section has an energy threshold of 1.806 MeV in order to initiate a response.

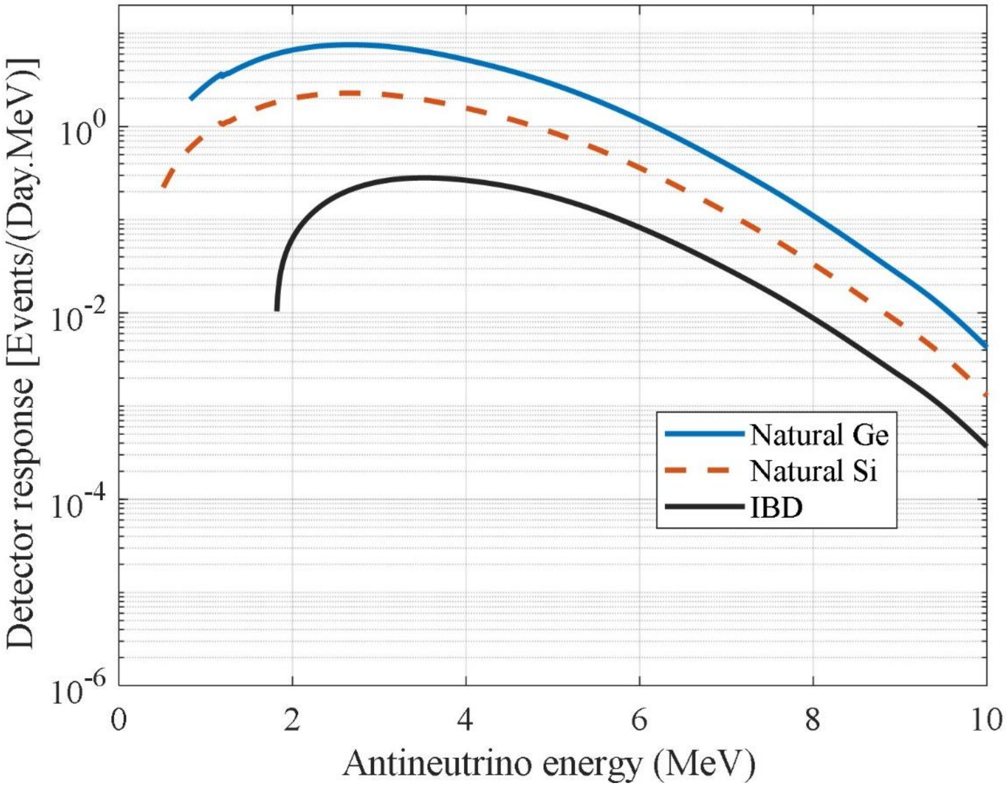

Figure 3-4 Calculated detector response as a function antineutrino energy for natural Ge and natural Si with threshold (20 eV nuclear recoil), for 100 kg detector at 10 m from the core. The above detector response curves do not include background interactions in the detector. Natural Ge provides the highest response, whereas natural Si provides sensitivities at energies as low as 0.51 MeV.

For a 20 eV nuclear recoil threshold, Fig. 3-4 yields ~20.39 events/day in natural Ge, ~7.15 events/day in natural Si and ~0.75 events/day with IBD, in each case a 100 kg detector at a distance of 10 m from the core is modeled. Both Ge and Si response curves have peak at 2.67 MeV antineutrino energy. In general, it is found that natural Ge has a greater detection efficiency than natural Si by a factor of 2.85. However, it is shown that natural Si is sensitive to lower antineutrino energies than natural Ge. The lower threshold of 20 eV nuclear recoil can be produced by a minimum-antineutrino-incident-energy of 0.51 MeV in natural Si, whereas it can be produced minimum-antineutrino-incident-energy of 0.82 MeV in natural Ge. It is found that a 100 eV nuclear recoil in natural Ge and natural Si detectors can be produced by a minimum-antineutrino-incident-energy of 1.84 MeV and 1.14 MeV, respectively. Both Ge and Si have higher detection efficiency compared to IBD. For the example, the detection efficiency of Ge is greater than that of IBD by a factor of 27.19. Additionally, the fraction of undetected antineutrinos below the IBD threshold in Fig. 3-2 is 66.17%. In the case of natural Ge and natural Si CEνNS, the undetected antineutrino fractions are reduced to 33.10% and 20.26% respectively, with 20 eV nuclear recoil threshold. For 100 eV nuclear recoil threshold, it is found that undetected antineutrino fractions are 66.95% and 46.02% for natural Ge and natural Si CEνNS respectively.

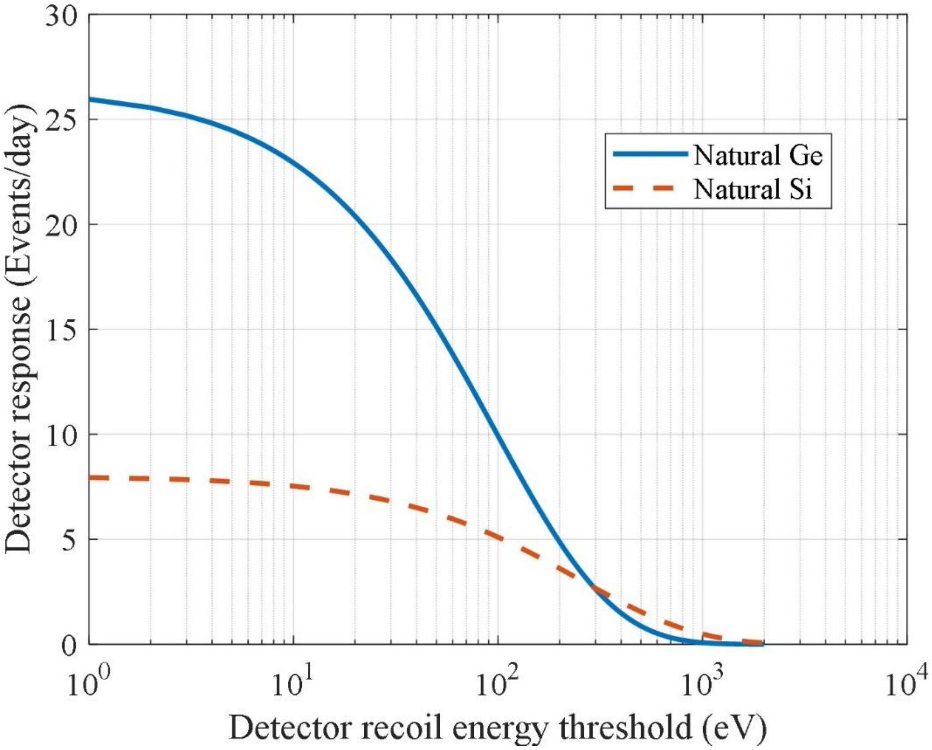

Figure 3-5 Detector response (events per day) captured as a function of nuclear recoil detection threshold energy (eV) in natural Ge and natural Si detectors.

Fig. 3-5 shows the detector response (events per day) for natural Ge and natural Si detectors as a function of nuclear recoil detection threshold following a CEvNS event. Overall, natural Ge detector captures more events compared to natural Si detector. The detection rate for both detectors decreases when the detector recoil energy threshold increases, this effect is more pronounced in the case of antineutrinos detection because a significant portion of the antineutrino spectrum lies at lower energies, as in Fig. 3-2.

The results shown in this work have not included any background reduction or elimination. The background levels measured by the detector greatly affect the ability to measure true CEvNS events in an actual measurement, as shown by MINER and other similar experiment [20]. The advantage of the SuperCDMS technology detector lies with its capability to discriminate between electron-recoil and nuclear-recoil interactions that can be produced by both reactor antineutrinos and background radiation such as muons and muon-induced neutrons from cosmic rays [21]. Thus, the CEνNS detector would need to be shielded in order to reduce background gammas and neutrons produced from the core. Further, a perfect energy resolution is being assumed [21].

3.4. Conclusion

Our calculations show that CEνNS detectors have the potential to provide higher detection efficiency compared to IBD. A 100 kg detector using CEνNS mechanism can detect 20.39 events/day in natural Ge and 7.15 events/day in natural Si compared to 0.75 events/day using IBD. We have demonstrated that Ge detectors can be significantly more efficient than Si detectors by a factor of 2.85, and a factor of 27.19 more efficient compared to IBD detector. However, Si is a better semiconductor material candidate than Ge for low energy sensitivity. Si detector can be used to provide antineutrino incident energies to as low as 1.14 MeV for 100 eV nuclear recoil energy and 0.51 MeV for 20 eV nuclear recoil energy. On the other hand, the minimum incident energy to produce a 100 eV and 20 eV nuclear recoil energy in Ge are 1.84 MeV and 0.82 MeV respectively. Due to lower energy sensitivities, semiconductor CEνNS detector can be used to record detector response lower than the current IBD antineutrino energy threshold of 1.806 MeV. This achievement can only be possible once background corrections can be made adequately in both semiconductor materials.

Further, we have studied three different cross-sections: CEνNS cross-section for natural Ge, CEνNS cross-section for natural Si, and the IBD cross-section. The result shows that Ge has the highest flux weighted average CEνNS cross section, an order of magnitude higher compared to the Si-CEνNS cross-section and two orders of magnitude higher than the average IBD cross-section. It is worth noting that an IBD reaction can only be initiated for antineutrinos above 1.806 MeV, leaving nearly half of nearly two-thirds the antineutrinos below this energy-level undetected.

We also analyze the antineutrino flux spectra from the major contributing isotopes: ^{235}U, ^{238}U, ^{239}Pu, and ^{241}Pu. It is shown that ^{238}U has the hardest spectrum among all four fissionable actinides. The ^{238}U produces most antineutrinos at 7.11 antineutrinos per fission and ^{239}Pu produces the least among all four at 5.46 antineutrinos per fission. The antineutrino production rate of typical 1 MW(th) reactor is 1.88×10^{17} s^{-1} and antineutrino flux is approximately 1.50×10^{10} cm^{-2} s^{-1}, at a distance of 10 m from the core. With our choice of 1 MW(th) TRIGA reactor, we obtain an average of 6.01 antineutrinos produced per fission event. We have shown that the nuclear recoil threshold of 20 eV in natural Ge renders 33.10% of antineutrinos undetectable, and in natural Si renders 20.26% undetectable. It is shown that increasing the nuclear recoil threshold to 100 eV in both natural Ge and natural Si renders 66.95% and 46.02% of antineutrinos undetectable, respectively. The existing IBD threshold leaves 66.17% undetectable.

Low energy antineutrinos can provide important information about nuclear fuel, such as fuel composition, the age of the fuel, and its operational history. The CEνNS reaction can make detection of low energy antineutrinos possible. High detection efficiency and smaller size of CEνNS detectors would open a new window of opportunity for their use in reactor security and non-proliferation safeguards.

3.5. References

[1] B. Dutta, R. Mahapatra, L. E. Strigari, and J. W. Walker, Sensitivity to Z-Prime and Non-Standard Neutrino Interactions from Ultra-Low Threshold Neutrino-Nucleus Coherent Scattering, *Phys. Rev.* D 93, 013015, 2016, doi: 10.1103/PhysRevD.93.013015.

[2] M. Bowen and P. Huber, Reactor Neutrino Applications and Coherent Elastic Neutrino Nucleus Scattering, *Phys. Rev.* D 102, 053008, 2020, doi: 10.1103/PhysRevD.102.053008.

[3] W. Rau, SuperCDMS SNOLAB - Status and Plans, *J. Phys.: Conf. Ser.* 1342, 012077, 2020, doi: 10.1088/1742-6596/1342/1/012077.

[4] Y. Kim, Detection of antineutrinos for reactor monitoring, *Nuclear Engineering and Technology* 48, 285-292, 2016, doi: 10.1016/j.net.2016.02.001.

[5] A. Bernstein, N. Bowden, and A. S. Ericson, Reactors as a source of antineutrinos: the effect of fuel loading and burnup for mixed oxide fuels, *Phys. Rev.* A 9, 014003, 2018, doi: 10.1103/PhysRevApplied.9.014003.

[6] W. E. Ang, S. Prasad, and R. Mahapatra, Reactor antineutrino response using low threshold coherent elastic neutrino-nucleus scatter-based detectors, IEEE Nuclear Science Symposium and Medical Imaging Conference (2020).

[7] M. Rupak, Dark Matter, Neutrino and Axion Search. [Online]. Available: http://people.tamu.edu/mahapatra/miner.html.

[8] S. Golwala, SuperCDMS and GEODM, Workshop on Ge-based detectors and technologies, 2020. [Online]. Available:https://indico.cern.ch/event/943069/contributions/4104016/attachments/2146542/3618235/SuperCDMSGolwalaReynolds.pdf.

[9] A. C. Hayes and P. Vogel, Reactor Neutrino Spectra, *Annual Review of Nuclear and Particle Science* 66, 219, 2016, doi: 10.1146/annurev-nucl-102115-044826.

[10] JEFF-3.3. [Online]. Available: https://www.oecd-nea.org/dbdata/jeff/jeff33/index.html.

[11] ENDF/B-VIII.0 Evaluated Nuclear Data Library. [Online]. Available: https://www.nndc.bnl.gov/endf/b8.0/.

[12] V. I. Kopeikin, Flux and Spectrum of Reactor Antineutrinos, *Phys. Atom. Nuclei* 75, 143, 2012, doi: 10.1134/S1063778812020123.

[13] S. Ishimoto, T. Omori, H. Arima, and K. Ishibashi, Simple Calculation of Reactor Antineutrino Energy Spectrum by the Use of Nuclear Data Libraries, *Journal of Nuclear Science and Technology* 39, 670, 2002, doi: 10.1080/18811248.2002.9715248.

[14] P. Venkataramaiah, A simple relation for the Fermi function, *J. Phys. G: Nucl. Phys.* 11, pp. 359-364, 1985, doi: 10.1088/0305-4616/11/3/014.

[15] J. Erler and S. Su, The Weak Neutral Current, *Progress in Particle and Nuclear Physics* 71, 119, 2013, doi: 10.1016/j.ppnp.2013.03.004.

[16] P. Coloma, I. Esteban, M. C. Gonzalez-Garcia, and J. Menendez, Determining the Nuclear Neutron Distribution from Coherent Elastic Neutrino-Nucleus Scattering:

Current Results and Future Prospects, *J. High Energ. Phys.* 2020, 30, 2020, doi: 10.1007/JHEP08(2020)030.

[17] JAEA Nuclear Data Center, Table of Nuclear Data. [Online]. Available: https://wwwndc.jaea.go.jp/NuC/.

[18] A. Oralbaev, M. Skorokhvatov, and O. Titov, The Inverse Beta Decay: A Study of Cross Section, *J. Phys.: Conf. Ser.* 675, 012003, 2016, doi: 10.1088/1742-6596/675/1/012003.

[19] P. Mumm, PROSPECT (Precision reactor oscillation and spectrum experiment), 2017. [Online]. Available: https://prospect.yale.edu/sites/default/files/files /DNP17_overview_final.pdf.

[20] G. Agnolet et al., Background studies for the MINER coherent neutrino scattering reactor experiment, *Nucl. Instrum. Methods Phys. Res.* A 853, pp. 53-60, 2017, doi: 10.1016/j.nima.2017.02.024.

[21] R. Agnese, projected sensitivity of the SuperCDMS SNOLAB experiment, *Phys. Rev.* D 95, 082002, 2017, doi: 10.1103/PhysRevD.95.082002.

4. ANTINEUTRINO DETECTION FOR TEMPORAL MONITORING OF FUEL BURNUP IN A LARGE NUCLEAR REACTOR*

4.1. Introduction

Nuclear safeguards using antineutrino detection have been long proposed since the 1980s and various feasibility studies have been conducted [1] [2]. The conventional way to detect antineutrinos from a reactor core is based on the inverse beta decay (IBD) reaction:

$$\bar{\nu}_e + p \rightarrow e^+ + n \tag{4-1}$$

Traditional IBD antineutrino detectors utilize this reaction, where an antineutrino interacts with a proton to produce a positron and a neutron. However, the IBD reaction has an intrinsic energy threshold of 1.806 MeV and low cross-sections (~10^{-42} cm^2) due to the infinitesimal mass of antineutrinos [3]. Thus, IBD detectors are usually large in size [4] [5].

The observation of the coherent-elastic-neutrino-nucleus-scattering (CEνNS) reaction in 2017 offered an alternate solution to improve antineutrino detection efficiency because of its higher cross-section compared to IBD [6]. Better intrinsic efficiencies will allow use of smaller detectors.

---

*Reprinted with permission from “Antineutrino detection for temporal monitoring of semiconductor detectors of fuel burnup in a large nuclear reactor antineutrinos,” by W. E. Ang, S. Prasad, and S. S. Chirayath April 2022. *Nuclear Instruments and Methods in Physics Research Section A: Accelerators, Spectrometers, Detectors and Associated Equipment*, Vol. 1028, p. 166353 with minor updates.

Various case studies on using antineutrinos as a means to safeguards monitoring of nuclear reactors have been performed in the past few years. However, most of these studies have been based on using the IBD reaction [1] [2] [7]. As yet, the reactor antineutrinos have not been measured using CEνNS. Our objective is to investigate if antineutrino monitoring can be performed using a relatively small-size CEνNS based detector. We investigate if small size CEνNS based detectors can be used to monitor the burnup of the fuel from outside the reactor containment.

4.2. Methodology

In our study, we used the '*ab initio*' summation method to model the AP1000 reactor antineutrino spectrum [8]. Antineutrinos are mainly produced from the beta minus decay of fission product isotopes. First, we identified all beta minus decay fission products from ^{235}U, ^{238}U, ^{239}Pu, and ^{241}Pu, which cause over 99% of fission reactions. Next, we modeled and summed the antineutrino spectrum from all beta minus decay isotopes from ^{235}U, ^{238}U, ^{239}Pu, and ^{241}Pu, to produce the antineutrino spectrum.

Once we obtained the ^{235}U, ^{238}U, ^{239}Pu, and ^{241}Pu antineutrino spectra, we simulated the AP1000 core using MCNP 6.2 to determine the fission fraction of fissile isotopes at various burnup steps from 0 to 60 GWd/MTU. This allowed us to model the AP1000 reactor antineutrino spectrum based on different operation duration and burnups [9].

Lastly, we computed the pulse height distributions from the reactor antineutrino spectrum and demonstrated various comparison cases to see if the conceptual CEνNS based detector can be applied for reactor monitoring, while satisfying International Atomic Energy Agency’s (IAEA) requirement.

4.2.1. Antineutrino spectrum calculation

An antineutrino spectrum of the fissionable isotopes can be defined as below [8]:

$$\frac{dN}{dE_v} = \sum_n Y_n(Z, A, t) \sum_i b_{n,i}(E_0^i) P_v(E_v, E_0^i, Z) \tag{4-2}$$

where $Y_n(Z, A, t)$ is the number of β decays of fission fragment Z and A at time t. The Y_n is approximately cumulative yield and is independent of t after a reactor is burned for sufficient time. The beta intensity, $b_{n,i}$, refers to the probability of beta decay to a given excited state with its endpoint-energy and sums up to unity when the fission fragment does not have additional decay modes other than beta minus decay. Lastly, P_v is the normalized antineutrino spectrum with endpoint energy, E_0^i. We obtained endpoint energies and beta intensities values from ENDF/VIII.0 and cumulative yield from JEFF-3.3 nuclear libraries [10] [11]. The antineutrino emission spectrum for a fission fragment can be defined as [8]:

$$P_v\left(E_v, E_0^i, Z\right) = k p_e (E_0 - E_e)^2 F(Z, E_e) C(Z, E_e)[1 + \delta(Z, A, E_e)] \tag{4-3}$$

where k is the normalization constant, p_e is electron momentum, $F(Z, E_v)$ is the Fermi function, Z is the atomic number, E_v is the initial antineutrino energy incident on the detector, E_e is the total electron energy, m_0 is electron rest mass and $C(Z, E_e)$ is shape factor. For allowed decay, $C(Z, E_e)$ is equal to 1. This study assumes all the beta decays are allowed decay. The endpoint energy, E_0 is approximately equal to $Q + m_0c^2$, where Q is the Q-value. The function $\delta(Z, A, E_e)$ includes corrections that should be considered to the shape of the spectrum, which are finite-size correction, radiative correction, and weak magnetism correction [8] [12] [13]. To obtain the antineutrino spectrum, Eq. 4-3 must substitute $E_v = E_0 - E_e$.

4.2.2. AP1000 reactor modeling

AP1000 reactor is a 3,400 MW(t) commercial pressurized water reactor designed by Westinghouse Electric Company [14]. The reactor core consists of 157 fuel assemblies, with each fuel assembly comprising of 264 fuel rods and 25 guide tubes for optional neutron control rods. To simplify and speed-up the Monte Carlo simulation, we took advantage of the symmetry of the reactor core and modeled a quarter of it with reflecting boundary conditions applied to the boundaries towards the core in MCNP 6.2, as in Fig.4-1 (Top). The fuel rods contained explicit helium bonded uranium fuel, and cladding regions in Fig. 4-1 (Bottom), and each assembly was modeled with 25 guide tubes. In this study, we simulated two cases using MCNP 6.2: 3.3-wt-% and 4.4-wt-% ^{235}U, with no boron in the pressurized coolant/moderator water. The fuel was burned from 0 to 60 GWd/MTU with the help of CINDER-90 module, which is part of MCNP 6.2 code.

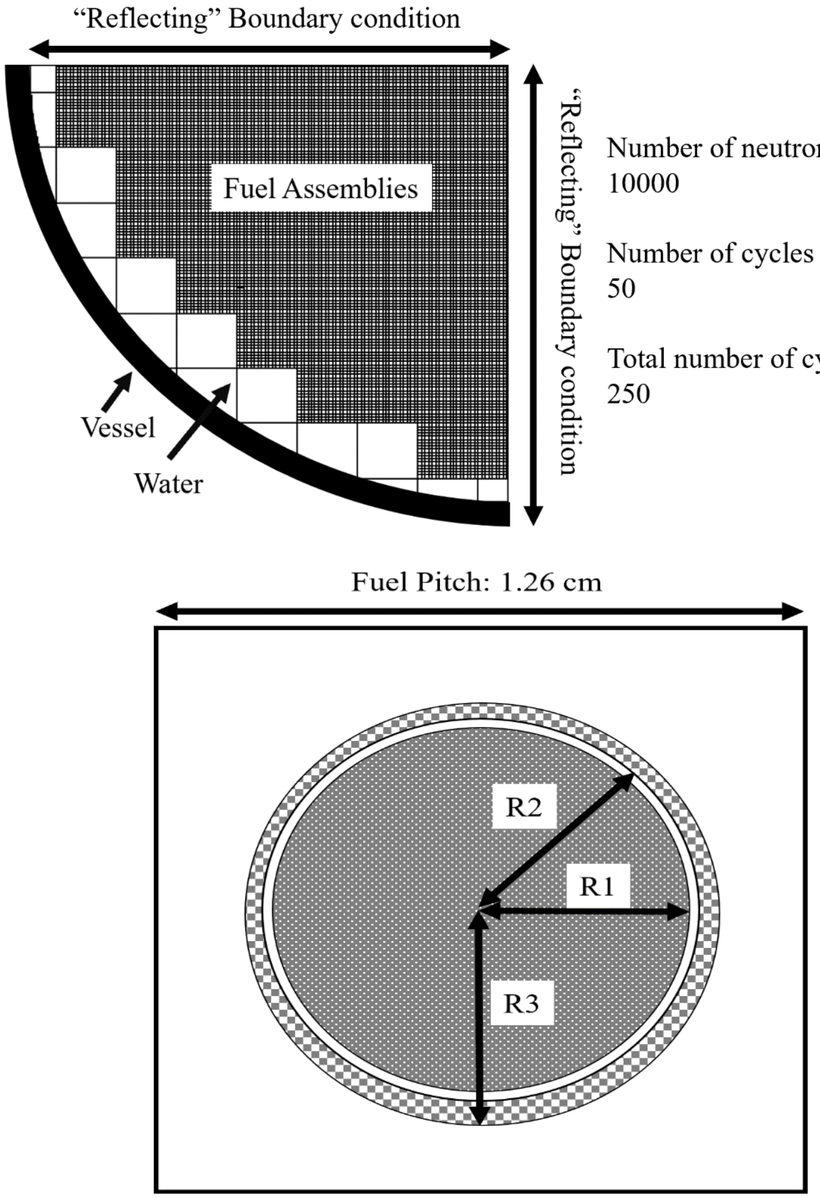

Number of neutrons per cycle:
10000

Number of cycles skipped:
50

Total number of cycles:
250

R1: Fuel Radius = 0.409575 cm
R2: Helium = 0.41775 cm
R3: Cladding = 0.47475 cm

Figure 4-1 (Top): AP1000 reactor quarter core with reflecting boundary conditions on both sides. (Bottom) AP1000 fuel pitch parameters.

4.2.3. CEvNS cross-section calculation

The differential equation of CEvNS cross-section is defined as [15]:

$$\frac{d\sigma(E_v)}{dT_R(E_v)} = \frac{G_F^2 M}{2\pi}[(q_v + q_A)^2 + (q_v - q_A)^2 \left(1 - \frac{T_R}{E_v}\right)^2 - (q_v^2 - q_A^2)\frac{MT_R}{E_v^2}] \qquad (4\text{-}4)$$

where G_F denotes the Fermi constant, M is the mass of the targeted nucleus, q_v and q_A are vector and axial charges respectively, T_R is recoil energy and E_v is incident antineutrino energy. We neglected the axial term q_A in the equation as it is small for most nuclei, and it is 0 for the spin-zero nuclei [16] [17] [18] [19]. The vector charges, q_v can be defined as:

$$q_v = g_v^p Z + g_v^n N \qquad (4\text{-}5)$$

where g_v^p and g_v^n are vector proton and neutron weak neutral current couplings respectively [20]. Variables Z and N represent the number of protons and neutrons in the nucleus respectively. The maximum recoil energy that can be produced by an incident antineutrino energy is [15]:

$$T_R^{Max} = \frac{2E_v^2}{M + 2E_v} \qquad (4\text{-}6)$$

In a previous study, we have calculated the CEvNS cross-section for both natural germanium and natural silicon and compared them to the IBD cross-section [6]. The results show that the CEvNS cross-sections for natural germanium and silicon are one to two magnitude higher than the IBD cross-section.

4.2.4. Detector response and pulse height distribution

The detector response rate as a function of incident antineutrino energy is defined as:

$$R(E_v) = N\sigma(E_v)\phi(E_v) \tag{4-7}$$

where N is the number of atoms, σ is the CEvNS cross-section and ϕ is the antineutrino flux. Next, we define the probability of the recoiled energies for a given incident antineutrino energy as below:

$$P(E_v \to T_R) = \frac{d\sigma(E_v, T_R)}{dT_R} / \sigma(E_v) \tag{4-8}$$

Using the results from Eq. 4-7 and Eq. 4-8, we obtain pulse height distribution, C as a function of T_R using the equation:

$$C(T_R) = \int_{E_v} R(E_v)P(E_v \to T_R)dE_v \tag{4-9}$$

For demonstration purposes, we assume a 100 kg CEνNS based natural germanium detector with a 100 eV nuclear recoil (NR) threshold, placed 25 m away from the core located outside of the reactor containment. A minimum detection limit of 100 eV_{NR} in germanium will allow measurement of antineutrinos above 1.84 MeV. Background levels of 100 differential rate units (DRU) are assumed due to the surrounding radiation interacting in the detector, which corresponds to 100 detected events/(keV.kg.day).

For calculating the probability of detecting a difference between two fuel burnups, we define:

$$Detection\,probability = 1 - \beta \tag{4-10}$$

where β is the error (probability) of omission or the type II error in hypothesis-testing, also known as non-detection probability. The IAEA requires detection probability to be greater than 20% for low likelihood events. Based on the IAEA's minimum detection probability requirements, we set the false alarm probability α, at 5% [2]. We applied a 3% spread to the detector count rate, which accounts for 1% uncertainty in operating power, 1% in detection and instrumentation, and another 1% due to uncertainty in counting statistics.

4.3. Results and discussion

In this section, we discuss the AP1000 reactor fission antineutrino production rates from MCNP 6.2. Both 3.3-wt-% ^{235}U and 4.4-wt-% ^{235}U reactor antineutrino spectra are presented with their antineutrino production rate, average mean energies, variance, skewness, and kurtosis. The calculated pulse height distributions from Eq. 4-9 are examined to understand the resolution needed to distinguish CEνNS response at various burnups.

4.3.1. AP1000 fission rate and fission fraction results

From the MCNP simulations, we obtain the fission rates for ^{235}U, ^{238}U, ^{239}Pu, and ^{241}Pu at a given enrichment and burnup. Tables 4-1 and 4-2 show the full core fission rates for all the fissionable isotopes, the total fission rate for AP1000, k_{eff} values and ^{238}U neutron capture events for both 3.3-wt-% ^{235}U and 4.4-wt-% ^{235}U cases as function of burnup steps.

Table 4-1 AP1000 full-core fission rate for ^{235}U, ^{238}U, ^{239}Pu, and ^{241}Pu, ^{238}U neutron capture rate, and k_{eff} values for 3.3-wt-% ^{235}U at various burnup steps.

Burnup (GWd/MTU)	k_{eff}	Fission rate (s^{-1})				^{238}U neutron capture rate (s^{-1})
		^{235}U	^{238}U	^{239}Pu	^{241}Pu	
0	1.3353	9.97E+19	5.88E+18	7.18E-16	7.63E-16	5.31E+19
10	1.1676	7.22E+19	6.97E+18	2.38E+19	1.33E+18	6.05E+19
20	1.0806	5.52E+19	7.68E+18	3.61E+19	4.57E+18	6.65E+19
40	0.9234	2.55E+19	9.21E+18	5.34E+19	1.39E+19	8.09E+19
60	0.8326	9.28E+18	1.02E+19	6.16E+19	2.01E+19	9.08E+19

Table 4-2 AP1000 full-core fission rate for ^{235}U, ^{238}U, ^{239}Pu, and ^{241}Pu, ^{238}U neutron capture rate, and k_{eff} values for 4.4-wt-% ^{235}U at various burnup steps.

Burnup (GWd/MTU)	k_{eff}	Fission rate (per s^{-1})				^{238}U neutron capture rate (per s^{-1})
		^{235}U	^{238}U	^{239}Pu	^{241}Pu	
0	1.3859	1.00E+20	5.59E+18	5.67E-16	5.89E-16	4.70E+19
10	1.2294	7.94E+19	6.49E+18	1.79E+19	7.72E+17	5.30E+19
20	1.1493	6.58E+19	7.03E+18	2.82E+19	2.88E+18	5.76E+19
40	0.9947	3.96E+19	8.32E+18	4.47E+19	1.02E+19	6.96E+19
60	0.8792	1.99E+19	9.51E+18	5.52E+19	1.70E+19	8.15E+19

We converted the fission rates in Tables 4-1 and 4-2 into the fission fractions in Tables 4-3 and 4-4. These fractions provide the probability of a particular fissionable isotope causing a fission, given that a fission reaction occurred. Tables 4-3 and 4-4 also show the ^{238}U neutron capture, given that burnup and duration that the reactor operated for. At 40 GWd/MTU, both 3.3-wt-% ^{235}U and 4.4-wt-% ^{235}U cases drop to subcriticality with the k_{eff} values dropping below 0.9234 and 0.9947, respectively. It is clear that as burnup increases, the likelihood of fission moves away from ^{235}U to mainly ^{239}Pu as the first isotope depletes and the second isotope builds-up with operation-time. ^{241}Pu and ^{238}U also begin to contribute notably. It is remarkable to see the ^{238}U capture rates nearly double from 0 GWd/MTU to 60 GWd/MTU, however, the antineutrino energies from these captures fall much below the 1.84 MeV threshold of detection due to 100 eV_{NR} limit.

Table 4-3 Fission fraction of important fissionable isotopes with 3.3-wt-% ^{235}U at various burnup steps.

Burnup (GWd/MTU)	Time (days)	Fission Fraction				
		^{235}U	^{238}U	^{239}Pu	^{241}Pu	^{238}U neutron capture
0	0	0.9443	0.0557	0.0000	0.0000	0.5030
10	270	0.6926	0.0669	0.2278	0.0127	0.5804
20	510	0.5334	0.0741	0.3483	0.0441	0.6423
40	1070	0.2502	0.0902	0.5236	0.1360	0.7923
60	1590	0.0917	0.1011	0.6089	0.1983	0.8979

Table 4-4 Fission fractions of important fissionable isotopes with 4.4-wt-% ^{235}U at various burnup steps.

Burnup (GWd/MTU)	Time (days)	Fission Fraction				
		^{235}U	^{238}U	^{239}Pu	^{241}Pu	^{238}U neutron capture
0	0	0.9471	0.0529	0.0000	0.0000	0.4450
10	270	0.7592	0.0620	0.1714	0.0074	0.5068
20	510	0.6331	0.0676	0.2715	0.0277	0.5542
40	1070	0.3850	0.0810	0.4351	0.0989	0.6769
60	1590	0.1957	0.0935	0.5436	0.1671	0.8015

Nonetheless, the buildup of ^{239}Pu results from the neutron capture of ^{238}U, where ^{239}Pu undergoes beta decay to ^{239}Np, and subsequently ^{239}Pu. During this breeding process, two antineutrinos are produced through two beta decays of ^{239}U. Thus, the ^{238}U capture event should be taken into consideration when determining the antineutrino production of the reactor. The ^{238}U neutron capture rate increases with burnup.

4.3.2. AP1000 antineutrino spectrum

Using the tabulated fission fraction values in Tables 4-3 and 4-4, we modelled the reactor antineutrino spectrum using Eq. 4-2. Figs. 4-2 and 4-3 show the AP1000 reactor antineutrino spectrum for both 3.3-wt-% ^{235}U and 4.4-wt-% ^{235}U, at burnup steps of 10 and 60 GWd/MTU. It can be seen that the antineutrino spectra are heavily skewed towards lower antineutrino energies as shown in Tables 4-5 and 4-6. The peak seen in the spectrum close to antineutrino energy of 0.5 MeV is due to the antineutrinos produced from the ^{238}U neutron capture events.

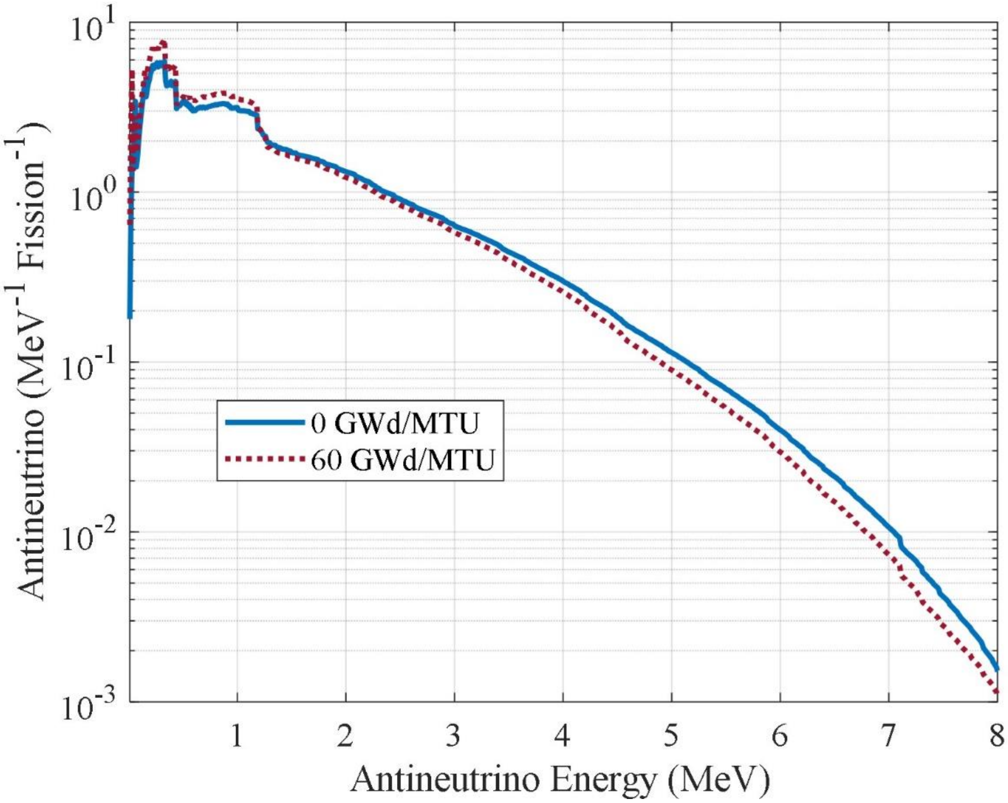

Figure 4-2 AP1000 reactor antineutrino spectrum for 3.3-wt-% ^{235}U, with burnup 0 and 60 GWd/MTU comparison.

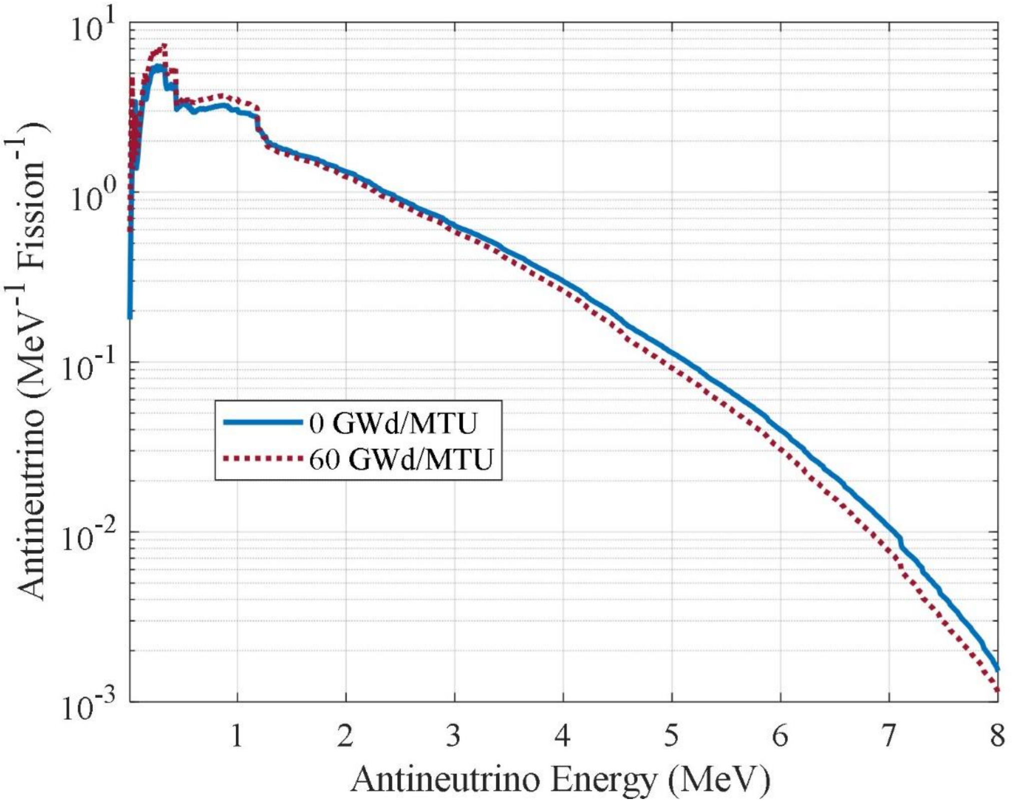

Figure 4-3 AP1000 reactor antineutrino spectrum for 4.4-wt-% ^{235}U, with burnup 10 and 60 GWd/MTU.

Using Figs. 4-2 and 4-3, we calculated antineutrino production rate, average antineutrino energies, variance, skewness, and kurtosis at burnup steps of 0, 10, 20, 40 GWd/MTU, and 60 GWd/MTU and is shown in Tables 4-5 and 4-6 for 3.3% and 4.4% ^{235}U enrichments, respectively.

Table 4-5 The antineutrino production rate, mean, variance, skewness, and kurtosis for 3.3-wt-% ^{235}U antineutrino spectrum.

Burnup (GWd/MTU)	Antineutrino production (per fission)	Mean Energy (MeV)	Variance (MeV)	Skewness	Kurtosis
0	7.1485	1.3645	1.4047	2.4214	10.3960
10	7.1866	1.3232	1.3534	2.3512	9.9474
20	7.2539	1.2972	1.3210	2.3057	9.6616
40	7.4878	1.2496	1.2627	2.2264	9.1640
60	7.6731	1.2221	1.2291	2.1816	8.8865

Table 4-6 The antineutrino production rate, mean, variance, skewness, and kurtosis for 4.4-wt-% ^{235}U antineutrino spectrum.

Burnup (GWd/MTU)	Antineutrino production (per fission)	Mean Energy (MeV)	Variance (MeV)	Skewness	Kurtosis
0	7.0295	1.3776	1.4138	2.4154	10.4111
10	7.0656	1.3452	1.3753	2.3662	10.0837
20	7.1119	1.3239	1.3496	2.3318	9.8605
40	7.2913	1.2810	1.2983	2.2656	9.4298
60	7.5034	1.2460	1.2573	2.2142	9.0972

In Tables 4-5 and 4-6, the antineutrino spectrum extending to 14 MeV was used for calculating the central moments to study the difference in the shapes of the spectrum with increasing burnup. The antineutrino production is seen increasing when the burnup increases. During the operation, the inventory of ^{235}U decreases due to its consumption in the fission process and it typically produces about 6.08 antineutrinos per fission. However, ^{239}Pu and ^{241}Pu inventories in the core begin increasing and produce about 5.51 and 6.26

antineutrinos per fission, respectively.

In Tables 4-5 and 4-6, we also observe that the mean antineutrino energy decreases with increasing burnup. The reduction in the mean antineutrino energy is the result of depletion of ^{235}U with a higher average antineutrino energy and the buildup of ^{239}Pu with a lower antineutrino energy as shown in Table 4-7. Increased fuel burnup also leads to greater contributions from ^{241}Pu and ^{238}U fissions, which in fact have higher average antineutrino energies; however, these fissions rates are much smaller compared to ^{239}Pu. Detailed shape comparison of the four fissionable isotopes illustrating a softer antineutrino spectrum of ^{239}Pu compared to ^{235}U has been shown in a previous work [21]. Fig. 4-4 shows the antineutrino spectrum of each fissionable isotopes.

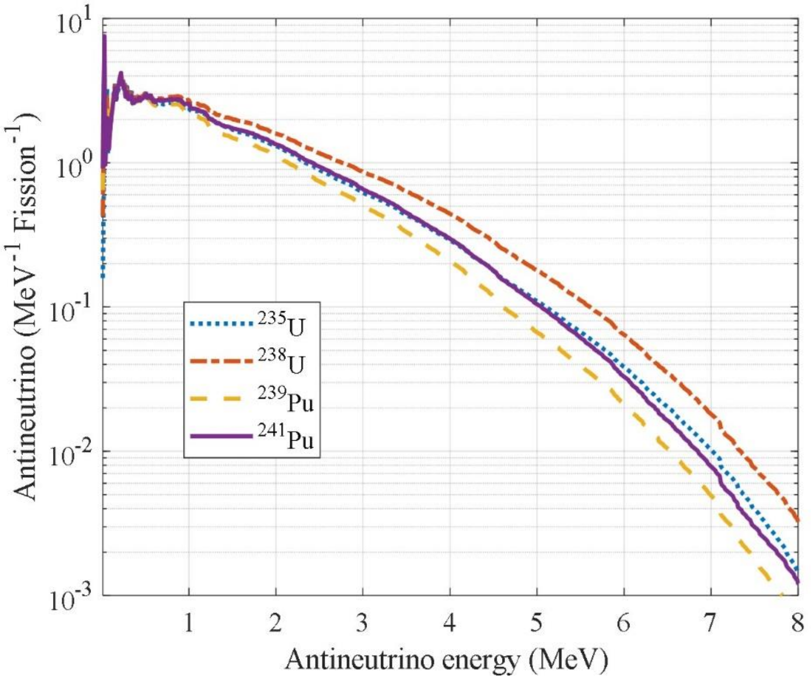

Figure 4-4 Antineutrino spectrum of ^{235}U, ^{238}U, ^{239}Pu, and ^{241}Pu. ^{238}U has the hardest antineutrino spectrum while ^{239}Pu has the softest antineutrino spectrum among the four fissionable isotopes.

Table 4-7 The antineutrino production for each fissionable isotope with its average antineutrino energies.

Fissionable Isotopes	E_ν (MeV)	N_ν (per fission)
^{235}U	1.49	6.08
^{238}U	1.65	7.17
^{239}Pu	1.36	5.51
^{241}Pu	1.48	6.26
^{238}U to ^{239}Pu	0.54	2.00

Figs. 4-2 and 4-3 illustrates that as the burnup increases, the spectrum shifts to lower energies from the tail region, indicating an even greater left-skewing distribution with a reduced importance of the tail. Thus, Tables 4-5 and 4-6 for 3.3-wt-% ^{235}U and 4.4-wt-% ^{235}U, respectively, show a trend of decreasing skewness and kurtosis with the burnups. The decreasing skewness entails a shift towards the lower energies and closer to the mean, the decreasing kurtosis indicates that the tails of spectra become less significant when the burnup increases.

4.3.3. Pulse height distribution and background

Our study assumes a 100 kg CEνNS based germanium detector placed 25 m away from the AP1000 reactor core. The detector is subjected to an instrumentation threshold of 100 eV$_{NR}$ and a background level of 100 DRU. Figs. 4-5 and 4-6 show the pulse height distribution for 0, 20, and 60 GWd/MTU, with the 100 eV$_{NR}$ threshold and 100 DRU antineutrino background cuts superimposed.

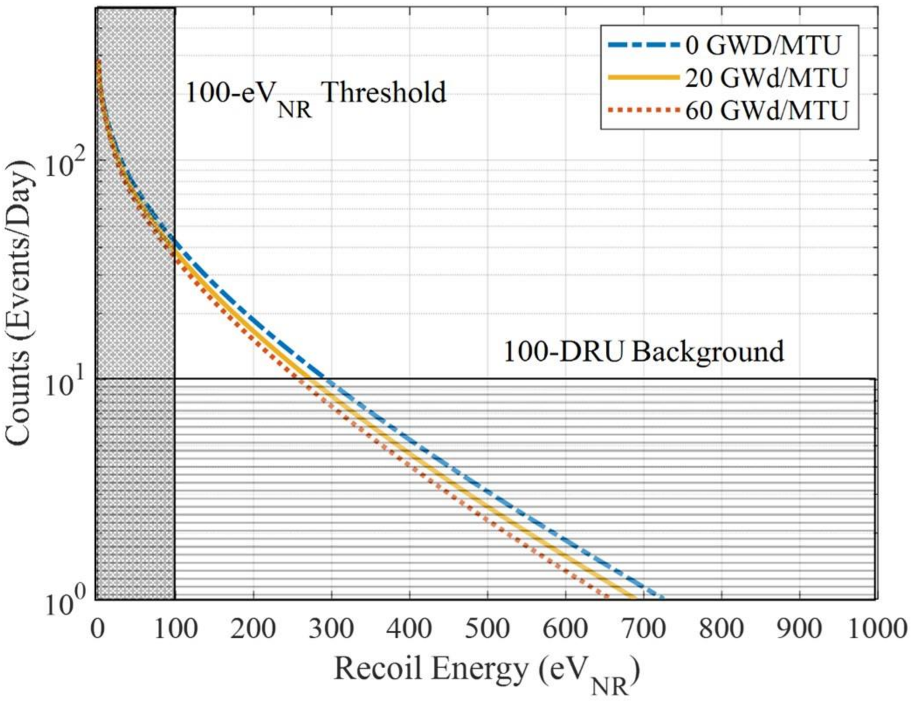

Figure 4-5 Pulse height distribution as a function of recoil energy with 1 eV resolution for 3.3-wt-% ^{235}U, with 100 DRU antineutrino background and 100 eV$_{NR}$ threshold.

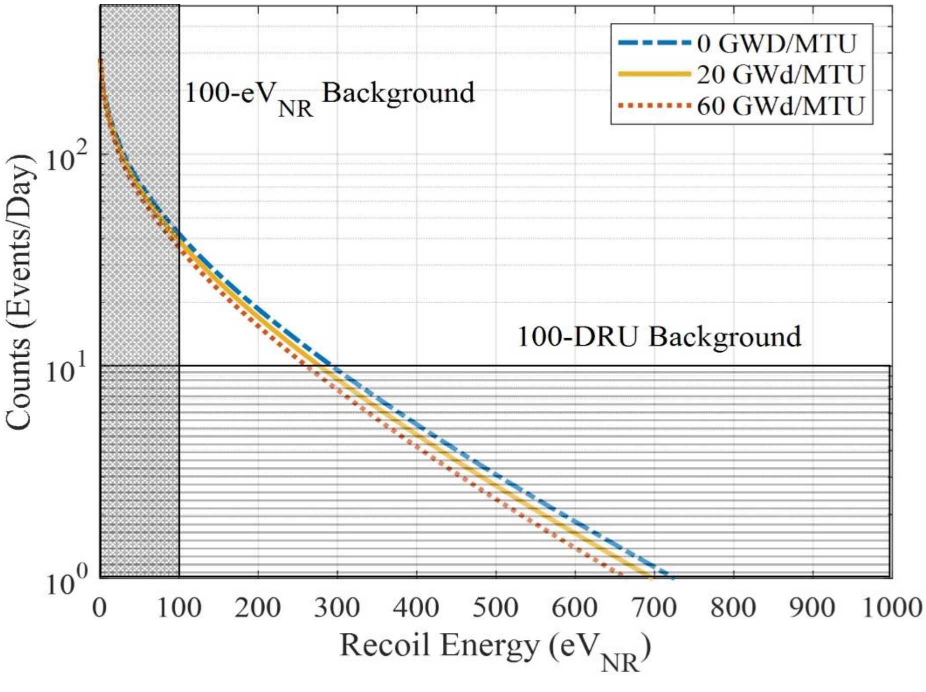

Figure 4-6 Pulse height distribution as a function of recoil energy with 1 eV resolution for 4.4-wt-% ^{235}U, with 100 DRU antineutrino background and 100 eV$_{NR}$ threshold.

In this section, we present detector response in the form of pulse height distributions for both 3.3-wt-% ^{235}U and 4.4-wt-% ^{235}U cases. Tables 4-8 and 4-9 show the total gross counts, net count rate after 100 DRU background subtraction, and net count rate after 100 DRU background and 100 eV$_{NR}$ threshold subtraction, for burnup steps 10, 20, 40, and 60 GWd/MTU, respectively.

Table 4-8 The total gross counts, the net counts after 100 DRU background subtraction, and the nets with both 100 DRU background and 100 eV$_{NR}$ threshold subtraction for 3.3-wt-% ^{235}U case.

Burnup (GWd/MTU)	Total Gross Counts (Events/Day)	100 DRU Background Subtraction (Events/Day)	100 eV$_{NR}$ Threshold (Events/Day)
0	14933.33	10190.33	2158.28
10	14090.49	9525.28	1883.72
20	13662.75	9189.83	1745.79
40	13069.15	8746.39	1553.59
60	12798.56	8551.30	1464.87

Table 4-9 The total gross counts, the net counts after 100 DRU background subtraction, and the nets with both 100 DRU background and 100 eV$_{NR}$ threshold subtraction for 4.4-wt-% ^{235}U case.

Burnup (GWd/MTU)	Total Gross Counts (Events/Day)	100 DRU Background Subtraction (Events/Day)	100 eV$_{NR}$ Threshold (Events/Day)
0	14888.60	10148.71	2153.09
10	14258.50	9647.01	1946.31
20	13893.75	9362.20	1828.09
40	13337.94	8942.13	1646.34
60	12974.53	8674.51	1527.13

Overall, the net total counts between 3.3-wt-% ^{235}U and 4.4-wt-% ^{235}U cases have a similar trend where the counts decrease when the burnup increase. For the 3.3%-enrichment case, the difference between the gross count rate and net count rate after 100 DRU background subtraction are: 31.76%, 32.43%, 32.74%, 33.08% and 33.19% for 0, 10, 20, 40, and 60 GWd/MTU. For the 4.4%-enrichment case, the difference between the gross count rate and net count rate after 100 DRU background subtraction are: 31.84%, 32.34%, 32.62%, 32.96% and 33.14% for 0, 10, 20, 40, and 60 GWd/MTU.

When in addition, with the 100 eV$_{NR}$ threshold applied, the count rate difference between the gross counts and the final net counts becomes even larger. For the 3.3%-enrichment case, the difference between the gross count rate and the final net count rate are: 78.82%, 80.21%, 81.00%, 82.24% and 82.87% for 0, 10, 20, 40, and 60 GWd/MTU. For the 4.4%-enrichment case, the difference between the gross count rate and the final net count rate are: 78.78%, 79.82%, 80.47%, 81.59% and 82.40% for 0, 10, 20, 40, and 60 GWd/MTU. The main reason for the sharp drop in the count rate was due to the high detector efficiency between 1 to 100 eV$_{NR}$, which is not utilized with a 100 eV$_{NR}$ threshold. Fig. 4-7 and Fig. 4-8 show the pulse height distributions as a function of recoil energy after the 100 DRU background and 100 eV$_{NR}$ threshold subtraction.

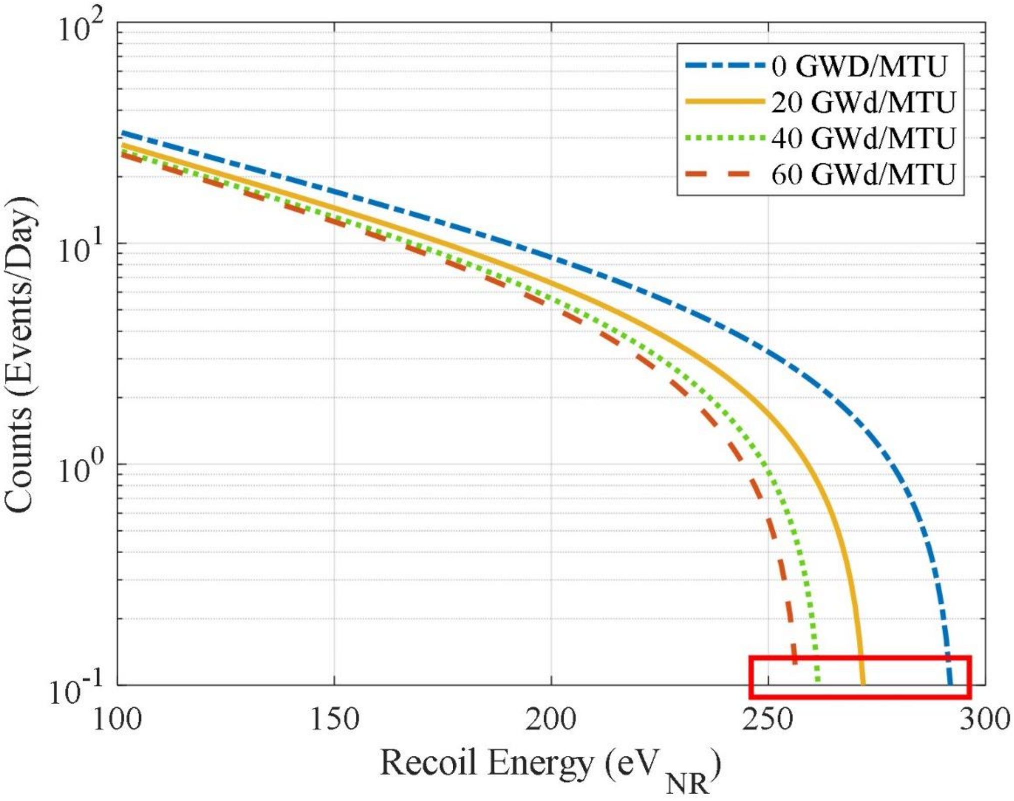

Figure 4-7 Pulse height distribution as a function of recoil energy with 1 eV resolution for 3.3-wt-% ^{235}U after 100 DRU background and 100 eV_{NR} threshold subtraction for burnups 10, 20, 40 and 60 GWd/MTU.

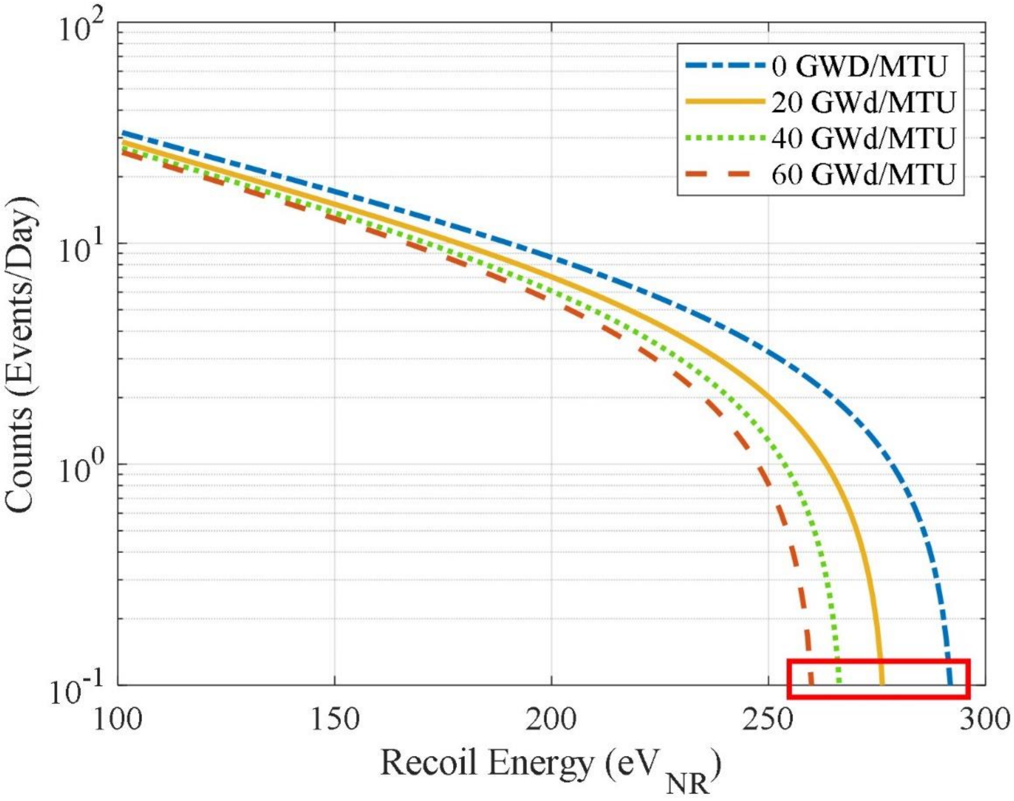

Figure 4-8 Pulse height distribution as a function of recoil energy with 1 eV resolution for 4.4-wt-% ^{235}U after 100 DRU background and 100 eV_{NR} threshold subtraction for burnup 10, 20, 40, and 60 GWd/MTU.

Figs. 4-7 and 4-8 provide the pulse height distributions after background and threshold reduction. It can be seen that the end-point energy or the highest detectable nuclear recoil energy of these distributions moves to lower nuclear recoil energies for higher burnups, as shown in Figs. 4-9 and 4-10. The box in Figs. 4-7 shows the end-point nuclear recoil energies for 0, 20, 40, and 60 GWd/MTU are 293 eV, 273 eV, 262 eV, and 257 eV, respectively. The difference between the end-point energies at 0 and 20 GWd/MTU is 20 eV, and that between more separated 40 and 60 GWd/MTU is only 5 eV. Similarly, in Fig. 4-8, the box indicates that the highest detectable nuclear energies at

0, 20, 40, and 60 GWd/MTU are 293 eV, 277 eV, 268 eV, 261 eV, respectively. The difference in end-point energies between 0 and 20 GWd/MTU is 16 eV, however, a much larger difference in burnup between 40 and 60 GWd/MTU also causes a similar shift in the end-point energy of 7 eV. Thus, the change in the end-point energies due to a given change in burnup is not constant but depends on the burnup. The ability to differentiate burnup based on end-point-energies is easier at lower burnups and becomes more difficult at higher burnups. So while a 20 eV_{NR} resolution might be sufficient when differentiating pulse height detector response between 0 and 20 GWD/MTU, it will not be sufficient for distinguishing the response between 20 and 40 GWD/MTU. Thus, CEνNS detectors interrogating beyond fresh fuel and detecting once or twice burned fuel in the core will require detector resolutions better than 16 eV_{NR} for end-point-analysis using pulse height distributions as demonstrated in Figs. 4-9 and 4-10. We acknowledge that CEνNS semiconductor resolution can vary from a few eVs to several tens of eVs, depending on the size and material of the detector.

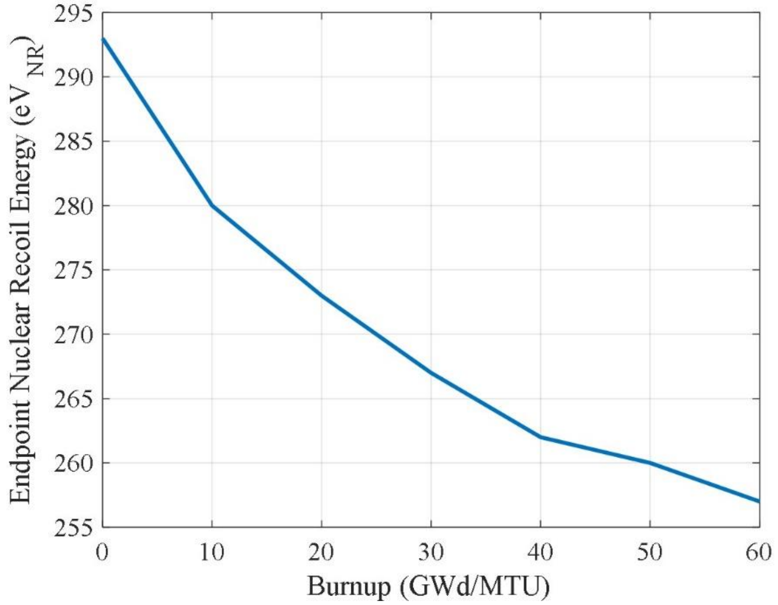

Figure 4-9 Pulse height endpoint nuclear recoil energies as a function of burnup for 3.3% ^{235}U enrichment.

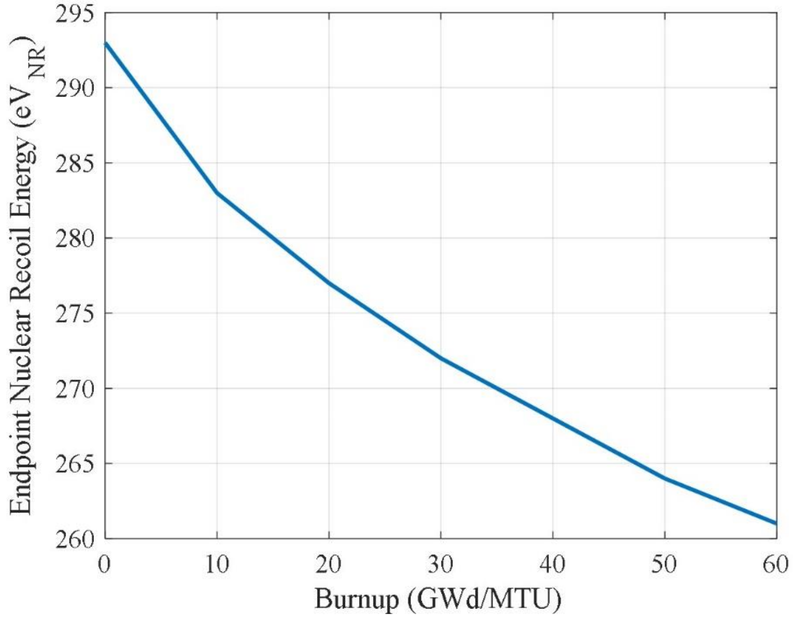

Figure 4-10 Pulse height endpoint nuclear recoil energies as a function of burnup for 4.4% ^{235}U enrichment.

4.3.4. Non-detection probability and burnup

The IAEA requires a minimum of 20% detection probability for low probability events. False alarm probability α, has been set at 0.05 to minimize the number of anomalies to be investigated. In this section, we deliberate whether higher burnups of the core can be adequately detected based on the integral net counts, if 10 GWd/MTU is treated as reference burnup and assuming a 3% spread in their normal distributions. We compare detection distributions of burnup at 10 to 20 GWd/MTU, 40 GWd/MTU, and 60 GWd/MTU for both 3.3-wt-% ^{235}U and 4.4-wt-% ^{235}U cases to determine if a CEνNS germanium detector with predetermined parameters satisfies the IAEA requirements, as shown in Figs. 4-11 and 4-12.

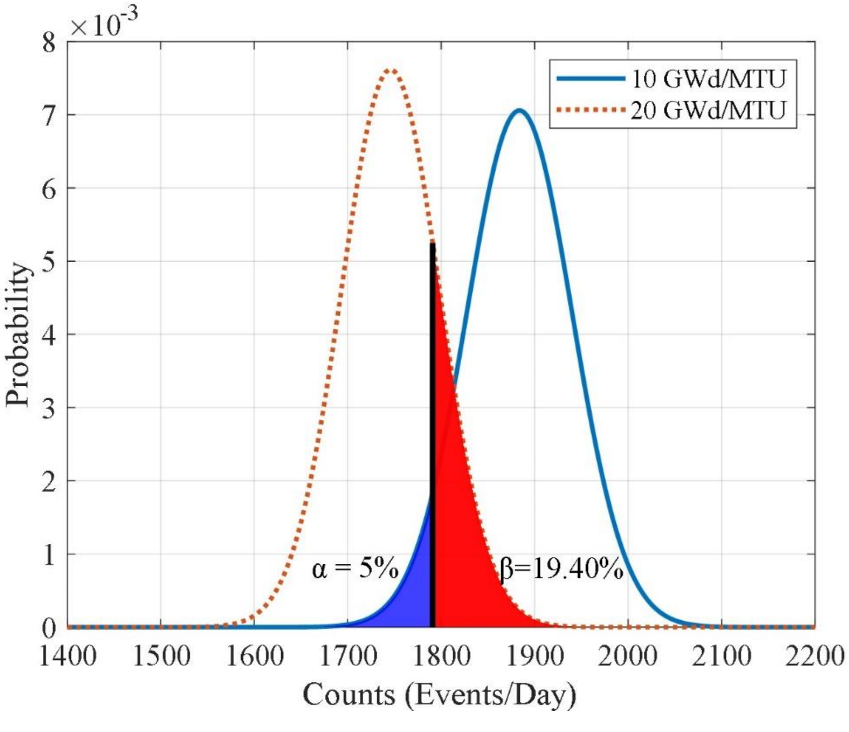

Figure 4-11 The normal distribution of 10 and 20 GWd/MTU counts with 3% uncertainty for 3.3-wt-% ^{235}U case. The non-detection probability, **β** is found at 19.40% when the false alarm probability, **α** is set at 5%.

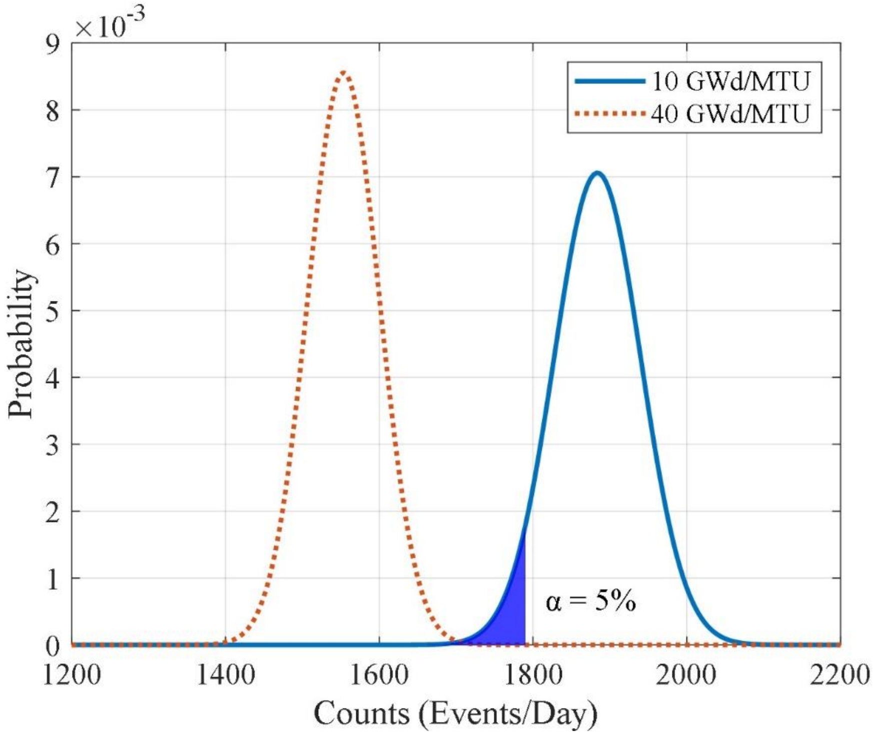

Figure 4-12 The normal distribution of 10 and 40 GWd/MTU counts with 3% uncertainty for 3.3-wt-% ^{235}U case. The non-detection probability, **β** is found at 0% when the false alarm probability, **α** is set at 5%.

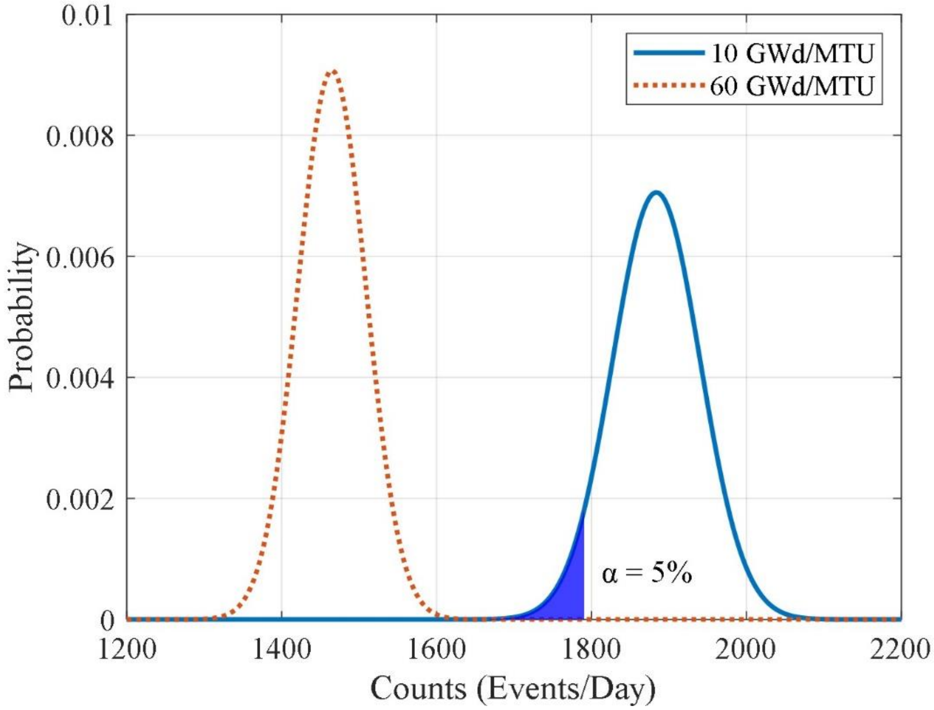

Figure 4-13 The normal distribution of 10 and 60 GWd/MTU counts with 3% uncertainty for 3.3-wt-% ^{235}U case. The non-detection probability, **β** is found at 0% when the false alarm probability, **α** is set at 5%.

Table 4-10 The non-detection probability and detection probability for 3.3-wt-% ^{235}U case.

Burnup (GWd/MTU)	Net Counts (Events/Day)	3% uncertainty	Non-detection Probability (%)	Detection Probability (%)
10	1883.72	56.51	N/A	N/A
10 and 20	1745.79	52.37	19.40	80.60
10 and 40	1553.59	46.61	0.00	100.00
10 and 60	1464.87	43.95	0.00	100.00

For 3.3-wt-% ^{235}U, the net count rate at 10 GWd/MTU is 1883.72 ± 56.51 events/day and for 20 GWd/MTU it is 1745.79 ± 52.37 events/day. The non-detection probability is calculated as 19.40% when the false alarm was set at 5%. Thus, there is a 80.60% probability that a safeguards measurement will detect the burnup difference. Comparing between burnups 10 and 40 GWd/MTU (net count rate: 1553.59 ± 46.61 events/day), the non-detection probability and detection probabilities are 0% and 100%. Lastly, distinguishing between burnup steps of 10 and 60 GWd/MTU (net count rate: 1464.87 ± 43.95 events/day), is measurable with nearly 100% confidence.

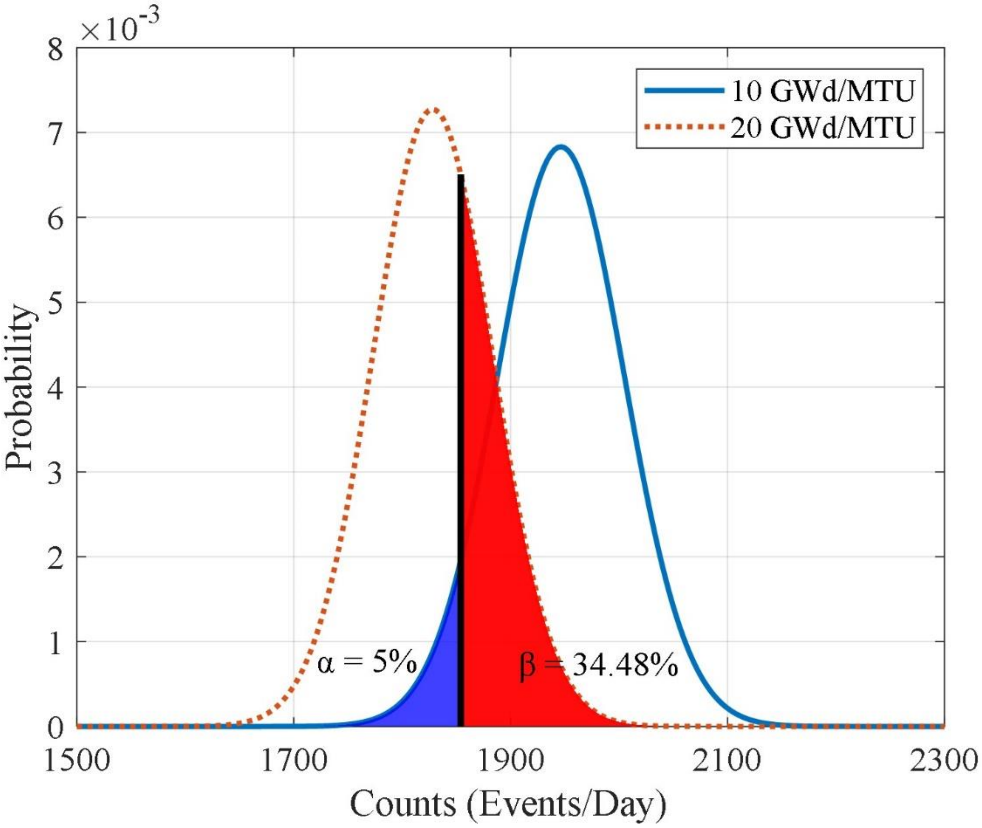

Figure 4-14 The normal distribution of 10 and 20 GWd/MTU counts with 3% uncertainty for 4.4-wt-% ^{235}U case. The non-detection probability, **β** is found at 34.48% when the false alarm probability, **α** is set at 5%.

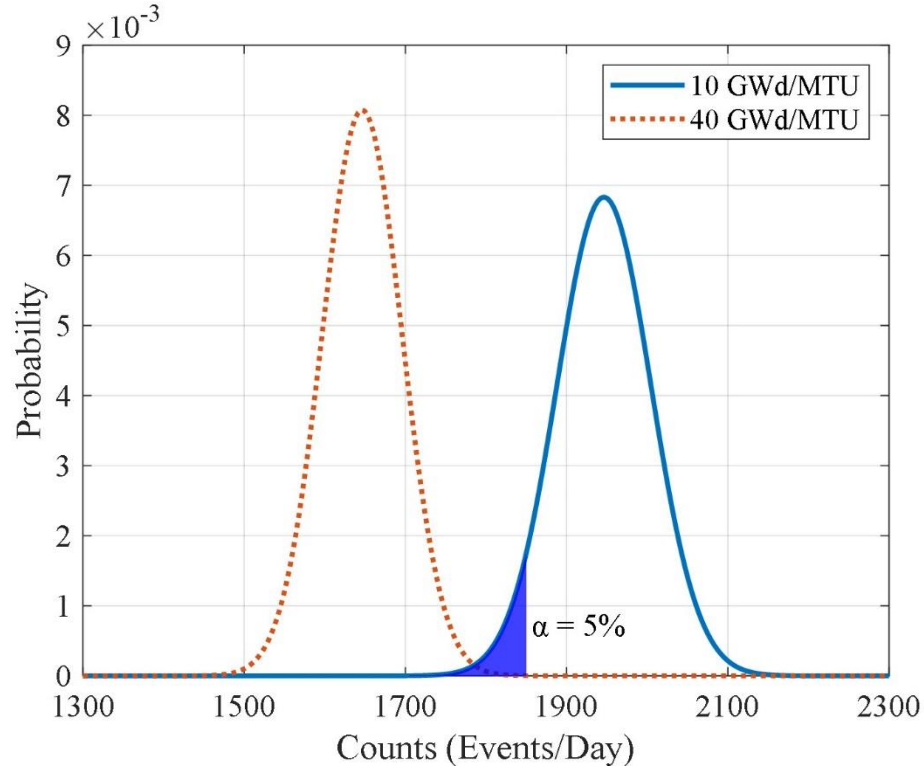

Figure 4-15 The normal distribution of 10 and 40 GWd/MTU counts with 3% uncertainty for 4.4-wt-% ^{235}U case. The non-detection probability, **β** is found at 0% when the false alarm probability, **α** is set at 5%.

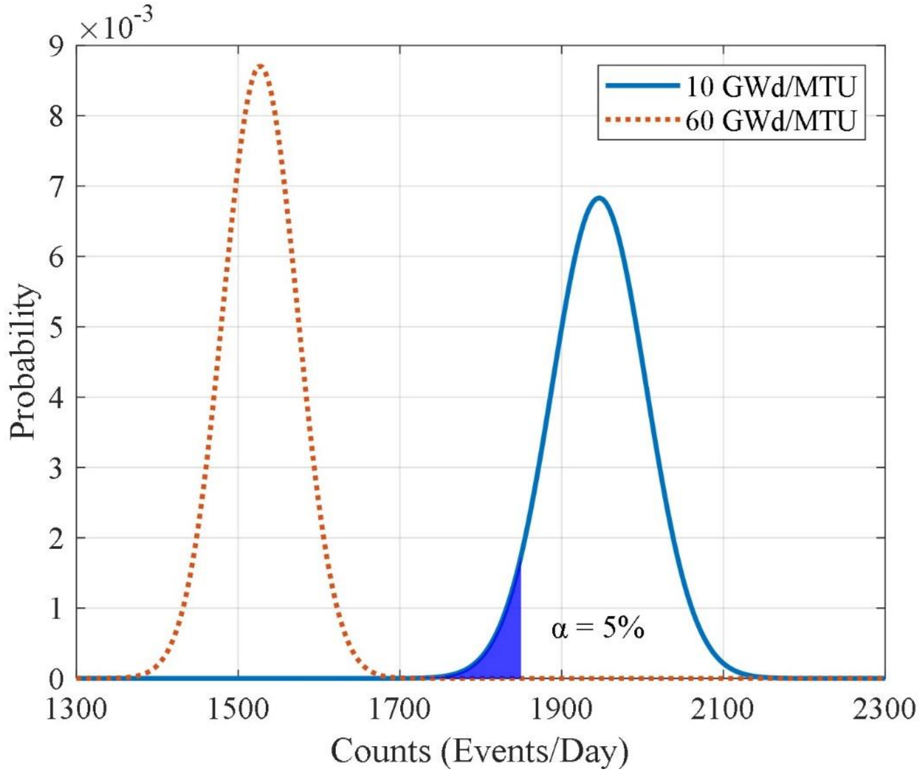

Figure 4-16 The normal distribution of 10 and 60 GWd/MTU counts with 3% uncertainty for 4.4-wt-% ^{235}U case. The non-detection probability, **β** is found at 0% when the false alarm probability, **α** is set at 5%.

Table 4-11 The non-detection probability and detection probability for 4.4-wt-% ^{235}U case.

Burnup (GWd/MTU)	Net Counts (Events/Day)	3% uncertainty	Non-detection Probability (%)	Detection Probability (%)
10	1946.31	58.39	N/A	N/A
10 and 20	1828.09	54.84	34.48	65.52
10 and 40	1646.34	49.39	0.00	100.00
10 and 60	1527.13	45.81	0.00	100.00

For 4.4-wt-% ^{235}U, the integral net counts at 10 and 20 GWd/MTU are 1946.31 ± 58.39 events/day and 1828.09 ± 54.84 events/day, respectively. The non-detection probability

is found to be 34.48% therefore the detection probability is 65.52%. Between 10 and 40 GWd/MTU (1646.34 $\pm$ 49.39 events/day), the non-detection and detection probabilities are 0% and 100%. Lastly, for differentiating 10 and 60 GWd/MTU (1527.13 $\pm$ 45.81 events/day), the detection probability approximates to 100%.

From the above observations, all the comparison cases for both 3.3-wt-% ^{235}U and 4.4-wt-% ^{235}U satisfy the IAEA's requirement, having a minimum of 20% detection probability for all low probability events

4.4. Conclusion and future work

In this work, we study a 100 kg CEνNS based natural germanium detector subjected to 100 DRU background levels and 100 eV$_{NR}$ threshold (1.84 MeV antineutrino energy threshold), placed 25 m away from the AP1000 reactor with burnups varying between 0 GWd/MTU and 60 GWd/MTU. For 3.3-wt-% ^{235}U and 4.4-wt-% ^{235}U enrichment levels the fission fraction of ^{235}U decreased throughout reactor operation due to the depletion of ^{235}U, whereas, the fission fraction of ^{239}Pu increased from the buildup of the inventory due to the ^{238}U neutron capture reaction. The results indicate that ^{238}U capture events should be taken into consideration as they contribute to antineutrino production due to an increase neutron capture with burnup. In general, the antineutrino production rate increases with increasing burnup.

We also developed and implemented pulse height distribution response to the changing antineutrino spectra with burnup. The detector gross count rate and net count rate after 100 DRU background subtraction from 3.3-wt-% ^{235}U and 4.4-wt-% ^{235}U enrichment levels caused an average reduction of counts by 32.64% and 32.58%, respectively. Additionally, when the 100 eV_{NR} threshold is applied to both enrichment levels, more drastic reduction to the gross counts are observed, by 81.03% and 80.61%, respectively.

In addition to differentiating burnups using net integral counts from the germanium CEνNS detector, we also perform an analysis of the shifting end-point energies of the pulse height distributions with increasing burnup. The highest end-point nuclear recoil energies detected by a 100 kg germanium detector after 100 DRU background and 100 eV_{NR} threshold subtractions for 3.3-wt-% ^{235}U enrichment are 293 eV, 273 eV, 262 eV and 257 eV, for 0, 20, 40, and 60 GWd/MTU respectively. A difference of 20 eV and 36 eV is observed between 0 and 20 GWd/MTU, 0 and 60 GWd/MTU. For 4.4-wt-% ^{235}U enrichment, the highest end-point nuclear recoil energies observed are 293 eV, 277 eV, 268 eV, and 261 eV, for 0, 20, 40, and 60 GWd/MTU. The deviation between 0 and 20 GWd/MTU, 0 and 60 GWd/MTU are 16 eV and 32 eV, respectively.

For the 3.3-wt-% ^{235}U enrichment, the detection probabilities of differentiating burnup between 10 and 20 GWd/MTU, 10 and 40 GWd/MTU, and 10 and 60 GWd/MTU are 80.60%, 100%, and 100% respectively. For the 4.4% enrichment case, these detection probabilities become 65.52%, 100%, and 100%. For all the comparison cases, the detection probabilities are higher than 20% confidence, as required by the IAEA.

In future works, we will further investigate the diversion scenarios of plutonium using a similar methodology to determine if such diversions can be detected with confidence.

4.5. Acknowledgement

We would like to express our gratitude to Prof. R. Mahapatra, the spokesperson of Mitchell Institute Neutrino Experiment at Reactor (MINER), for providing valuable data on semiconductor CEvNS detector specifications.

4.6. References

[1] E. Christensen, P. Huber, and P. Jaffke, Antineutrino Reactor Safeguards - a Case Study, 2014. ArXiv:1312.1959.

[2] C. Stewart, A. Abou-Jaoude, and A. Erickson, Employing Antineutrino Detectors to Safeguard Future Nuclear Reactors from Diversions, *Nat. Commun.* 10, 3527, 2019, doi: 10.1038/s41467-019-11434-z.

[3] A. Oralbaev, M. Skorokhvatov, and O. Titov, The Inverse Beta Decay: A Study of Cross Section, *J. Phys.: Conf. Ser.* 675, 012003, 2016, doi: 10.1088/1742-6596/675/1/012003.

[4] PROSPECT Collaboration et al., The PROSPECT Reactor Antineutrino Experiment, *Nuclear Instruments and Methods in Physics Research Section A: Accelerators, Spectrometers, Detectors and Associated Equipment* 922, 287, 2019, doi: 10.1016/j.nima.2018.12.079.

[5] G. L. Fogli, E. Lisi, A. Palazzo, and A. M. Rotunno, KamLAND Neutrino Spectra in Energy and Time: Indications for Reactor Power Variations and Constraints on the Georeactor, *Physics Letters* B 623, 80, 2005, doi: 10.1016/j.physletb.2005.07.064.

[6] W. E. Ang, S. Prasad, and R. Mahapatra, Coherent Elastic Neutrino Nucleus Scatter Response of Semiconductor Detectors to Nuclear Reactor Antineutrinos, N*uclear Instruments and Methods in Physics Research Section A: Accelerators, Spectrometers, Detectors and Associated Equipment* 1004, 165342, 2021, doi: 10.1016/j.nima.2021.165342.

[7] Y. Kim, Detection of Antineutrinos for Reactor Monitoring, *Nuclear Engineering and Technology* 48, 285, 2016, doi: 10.1016/j.net.2016.02.001.

[8] A. C. Hayes and P. Vogel, Reactor Neutrino Spectra, *Annual Review of Nuclear and Particle Science* 66, 219, 2016, doi: 10.1146/annurev-nucl-102115-044826.

[9] Los Alamos National Laboratory: MCNP Home Page. [Online]. Available: https://mcnp.lanl.gov/.

[10] ENDF/B-VIII.0 Evaluated Nuclear Data Library. [Online]. Available: https://www.nndc.bnl.gov/endf/b8.0/.

[11] JEFF-3.3. [Online].
Available: https://www.oecd-nea.org/dbdata/jeff/jeff33/index.html.

[12] V. B. Berestetskii, E. M. Lifshitz, and L. P. Pitaevskii, Chapter XII - Radiative Corrections, in Quantum Electrodynamics (Second Edition), edited by V. B. Berestetskii, E. M. Lifshitz, and L. P. Pitaevskii (Butterworth-Heinemann, Oxford, 1982), 501–596.

[13] A. Sirlin, Radiative Correction to the $\bar{\nu}_e(\nu_e)$ Spectrum in β Decay, *Phys. Rev.* D 84, 014021, 2011, doi: 10.1103/PhysRevD.84.014021.

[14] M. Hone, AP1000 Core Reference Report, 370, 2014.

[15] B. Dutta, R. Mahapatra, L. E. Strigari, and J. W. Walker, Sensitivity to Z-Prime and Non-Standard Neutrino Interactions from Ultra-Low Threshold Neutrino-Nucleus Coherent Scattering, *Phys. Rev.* D 93, 013015, 2016, doi: 10.1103/PhysRevD.93.013015.

[16] P. Coloma, I. Esteban, M. C. Gonzalez-Garcia, and J. Menendez, Determining the Nuclear Neutron Distribution from Coherent Elastic Neutrino-Nucleus Scattering: Current Results and Future Prospects, *J. High Energ. Phys.* 2020, 30, 2020, doi: 10.1007/JHEP08(2020)030.

[17] K. Scholberg, Observation of Coherent Elastic Neutrino-Nucleus Scattering by COHERENT, 2018. ArXiv:1801.05546.

[18] D. A. Sierra, V. De Romeri, and N. Rojas, COHERENT Analysis of Neutrino Generalized Interactions, *Phys. Rev.* D 98, 075018, 2018, doi: 10.1103/PhysRevD.98.075018.

[19] M. Bowen and P. Huber, Reactor Neutrino Applications and Coherent Elastic Neutrino Nucleus Scattering, *Phys. Rev.* D 102, 053008, 2020, doi: 10.1103/PhysRevD.102.053008.

[20] J. Erler and S. Su, The Weak Neutral Current, *Progress in Particle and Nuclear Physics* 71, 119, 2013, doi: 10.1016/j.ppnp.2013.03.004.

[21] W. E. Ang, S. Lee, and S. Prasad, Improvements in Antineutrino Detector Response by Including Fission Product Transitions, *Transactions of the 2021 American Nuclear Society*, 125, (2021) 340-343.

5. LARGE NUCLEAR REACTOR SAFEGUARDS AND MONITORING WITH ANTINEUTRINO DETECTION

5.1. Introduction

International nuclear safeguards have been introduced since the establishment of the Non-Proliferation Treaty (NPT) in 1968 [1]. In the NPT, non-nuclear-weapon states have been required to conclude a comprehensive safeguards agreement (CSA) with International Atomic Energy Agency (IAEA) to place all possessed nuclear material under safeguards [2]. Since then, many traditional safeguard approaches such as inspections and reports, nuclear material verification via non-destructive analysis, and destructive analysis have been introduced to detect diversion of significant quantities of nuclear material in a timely manner. Traditional safeguards tools have been successfully deterred the diversion of nuclear materials, however, they also have required safeguards inspectors to conduct the measurement in the site. Several times in the history of nuclear safeguards, countries like Iran and North Korea have refused or denied inspection visits by the United Nations' IAEA [3] [4]. Thus, with the characteristic of antineutrino where it has very high penetrating power, it is possible to monitor the reactor activity outside the reactor containment.

After coherent elastic neutrino-nucleus scattering had been successfully observed in 2017, this provided an alternative option for nuclear safeguards with antineutrino monitoring [5]. However, reactor-induced neutrino coherent elastic scattering has yet to be observed, so this study is intended to explore the potential of monitoring nuclear reactors via CEνNS. In a previous study, we have shown that assuming a 100 eV_{NR} energy threshold and a background of 100 DRU, the detector can detect the fuel burnup deviation with confidence greater than 20% [6]. In safeguards applications, the IAEA is interested to determine if a diversion of 1 significant quantity (SQ) of nuclear material can be detected with a minimum detection probability of 20% [7]. In this work, three different diversion scenarios are studied: diversion without operator intervention, diversion with operator intervention, and diversion with fresh fuel substitution.

5.2. Methodology

5.2.1. Antineutrino spectrum calculation

The '*ab initio*' summation method is used in this study to model the antineutrino spectrum of a reactor core. Only four fissionable isotopes which are ^{235}U, ^{238}U, ^{239}Pu, and ^{241}Pu are considered as they produce 99.9% of the power in the reactor [8]. A fissionable isotope's antineutrino spectrum can be defined as the summation of all antineutrino spectral from the contributing beta minus decay fission products [8]:

$$\frac{dN}{dE_v} = \sum_n Y_n(Z, A, t) \sum_i b_{n,i}(E_0^i) P_v(E_v, E_0^i, Z) \qquad (5\text{-}1)$$

where $Y_n(Z, A, t)$ is the number of fission fragment Z and A decays at time t. The Y_n is essentially cumulative yield and is independent of t after a reactor has been operated for a long time. The beta intensity, $b_{n,i}$ is the probability of beta decay to a specific excited sate with a given endpoint energy and sums to unity unless the fission fragment has other decay modes than beta minus decay. The normalized antineutrino spectrum is represented by P_v, with E_0^i as the endpoint energy. Two main nuclear libraries which are ENDF/B-

VIII.0 and JEFF-3.3 were used to obtain endpoint energies, beta intensities values, and cumulative yield [9] [10]. The antineutrino spectrum of a fission fragment is described as follows [8]:

$$P_v\left(E_v, E_0^i, Z\right) = kp_e(E_0 - E_e)^2 F(Z, E_e) C(Z, E_e)[1 + \delta(Z, A, E_e)] \qquad (5\text{-}2)$$

where k is the normalization constant, p_e is electron momentum, $F(Z, E_e)$ is the Fermi function, Z is the atomic number, E_v is the initial antineutrino energy, E_e is the total electron energy, E_0 represents the endpoint energy, and $C(Z, E_e)$ is the shape factor. This study assumes that all beta decays are allowed decay, thus $C(Z, E_e) = 1$. The function $\delta(Z, A, E_e)$ comprises finite-size correction, radiative correction, and weak magnetism correction, which should all be taken into account when determining the shape of the spectrum [11] [12] [13]. To obtain the antineutrino spectrum, E_e in the Eq. 5-2 must be substituted with $E_0 - E_v$.

5.2.2. AP1000 reactor modeling

AP1000 design has been used for MCNP 6.2 simulation [14]. The purpose of the simulation is to obtain the fission fraction and fission rate of each fissionable isotope as they can be varied during the operation. The uranium is consumed in the fission process; thus, the inventory of uranium diminishes. However, the content of plutonium will be increased during the neutron absorption. The AP1000 reactor is a commercial pressurized water reactor with a capacity of 3,400 MW(t) designed by Westinghouse Electric Company [15]. The core of the reactor is made up of 157 fuel assemblies, each of which has 264 fuel rods and 25 guide tubes. Figure 5-1 shows the geometry of the AP1000 core design that was used in the simulation. For the simplification purpose, 3.3-wt-% ^{235}U enrichment fuels are used.

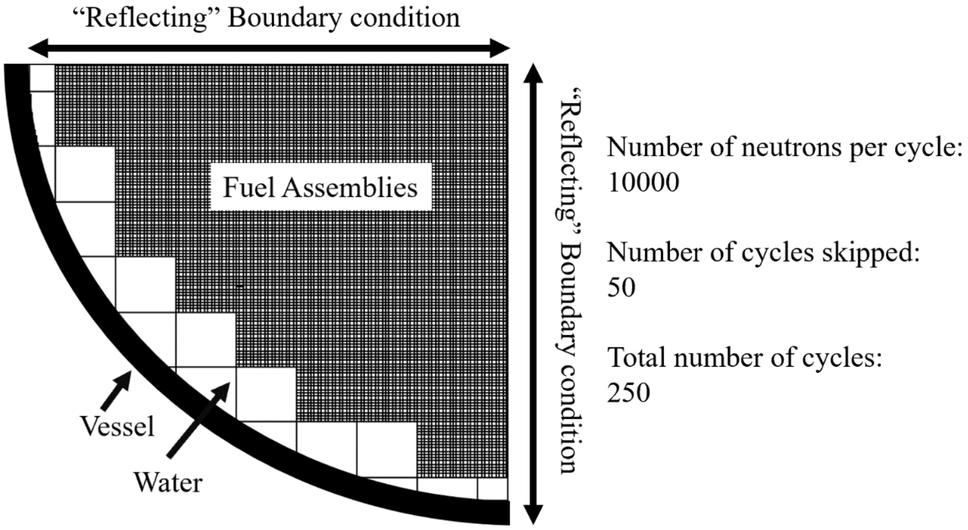

Figure 5-1 Quarter core of AP1000 reactor design, reflecting boundary condition applied. The number of neutrons cycle used in MCNP simulation is 10000, the number of cycles skipped is 50, and the total number of cycles run is 250.

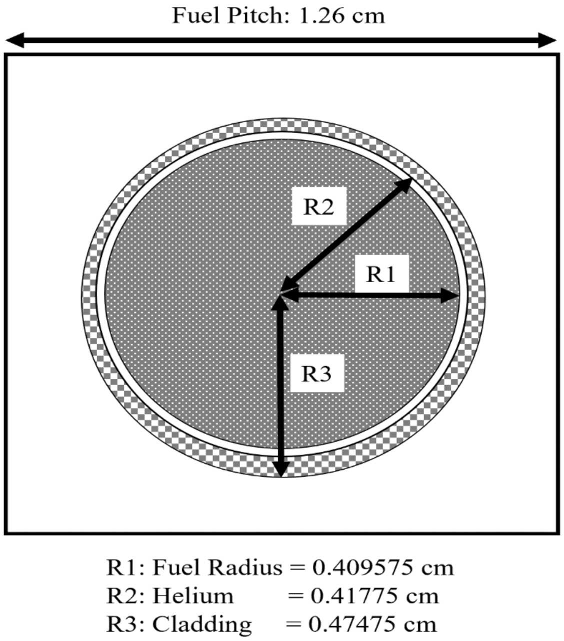

Figure 5-2 The fuel pitch and parameters used in MCNP simulation.

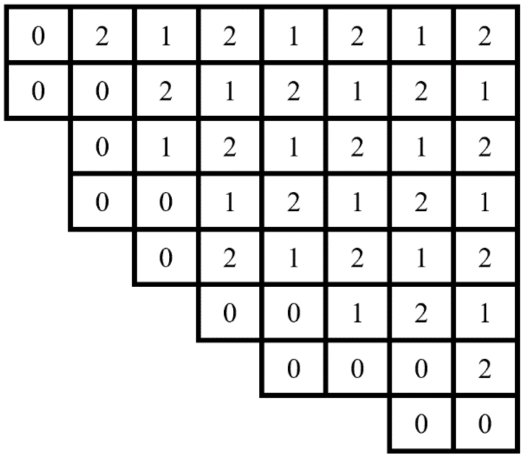

0	2	1	2	1	2	1	2
0	0	2	1	2	1	2	1
	0	1	2	1	2	1	2
	0	0	1	2	1	2	1
		0	2	1	2	1	2
			0	0	1	2	1
				0	0	0	2
						0	0

Figure 5-3 AP1000 reactor quarter core with scatter refueling scheme. The 0 is fresh fuel, 1 is the fuel that burned in one previous cycle and 2 is the fuel that burned in two previous cycles.

At the beginning of the operation, the core was loaded with all 3.3-wt-% ^{235}U enrichment fuels and burned for 390 days to reach 15 GWd/MTU. At the second cycle, 1/3 of the first-cycle fuels were refueled with fresh fuels and continued operating for another 390 days. Lastly, another 1/3 of the second-cycle fuels were loaded with the fresh fuel to reach equilibrium core as shown in Fig 5-2. In this study, we simulate the AP1000 equilibrium core using MCNP for three different diversion scenarios:

a) divert one to four fuel assemblies with operator intervention (cover-up diversion)

b) divert one to four fuel assemblies without operator intervention

c) divert one to four fuel assemblies with fresh fuel substitution

The net counts for 30 days, 60 days, and 90 days are studied for each scenario. The fission fraction and fission rate obtained from MCNP simulation are used to model the antineutrino spectrum and further used to calculate the detector response for each case.

Next, we also compute the antineutrino spectrum of the equilibrium core 1 day, 1 week, 1 month, 3 months, 1 year, 5 years, and 10 years after shutdown. The spent fuel antineutrino spectrum took into consideration of production of daughter beta decay isotopes from parent isotopes. From the example, ^{90}Sr decays to ^{90}Y, which is a beta-decay isotope, via a beta decay reaction [16].

5.2.3. CEνNS cross-section calculation

When a neutrino interacts elastically with a nucleus, it produces a nuclear recoil signal, which is known as coherent-elastic neutrino-nucleus scattering. The pertinent CEνNS cross-section is defined as follows [17]:

$$\frac{d\sigma(E_v)}{dT_R(E_v)} = \frac{G_F^2 M}{2\pi}[(q_v + q_A)^2 + (q_v - q_A)^2 \left(1 - \frac{T_R}{E_v}\right)^2 - (q_v^2 - q_A^2)\frac{MT_R}{E_v^2}] \tag{5-3}$$

where G_F is the Fermi constant, M is the mass of the targeted nucleus, q_v and q_A stand for vector and axial charges, T_R represents the recoil energy, and E_v is incident antineutrino energy [18]. Nuclear recoil energy is proportional to the energy of the incident antineutrino. The maximum recoil energy that an incident antineutrino creates can be calculated with Eq. 5-4 [17].

$$T_R^{Max} = \frac{2E_v^2}{M + 2E_v} \tag{5-4}$$

5.2.4. Detector response and pulse height distribution

The detector response rate is defined as:

$$R(E_v) = N\sigma(E_v)\phi(E_v) \tag{5-5}$$

where N is the number of atoms of the element, $\sigma(E_v)$ is CEvNS cross-section, and $\phi(E_v)$ is the antineutrino flux. The likelihood of the recoiled energies for a given incident antineutrino energy is defined as follows [19]:

$$P(E_v \rightarrow T_R) = \frac{d\sigma(E_v, T_R)}{dT_R} / \sigma(E_v) \qquad (5\text{-}6)$$

Next, pulse height distribution, $C(T_R)$, as a function of T_R is described as below [19]:

$$C(T_R) = \int_{E_v} N\sigma(E_v)\phi(E_v)P(E_v \rightarrow T_R)dE_v \qquad (5\text{-}7)$$

In this study, natural germanium is chosen as the detector material. We also assumed that a 100 kg detector is placed 25 m away from the reactor core, with a 100 $\mathrm{eV_{NR}}$ threshold and background of 100 differentiate rate unit (DRU). 1 DRU is corresponding to 100 detected events/(keV.kg.day) [20].

5.2.5. Non-detection probability

The IAEA has defined a quantity component of the detection goal known as significant quantity. It's defined as the amount of radioactive material for which the prospect of making a nuclear weapon cannot be ruled out. As indicated in Fig. 5-1, the significance of a substantial quantity varies depending on the type of nuclear material [6].

Table 5-1 Significant quantity of nuclear material.

Material	Significant Quantity
$^{235}U < 20\%$	75 kg ^{235}U (or 10 t natural uranium or 20 t depleted uranium)
$^{235}U \geq 20\%$	25 kg ^{235}U
^{233}U	8 kg ^{233}U
Pu	8 kg Pu
Th	20 t Th

For low likelihood occurrences, the IAEA demands a detection probability of greater than 20%. As plutonium is categorized as irradiated direct use material, the detection goal of IAEA is 3 months. We define detection probability, P_{det} as [6]:

$$P_{det} = 1 - \beta \qquad (5\text{-}8)$$

where β is non-detection probability. The CDF (cumulative distribution function) function in Matlab software is used to determine the alarm threshold for a non-diversion scenario [21]. To avoid a large number of false alarms, a value of 5% was set for false alarm probability, α [6] [22]. For each diversion case, the non-detection probability can be calculated using the given alarm threshold, with NORMPDF (normal probability density function) function in Matlab software. Fig. 5-4 shows the example of both normal probability distribution for non-diversion and diversion cases, with alarm threshold, non-detection probability, β and false alarm probability, α. All cases are applied with a 3% uncertainty to the detector counts, which accounts for 1% uncertainty in operating power, 1% in detection and instrumentation, and another 1% uncertainty in counting statistics.

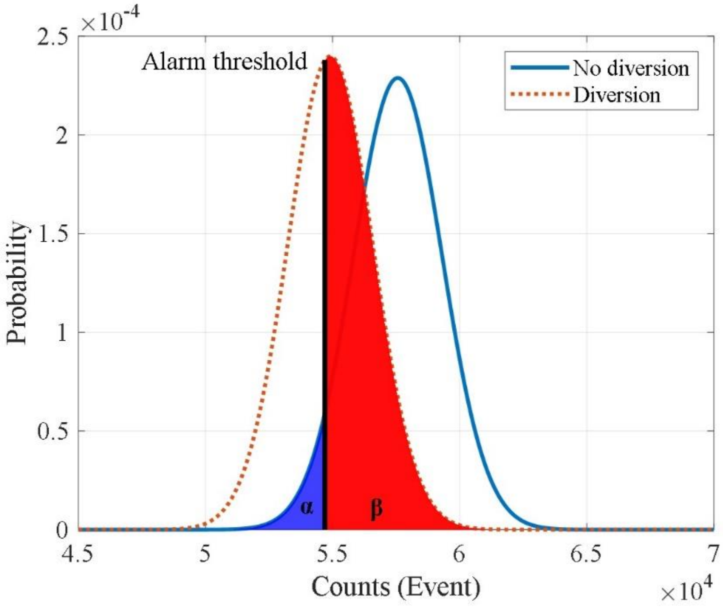

Figure 5-4 The plot of false alarm probability, α (5%), alarm threshold, and non-detection probability.

5.3. Results and discussion

In this section, we will discuss the detection probability before and after diversion of one fuel assembly up to four fuel assemblies based on the scenario discussed in section 5.2.2. The fuel assemblies that are removed from the core are first-cycle burned fuel which contains approximately 4.47 kg Pu per fuel assembly. Thus, removing two fuel assemblies representing 1 SQ of Pu will be removed from the core. Table 5-1 shows the expected net counts before diversion with 30 days, 60 days, and 90 days duration.

Table 5-2 Net counts without diversion after 30 days, 60 days, and 90 days.

Measurement Duration	Net count (Events)
30 days	57,565.67 ± 1,743.56
60 days	113,794.85 ± 3,430.47
90 days	168, 939.38 ± 5,084.82

Table 5-2 will be used to compare the net count after the fuel assembly's removal and calculate both non-detection and detection probability.

5.3.1. Diversion with operator intervention

In this diversion scenario, we assumed the operator of the facility will remove one to four fuel assemblies and maintain the power level, which is 3,400 MW(th) in our study. It is assumed that the operator intervenes and deliberately recovers the reactor power to the usual operating power, to mask the diversion.

Table 5-3 Net counts and detection probability after one fuel assembly removal (0.56 SQ) for diversion with operator intervention.

Measurement Duration	Net counts (Events)	Non-detection probability (%)	Detection probability (%)
30 days	57,535.05 ± 1,726.05	94.82	5.18
60 days	113,829.44 ± 3,414.88	94.89	5.11
90 days	169,039.05 ± 5,071.17	94.78	5.22

Table 5-3 shows the net counts and detection probabilities after one fuel assembly is removed from the core. After 30 days, 60 days, and 90 days, the overall counts are 57,565.67 ± 1,726.05 events, 113,829.44 ± 3,414.88 events, and 169,039.05 ± 5,071.17

events, respectively. With only a 5% detection probability, the detection probabilities after 30 days, 60 days, and 90 days are nearly identical.

Table 5-4 Net counts and detection probability after two fuel assemblies' removal (1.12 SQ) for diversion with operator intervention

Measurement Duration	Net counts (Events)	Non-detection probability (%)	Detection probability (%)
30 days	57,612.56 ± 1,728.38	94.70	5.30
60 days	113,957.86 ± 3,418.74	94.46	5.54
90 days	169,262.69 ± 5,077.88	94.27	5.73

Table 5-4 shows the net counts and detection probabilities after two fuel assemblies are removed from the core. The total count obtained after 30 days, 60 days and 90 days are 57,612.56 ± 1,728.38 events, 113,957.86 ± 3,414.74 events, and 169,262.69 ± 5,077.88 events respectively. The detection probabilities after 30 days, 60 days, and 90 days are approximately the same with only 5% to 6% detection probabilities.

Table 5-5 Net counts and detection probability after three fuel assemblies' removal (1.68 SQ) for diversion with operator intervention

Measurement Duration	Net counts (Events)	Non-detection probability (%)	Detection probability (%)
30 days	57,698.61 ± 1,730.96	94.11	5.89
60 days	114,169.10 ± 3,425.07	93.70	6.30
90 days	169,507.38 ± 5,085.22	93.67	6.33

Table 5-5 displays the net counts and detection probabilities after removing three fuel assemblies from the core. After 30 days, 60 days, and 90 days, the total counts are 57,698.61 ± 1,730.96 events, 114,169.10 ± 3,425.07 events, and 169,507.38 ± 5,085.22

events, respectively. The detection probabilities after 30 days, 60 days, and 90 days are lower than the IAEA requirement, with only 5.89%, 6.30%, and 6.33%, respectively.

Table 5-6 Net counts and detection probability after four fuel assemblies' removal for (2.24 SQ) diversion with operator intervention

Measurement Duration	Net counts (Events)	Non-detection probability (%)	Detection probability (%)
30 days	57,703.25 ± 1,731.10	94.08	5.92
60 days	114,178.41 ± 3,425.35	93.36	6.34
90 days	169,598.24 ± 5,087.95	93.34	6.57

Lastly, the detection probabilities after removing four fuel assemblies are slightly higher than the above cases. The total counts for 30 days, 60 days and 90 days after removing 4 fuel assemblies are 57,703.25 ± 1,731.10 events, 114,178.41 ± 3,425.35 events, and 169,598.24 ± 5,087.95 events, respectively. The detection probabilities after 30 days, 60 days, and 90 days are 5.92%, 6.34%, and 6.57% respectively.

Overall, if the operator maintains the power level of the reactor, it is very difficult for to the inspector to detect such diversions as the deviation fission rate before and after division is small due within 90 days. Generally, the detection probabilities for one to four fuel assemblies are not more than 7%, which are lower than IAEA's requirement of 20% detection probability.

5.3.2. Diversion without operator intervention

In this section, we assumed the operator will remove one to four fuel assemblies during the refueling phase such that the reactor power is reduced to a lower level. It is assumed that the operator does not try to recover the reactor power after the fuel assemblies are removed. However, this is unlikely as changing reactor power might be detected by the unattended monitoring systems of IAEA such as radiation monitors and sensors.

Table 5-7 Net counts and detection probability after one fuel assembly removal (0.56 SQ) for diversion without operator intervention.

Measurement Duration	Net counts (Events)	Non-detection probability (%)	Detection probability (%)
30 days	56,809.22 ± 1,704.28	88.93	11.07
60 days	112,405.89 ± 3,372.18	89.49	10.51
90 days	166,895.12 ± 5,006.85	89.55	10.45

The total net count after 30 days of diverting one fuel assembly is 56,809.22 ± 1,704.28 events, where a detection probability of 11.07% can be expected. At 60 days, the detection probability is 10.51% with 112,405.89 ± 3,372.18 events. Lastly, after 90 days, the net count is 166,895.12 ± 5,006.85 events, with 10.45% detection probability.

Table 5-8 Net counts and detection probability after two fuel assemblies' removal (1.12 SQ) for diversion without operator intervention.

Measurement Duration	Net counts (Events)	Non-detection probability (%)	Detection probability (%)
30 days	56,191.93 ± 1,685.76	80.79	19.21
60 days	111,177.14 ± 3,335.31	81.55	18.45
90 days	165,127.62 ± 4,953.83	81.94	18.06

For the case of removing two fuel assemblies from the core, the net counts after 30 days, 60 days, and 90 days are 56,191.93 ± 1,685.76 events, 111,177.14 ± 3335.31 events, and 165,127.62 ± 4,953.83 events, respectively. By removing two fuel assemblies, there is an approximately 1.27% reduction in power. The detection probabilities are increased compared to only one fuel assembly's removal with 19.21%, 18.45%, and 18.06% for 30 days, 60 days, and 90 days.

Table 5-9 Net counts and detection probability after three fuel assemblies' removal (1.68 SQ) for diversion without operator intervention.

Measurement Duration	Net counts (Events)	Non-detection probability (%)	Detection probability (%)
30 days	55,554.48 ± 1,666.63	69.07	30.93
60 days	109,879.73 ± 3,296.39	69.68	30.32
90 days	163,197.16 ± 4,895.91	70.18	29.82

Table 5-9 shows the net counts, non-detection probabilities, and detection probabilities after 30 days, 60 days, and 90 days after three fuel assemblies' removal. The counts after 30 days, 60 days, and 90 days are 55554.48 ± 1666.63 events, 109879.73 ± 3296.39 events, and 163197.16 ± 4895.91 events, respectively. The detection probability is improved to approximately 30% in 3 months. The detection probability after removing three fuel assemblies is higher than two fuel assemblies' removal.

Table 5-10 Net counts and detection probability after four fuel assemblies' removal for (2.24 SQ) for diversion without operator intervention.

Measurement Duration	Net counts (Events)	Non-detection probability (%)	Detection probability (%)
30 days	54,908.02 ± 1,647.24	54.42	45.58
60 days	113,829.44 ± 3,414.88	54.44	45.56
90 days	169,039.05 ± 5,071.17	55.23	44.77

The net counts for removing four fuel assemblies after 30 days, 60 days and 90 days are 54,908.02 ± 1,647.24 events, 113, 829.44 ± 3,414.88 events, and 169,039.05 ± 5071.17 events, respectively. Overall, diversion of four fuel assemblies can be detected with approximately 45% confidence.

The detection of diversion without operator intervention is possible because removal of 1 to 4 fuel assemblies lead to a power reduction of 0.64%, 1.27%, 1.91%, and 2.55%, so the decreasing of fission rate. Thus, the deviation of net counts before and after diversion can be distinguished. However, the IAEA requirement of 20% detection probability can only be fulfilled when a minimum of three fuel assemblies is removed from the core.

5.3.3. Diversion with fresh fuel substitution

In this case, we presumed that the operator would replace the missing or diverted fuel assemblies with fresh fuel assemblies. During the refueling phase, the operator might attempt to pass undetected by replacing the missing or diverted with dummy fuel assemblies.

Table 5-11 Net counts and detection probability after one fuel assembly removal (0.56 SQ) for diversion with fresh fuel substitution.

Measurement Duration	Net counts (Events)	Non-detection probability (%)	Detection probability (%)
30 days	57,518.25 ± 1,725.55	94.73	5.27
60 days	113,796.55 ± 3,413.90	94.99	5.01
90 days	169,084.12 ± 5,072.52	94.68	5.32

After 30 days, the net counts reached 57,518.25 ± 1,725.55 events, with detection probability only 5.27% after one fuel assembly is diverted. Similarly, the detection probabilities do not change significantly after 60 days and 90 days with 5.01% and 5.32% respectively. The total counts for both 60 days and 90 days are 113,796.55 ± 3,413.90 events and 169,084.12 ± 5072.52 events.

Table 5-12 Net counts and detection probability after two fuel assemblies' removal (1.12 SQ) for diversion with fresh fuel substitution.

Measurement Duration	Net counts (Events)	Non-detection probability (%)	Detection probability (%)
30 days	57,490.74 ± 1,724.72	94.56	5.44
60 days	113,785.23 ± 3,413.56	94.97	5.03
90 days	169,068.67 ± 5,072.06	94.71	5.29

Table 5-12 shows the net counts for removing two fuel assemblies after 30 days, 60 days and 90 days are 57,490.74 ± 1,724.72 events, 113,785.23 ± 3,413.56 events, and 169,068.67 ± 5,072.06 events. The detection probabilities for these 3 durations are approximately the same, where the anomaly can only be detected with 5.44%, 5.03%, and 5.29%, respectively.

Table 5-13 Net counts and detection probability after three fuel assemblies' removal (1.68 SQ) for diversion with fresh fuel substitution.

Measurement Duration	Net counts (Events)	Non-detection probability (%)	Detection probability (%)
30 days	57,418.41 ± 1,722.55	94.10	5.90
60 days	113,719.07 ± 3,411.57	94.77	5.23
90 days	169,027.87 ± 5,070.84	94.80	5.20

After 3 first-cycle burned fuels have been diverted from the core and substituted with the fresh fuels, the net counts for 30 days, 60 days, and 90 days are 57,418.41 ± 1,722.55 events, 113,719.07 ± 3,411.57 events, and 169,027.87 ± 5,070.84 events. The detection probabilities for these three durations are about the same where approximately only 5% detection probability is expected.

Table 5-14 Net counts and detection probability after four fuel assemblies' removal (2.24 SQ) for diversion with fresh fuel substitution.

Measurement Duration	Net counts (Events)	Non-detection probability (%)	Detection probability (%)
30 days	57,454.29 ± 1,723.63	94.33	5.67
60 days	113,815.44 ± 3,414.46	94.93	5.07
90 days	169,124.36 ± 5,073.73	94.59	5.41

Table 5-14 shows the net counts and detection probabilities after four fuel assemblies are diverted from the core and substituted with dummy fuel assemblies. The net counts for 30 days, 60 days and 90 days are 57,454.29 ± 1,723.63 events, 113,815.44 ± 3,414.46 events, and 169,124.36 ± 5,073.73 events, respectively. The detection probabilities for all three durations are almost identical with 5.67%, 5.07%, and 5.41%.

From the above results, it is difficult to determine if diversion is taking place if the missing fuel assembly is substituted with fresh fuel and constant power. The fission fraction between diversion and without diversion is small within 90 days and the deviation of the fission rate is also minor. Thus, the proliferator who attempts diversion by this approach maybe pass undetected by safeguards inspectors.

5.3.4. Power reduction without diversion

Next in this section, we reduced the original power with 1 to 10% reduction to study the impact on the detection probability. We also applied a 3% uncertainty to the detector count rate, which accounts for 1% uncertainty in operating power, 1% in detection and instrumentation, and another 1% due to uncertainty in counting statistics.

Table 5-15 Net counts and detection probability of power reduction.

Power Reduction	Count rate (Events/day)	Non-detection probability (%)	Detection probability (%)
0%	1,977.33 ± 59.32	N/A	N/A
1%	1,939.45 ± 58.18	84.66	15.34
2%	1,901.36 ± 57.04	64.60	35.40
3%	1,863.44 ± 55.90	38.35	61.65
4%	1,825.68 ± 54.77	16.07	83.93
5%	1,788.34 ± 53.65	4.38	95.62
6%	1,751.00 ± 52.53	0.70	99.30
7%	1,713.86 ± 51.42	0.06	99.94
8%	1,676.90 ± 50.31	0.00	100.00
9%	1,640.10 ± 49.20	0.00	100.00
10%	1,603.51 ± 48.11	0.00	100.00

From Table 5-14, the detection probabilities of 1 to 7% reduction in reactor power when compared to full power are 15.34%, 35.40%, 61.65%, 83.93%, 95.62%, 99.30%, and 99.94%. The detection probabilities from 8% to 10% reduction in reactor power are identical, with 100% detection probability.

The above results show that power reduction from 1% to 3% has detection probability not more than 62%. Power reduction of 2% can be detected with minimum IAEA requirement, with 35.40%. However, power reduction from 4% to 10% can be detected with more than 80% confidence.

5.3.5. Shutdown / spent fuel antineutrino spectrum

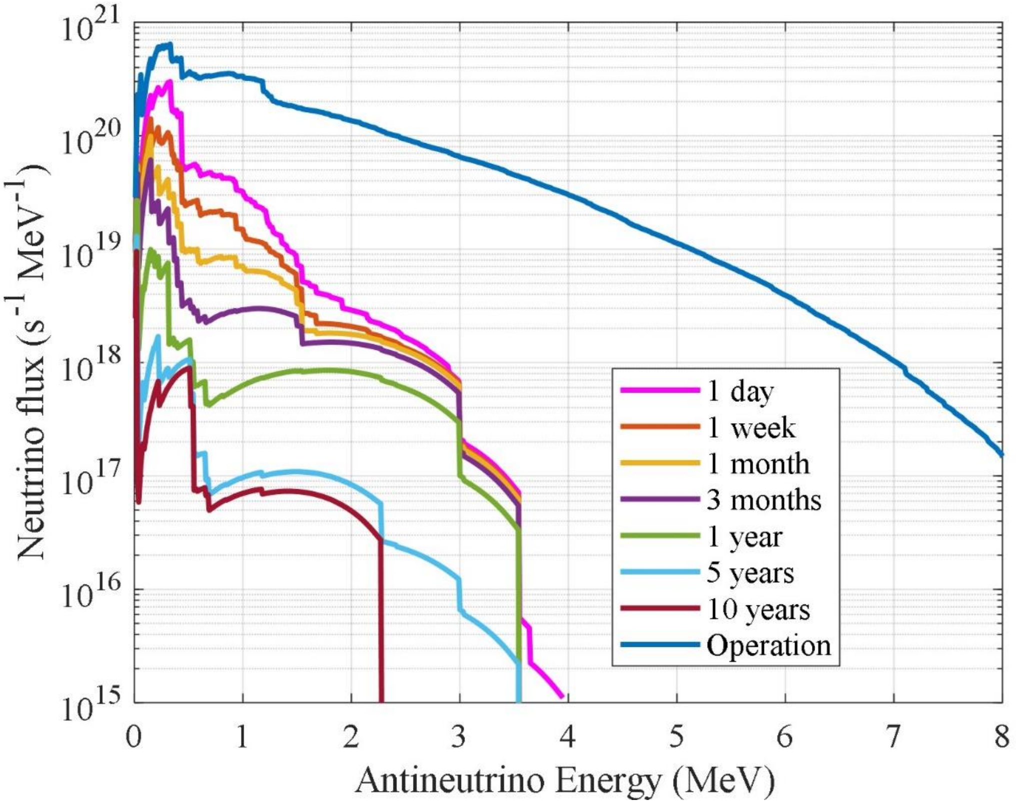

Figure 5-5 The antineutrino spectrum during the operation, 1 day, 1 week 1 month, 3months, 1 year, 5 years and 10 years after shutdown.

Fig. 5-5 shows the reactor antineutrino spectrum during operation, 1 day, 1 week 1 month, 3 months, 1 year, 5 years, and 10 years after shutdown. As the neutrino flux is decreased sharply after 1-day shutdown, the detector is now placed 3 m away from the core with 100 eV_{NR} threshold and 100 DRU background.

Table 5-16 Net counts and detection probability after the reactor is shutdown.

Time of Detection	Net count rate (Events/day)	Non detection probability	Detection probability
1 day	181.48 ± 5.44	N/A	N/A
1 week	93.97 ± 2.82	0%	100%
1 month	70.34 ± 2.11	0%	100%
3 months	29.44 ± 0.88	0%	100%
1 year	0.00	N/A	N/A
5 years	0.00	N/A	N/A
10 years	0.00	N/A	N/A

The net counts after reactor shutdown measured after 1 day, 1 week, 3 months are 181.48 ± 5.44 events/day, 93.97 ± 2.82 events/day, 70.34 ± 2.11 events/day, and 29.44 ± 0.88 events/day, respectively. The result from Table 5-16 shows that the net count rate deviation between 1-day after shutdown with 1 week, 1 month, and 3 months after reactor shutdown can be detected with a detection probability approximately 100%. After 1 year, 5 years, and 10 years after shutdown of the reactor, a detector with 100 eV_{NR} and 100 DRU limitation is not able to detect antineutrino with sufficient counts. After 1 year of reactor shutdown, the main contributor of the antineutrino spectrum with energy more than 2 MeV is ^{90}Y with 2.2798 MeV and ^{106}Rh with 3.545 MeV. However, 100 eV_{NR} Ge detector can only detect minimum antineutrino energy of 1.84 MeV, thus detector threshold less than 100 eV_{NR} and low background are highly favorable to improve the detection efficiency.

5.4. Conclusion

Overall, for the case of the diversion with operator intervention, inspectors will have difficulty detecting the diversion as the detection probabilities for one to four fuel assemblies are less than 7%, which is less than IAEA's requirements of 20% detection probabilities. This is because the changes to the fission rates within the first 3 months are generally small.

Next, for the case of diversion without operator intervention, the detection probabilities for the removal of one fuel assembly, two fuel assemblies, three fuel assemblies, and four fuel assemblies are approximately 10%, 18%, 30%, and 45%. Detection of such diversions is not possible per IAEA's requirement of 20% probability for less than three fuel assemblies removed from the core, which is more than 1 SQ of plutonium. On the other hand, removing three or more fuel assemblies satisfies IAEA's minimum requirement of 20% detection probability.

For the case of diversion with dummy substitution, it is hard to tell if such diversion is occurring as the detection probabilities for removal of one to four fuel assemblies are not more than 6%. Within 3 months, the fission fraction difference between diversion and without diversion is minimal. As a result, a proliferator attempting diversion in this duration may be undetected by the inspectors.

The detection probabilities of 1% to 7% power reduction without diversion when compared to full power are 15.34%, 35.40%, 61.65%, 83.93%, 95.62% and 99.94%

respectively. The detection probability is approximately 100% when power is reduced beyond 8%. The aforementioned findings show that reducing the power from 1% to 3% can be detected with no more than 62% confidence. The minimum requirement of IAEA can only be fulfilled by greater than 2% power reduction such that the detection probability will be more than 35.40%. Power drop from 4% to 10%, can be recognized with greater than 80% confidence.

Lastly, the detection probabilities of net count rate deviation at 1 week, 1 month, and 3 months after the shutdown are approximately 100% when compared to 1 day after shutdown of the reactor. After 1 year, 5 years, and 10 years after reactor shutdown, a detector with a threshold of 100 eV_{NR} and background of 100 DRU is unable to detect sufficient antineutrinos. To maximize the detection efficiency, a detector threshold of less than 100 eV_{NR} and a low background are particularly beneficial.

5.5. References

[1] The IAEA and the Non-Proliferation Treaty. [Online]. Available: https://www.iaea.org/topics/non-proliferation-treaty.

[2] INFCIRC/153(Corrected) - The Structure and Content of Agreements Between the Agency and States Required in Connection with the Treaty on the Non-Proliferation of Nuclear Weapons. [Online]. Available: https://www.iaea.org/sites/default/files/publications/documents/infcircs/1972/infcirc153.pdf.

[3] IAEA and Iran: Chronology of Key Events. [Online]. Available: https://www.iaea.org/newscenter/focus/iran/chronology-of-key-events.

[4] IAEA and DPRK: Chronology of Key Events. [Online]. Available: https://www.iaea.org/newscenter/focus/dprk/chronology-of-key-events.

[5] D. Akimov et al., Observation of Coherent Elastic Neutrino-Nucleus Scattering, *Science* 357, 1123, 2017, doi: 10.1126/science.aao0990.

[6] International Atomic Energy Agency, IAEA Safeguards Glossary 2001 Edition. [Online].
Available: https://www.iaea.org/sites/default/files/iaea_safeguards_glossary.pdf.

[7] V. Fortakov, Nuclear Verification: What it is, how it works, the assurances it can provide, Technical workshop on safeguards, verification technologies, and other related experience. [Online].
Available: https://www.osti.gov/etdeweb/servlets/purl/703309.

[8] A. C. Hayes and P. Vogel, Reactor Neutrino Spectra, *Annual Review of Nuclear and Particle Science* 66, 219, 2016, doi: 10.1146/annurev-nucl-102115-044826.

[9] ENDF/B-VIII.0 Evaluated Nuclear Data Library. [Online]. Available: https://www.nndc.bnl.gov/endf/b8.0/.

[10] JEFF-3.3. [Online].
Available: https://www.oecd-nea.org/dbdata/jeff/jeff33/index.html.

[11] P. Huber, On the Determination of Anti-Neutrino Spectra from Nuclear Reactors, *Phys. Rev.* C 84, 024617, 2011, doi: 10.1103/PhysRevC.84.024617.

[12] V. B. Berestetskii, E. M. Lifshitz, and L. P. Pitaevskii, Chapter XII - Radiative Corrections, in Quantum Electrodynamics (Second Edition), edited by V. B.

Berestetskii, E. M. Lifshitz, and L. P. Pitaevskii (Butterworth-Heinemann, Oxford, 1982), pp. 501–596.

[13] A. Sirlin, Radiative Correction to the $\bar{\nu}_e(\nu_e)$ Spectrum in β Decay, *Phys. Rev.* D 84, 014021, 2011, doi: 10.1103/PhysRevD.84.014021.

[14] Los Alamos National Laboratory: MCNP Home Page. [Online]. Available: https://mcnp.lanl.gov/.

[15] M. Hone, AP1000 Core Reference Report, 370, 2014.

[16] V. Brdar, P. Huber, and J. Kopp, Antineutrino Monitoring of Spent Nuclear Fuel, *Phys. Rev. Applied* 8, 054050, 2017, doi: 10.1103/PhysRevApplied.8.054050.

[17] B. Dutta, R. Mahapatra, L. E. Strigari, and J. W. Walker, Sensitivity to Z-Prime and Non-Standard Neutrino Interactions from Ultra-Low Threshold Neutrino-Nucleus Coherent Scattering, *Phys. Rev.* D 93, 013015, 2016, doi: 10.1103/PhysRevD.93.013015.

[18] J. Erler and S. Su, The Weak Neutral Current, *Progress in Particle and Nuclear Physics* 71, 119, 2013, doi: 10.1016/j.ppnp.2013.03.004.

[19] W. E. Ang, S. Prasad, and S. S. Chirayath, Antineutrino Detection for Temporal Monitoring of Fuel Burnup in a Large Nuclear Reactor, *Nuclear Instruments and Methods in Physics Research Section A: Accelerators, Spectrometers, Detectors and Associated Equipment* 166353, 2022, doi: 10.1016/j.nima.2022.166353.

[20] B. Dutta, Y. Gao, A. Kubik, R. Mahapatra, N. Mirabolfathi, L. E. Strigari, and J. W. Walker, Sensitivity to Oscillation with a Sterile Fourth Generation Neutrino

from Ultralow Threshold Neutrino-Nucleus Coherent Scattering, *Phys. Rev.* D 94, 093002, 2016, doi: 10.1103/PhysRevD.94.093002.

[21] MATLAB - MathWorks. [Online]. Available: https://www.mathworks.com/products/matlab.html.

[22] C. Stewart, A. Abou-Jaoude, and A. Erickson, Employing Antineutrino Detectors to Safeguard Future Nuclear Reactors from Diversions, *Nat. Commun.* 10, 3527, 2019, doi: 10.1038/s41467-019-11434-z.

6. CONCLUSIONS

This work studies CEvNS detector responses to reactor electron antineutrinos as a new method for neutrino detection with widespread applications, including the ones investigated here for nuclear security and nuclear power monitoring. Specifically, this work uses semiconductor reaction rates and their pulse height distributions for operation and nonproliferation analysis of a 1 MW TRIGA research reactor in steady-state operation, an AP-1000 type commercial reactor in quasi-steady-state operation with burnup feedback at different times, and detection response after reactor shutdown.

In this work, reactor antineutrino spectra have been modeled using a summation of antineutrino spectra from hundreds of fission products with various corrections for a nucleus' finite-size, weak magnetism, and radiative losses. The results from Chapter 2 demonstrate the importance of including fission product excited states into antineutrino spectrum calculations by comparing them to the spectrum without excited states and show that the impact on the detector response is significant. The absence of excited states in the antineutrino spectrum causes more than 38% overestimation of detector response. On the other hand, the contributions from finite-size correction, weak magnetism correction, and radiative correction cause only 0.7% to 0.9% increment in the detector response. TAGS data sets, which are free from the pandemonium effect are used in this work to improve the accuracy of the spectrum. Including the TAGS data set reduces the detector response by 1.7% to 1.8%, according to the findings. Chapter 2 also presents the probability distribution of recoil energies for a given incident antineutrino energy and pulse height distribution for both Ge and Si detectors when they are placed 10 m away from the 1 MW TRIGA reactor core.

Secondly, this work compares the detector responses of CEνNS detectors with the IBD detectors. In Chapter 3, Ge CEνNS detectors and Si CEνNS detectors have been used to compare to IBD detectors. The results show that CEνNS detectors have higher detection efficiency compared to IBD. Germanium has the largest flux-weighted average CEνNS cross section, an order of magnitude larger than Si CEνNS cross section, and two orders of magnitude higher than the average IBD cross section. Germanium detectors are found 2.85 times more efficient than Si detectors, and 27.19 times more efficient than IBD detectors. However, Si detectors are more sensitive to lower antineutrino energy. The results show that a threshold of 20 eV_{NR} renders 33.10% of antineutrinos from a 1 MW TRIGA reactor undetected in natural Ge and 20.26% of antineutrinos undetectable in natural Si. In both natural Ge and natural Si, increasing the threshold to 100 eV_{NR} renders 66.95% and 46.02% of antineutrinos undetected, respectively. The current IBD threshold leaves 66.17% of the antineutrino population undetected.

Chapter 4 demonstrates that a CEνNS detector can be used to detect antineutrino produced from an AP1000-type fission reactor from a distance of 25 m. The results show that the fuel burnup can be distinguished by their endpoint nuclear recoil energies. A 16 eV_{NR} is required to distinguish fresh fuel from 20 GWd/MTU burned fuel. According to the study, the endpoint nuclear recoil energies with increasing fuel burnup become less separable. As a result, better resolution is required for more burned fuel. The detection probabilities calculation for 10 and 20 GWd/MTU, 10 and 40 GWd/MTU, 10 and 60

GWd/MTU for both 3.3-wt-% ^{235}U and 4.4-wt-% ^{235}U have been carried out in this study. The results show that the fuel burnup variations can be identified with more than 20% detection probability, as required by the IAEA.

Lastly, nonproliferation analyses for diversion cases are carried out for an AP1000-type reactor. There are three different diversion scenarios presented in Chapter 5: diversion with operator intervention, diversion without operator intervention, and diversion with fresh fuel substitution. The analyses show that after removing 1 to 4 fuel assemblies, detection of diversion without any changing the reactor power or with operator intervention is not possible due to low detection probabilities, with only a 7% confidence level. For a diversion without operator intervention by way of reducing the reactor power, the minimum IAEA's detection probability of 20% can only be fulfilled if 3 of more fuel assemblies are removed from the core. For the diversion case with fresh fuel substitution after removing burned fuel containing high amounts of Pu, it is shown that such diversion is also not possible as the detection probabilities are less than 6%. This research also shows that a power drop of 4% or more without diversion can be identified with a detection probability of more than 80%. Lastly, the deviations of net count rate at one week, one month, and three months after shutdown can be detected with a detection probability of 100% when compared to one-day shutdown of the reactor.

This research is unique because of the possibility of using CEνNS detector to monitor reactor power outside containment. The findings from this research show that a relatively small size CEνNS detector (kg-scale) can be deployed outside the reactor to monitor reactor power with higher detection efficiency compared to the IBD detector.

Since CEνNS has a relatively higher cross-section and detection efficiency than the IBD, it could be a cheaper and more portable antineutrino detector option for safeguards purposes. This research is also significant as it shows the diversions of more than 1 SQ Pu are difficult to detect especially for the cases of diversion with operator intervention and diversion with fresh fuel substitution. However, a reactor power drop of 4% or more can be detected with more than 80% confidence using a 100 kg Ge detector with a energy threshold of 100 eV_{NR} and a background 100 DRU. Thus, it is recommended that CEνNS detectors be used as a complimentary safeguards tool rather than completely substitute the conventional safeguards, such as, the gamma spectroscopy technique.

In future works, more research can be done by exploring the possibility of using CEνNS detectors with lower threshold and reducing background levels to efficiently monitor reactor power inside and outside the reactor building. This research has been focused on two types which are a research reactor and commercial light-water reactor. Similar analysis can be conducted on various type of advanced-reactor designs such as fast reactors, pebble-bed reactors, or molten salt reactors to further this analysis. The study of employing CEνNS detector in a nuclear accident also can be conducted to determine the possibility for disaster radiation monitoring.

APPENDIX A

TOTAL ABSORPTION GAMMA SPECTROSCOPY DATA SETS

References	Isotopes
R.C. Greenwood *et al.* (1997)	^{89}Rb ^{90}Rb ^{90m}Rb ^{93}Rb ^{93}Sr ^{94}Sr ^{94}Y ^{95}Sr ^{95}Y ^{138}Cs ^{138m}Cs ^{139}Cs ^{140}Cs ^{141}Cs ^{141}Ba ^{142}Ba ^{142}La ^{143}Ba ^{143}La ^{144}Ba ^{144}La ^{145}Ba ^{145}La ^{145}Ce ^{146}Ce ^{146}Pr ^{147}Ce ^{147}Pr ^{148}Ce ^{148}Pr ^{148m}Pr ^{149}Pr ^{149}Nd ^{151}Pr ^{151}Nd ^{152}Nd ^{152}Pm ^{153}Nd ^{153}Pm ^{154}Nd ^{154}Pm ^{155}Nd ^{155}Pm ^{156}Pm ^{157}Pm ^{157}Sm ^{158}Sm ^{158}Eu
A. Algora *et al.* (2010)	^{102}Tc ^{104}Tc ^{105}Tc ^{106}Tc ^{107}Tc ^{105}Mo ^{101}Nb
A. A. Zakari-Issoufou *et al.* (2015)	^{92}Rb
S. Rice *et al*. (2017)	^{86}Br ^{91}Rb
L. Le Meur PhD thesis (2018)	^{99}Y ^{142}Cs ^{138}I
V. Guadilla *et al.* (2019)	^{100}Nb ^{100m}Nb ^{102}Nb ^{102m}Nb
J. Gombas *et al.* (2021)	^{103}Nb ^{104m}Nb

APPENDIX B

BETA CONTINUOUS SPECTRUM FROM JENDL-2015

Atomic number (Z)	Isotopes
29	^{71}Cu
30	^{74}Zn ^{79}Zn
31	^{77}Ga ^{82}Ga ^{83}Ga
32	^{84}Ge ^{85}Ge ^{86}Ge ^{87}Ge
33	^{83}As ^{85}As ^{86}As ^{87}As ^{88}As ^{89}As ^{90}As
34	^{88}Se ^{89}Se ^{90}Se ^{91}Se ^{92}Se
35	^{92}Br ^{93}Br ^{94}Br ^{95}Br
36	^{94}Kr ^{95}Kr ^{96}Kr ^{97}Kr ^{98}Kr
37	^{99}Rb ^{100}Rb
38	^{102}Sr ^{103}Sr
39	^{100m}Y ^{101}Y ^{102}Y ^{102m}Y ^{103}Y ^{104}Y ^{105}Y
40	^{103}Zr ^{104}Zr ^{105}Zr ^{106}Zr ^{107}Zr ^{108}Zr
41	^{104}Nb ^{105}Nb ^{106}Nb ^{107}Nb ^{108}Nb ^{109}Nb ^{110}Nb ^{112}Nb
42	^{106}Mo ^{107}Mo ^{108}Mo ^{109}Mo ^{111}Mo ^{112}Mo ^{113}Mo
43	^{109}Tc ^{110}Tc ^{111}Tc ^{112}Tc ^{113}Tc ^{114}Tc ^{115}Tc ^{116}Tc

Atomic number (Z)	Isotopes
44	^{111}Ru ^{112}Ru ^{114}Ru ^{115}Ru ^{116}Ru ^{117}Ru ^{118}Ru
45	^{112}Rh ^{114}Rh ^{115}Rh ^{116}Rh ^{117}Rh ^{118}Rh ^{119}Rh ^{120}Rh ^{121}Rh
46	^{115}Pd ^{115m}Pd ^{117}Pd ^{119}Pd ^{120}Pd ^{121}Pd ^{122}Pd ^{123}Pd ^{124}Pd
47	^{118}Ag ^{119m}Ag ^{120}Ag ^{122m}Ag ^{123}Ag ^{124}Ag ^{125}Ag ^{126}Ag ^{127}Ag ^{128}Ag
48	^{124}Cd ^{126}Cd ^{127}Cd ^{128}Cd ^{129}Cd ^{131}Cd ^{132}Cd
49	^{113}In ^{134}In
50	^{131}Sn ^{131m}Sn ^{135}Sn ^{136}Sn ^{137}Sn
51	^{129m}Sb ^{136}Sb ^{137}Sb ^{138}Sb ^{139}Sb
52	^{137}Te ^{138}Te ^{139}Te ^{140}Te ^{141}Te ^{142}Te
53	^{140}I ^{141}I ^{142}I ^{143}I ^{144}I
54	^{142}Xe ^{143}Xe ^{144}Xe ^{145}Xe ^{146}Xe ^{147}Xe
55	^{144}Cs ^{146}Cs ^{148}Cs ^{149}Cs
56	^{148}Ba ^{149}Ba ^{150}Ba ^{151}Ba ^{152}Ba
57	^{149}La ^{150}La ^{151}La ^{152}La ^{153}La ^{154}La
58	^{149}Ce ^{150}Ce ^{151}Ce ^{152}Ce ^{153}Ce ^{154}Ce ^{155}Ce ^{156}Ce
59	^{153}Pr ^{15}4Pr ^{155}Pr ^{156}Pr ^{157}Pr
60	^{156}Nd ^{157}Nd ^{158}Nd ^{159}Nd ^{160}Nd
61	^{152n}Pm ^{158}Pm ^{159}Pm ^{160}Pm ^{161}Pm

Atomic number (Z)	Isotopes
62	^{160}Sm ^{161}Sm ^{162}Sm ^{163}Sm
63	^{160}Eu ^{161}Eu ^{162}Eu ^{163}Eu ^{164}Eu ^{165}Eu
64	^{163}Gd ^{164}Gd ^{165}Gd ^{166}Gd ^{167}Gd
65	^{166}Tb ^{167}Tb ^{168}Tb ^{169}Tb
67	^{171}Ho

APPENDIX C

AN EXAMPLE OF AP1000 REACTOR CORE MCNP INPUT FILE

```
Westinghouse AP1000 17x17 Fuel Assembly
c cell card
1 1 -10.96 -1               u=1 vol=224.88 imp:n=1  $ Second-cycle fuel
2 2 -0.001598 1 -2          u=1 imp:n=1 $ He-4
3 3 -6.56 2 -3              u=1 imp:n=1 $ clad
4 4 -0.7194 3               u=1 imp:n=1 $ water in fuel pin
5 3 -6.56 4 -5              u=7 imp:n=1 $ Guide/Instrument tube
6 4 -0.7194 -4              u=7 imp:n=1 $ water in tube
7 4 -0.7194 5               u=7 imp:n=1 $ water outside tube
8 4 -0.7194 -16             u=6 imp:n=1 $ edge water
9 0 12 -13 14 -15           u=10 fill=100 imp:n=1 $ assembly
10 0 6 -7 8 -9              lat=1 u=100 imp:n=1 $ fuel pin cell lattice
     fill=-9:9 -9:9 0:0
     6 18R
     6 1 1 1 1 1 1 1 1 1 1 1 1 1 1 1 1 1 6
     6 1 1 1 1 1 1 1 1 1 1 1 1 1 1 1 1 1 6
     6 1 1 1 1 1 7 1 1 7 1 1 7 1 1 1 1 1 6
     6 1 1 1 7 1 1 1 1 1 1 1 1 1 7 1 1 1 6
     6 1 1 1 1 1 1 1 1 1 1 1 1 1 1 1 1 1 6
     6 1 1 7 1 1 7 1 1 7 1 1 7 1 1 7 1 1 6
     6 1 1 1 1 1 1 1 1 1 1 1 1 1 1 1 1 1 6
     6 1 1 1 1 1 1 1 1 1 1 1 1 1 1 1 1 1 6
     6 1 1 7 1 1 7 1 1 7 1 1 7 1 1 7 1 1 6
     6 1 1 1 1 1 1 1 1 1 1 1 1 1 1 1 1 1 6
     6 1 1 1 1 1 1 1 1 1 1 1 1 1 1 1 1 1 6
     6 1 1 7 1 1 7 1 1 7 1 1 7 1 1 7 1 1 6
     6 1 1 1 1 1 1 1 1 1 1 1 1 1 1 1 1 1 6
     6 1 1 1 7 1 1 1 1 1 1 1 1 1 7 1 1 1 6
     6 1 1 1 1 1 7 1 1 7 1 1 7 1 1 1 1 1 6
     6 1 1 1 1 1 1 1 1 1 1 1 1 1 1 1 1 1 6
     6 1 1 1 1 1 1 1 1 1 1 1 1 1 1 1 1 1 6
     6 18R
11 5 -10.96 -1              u=2 vol=224.88 imp:n=1  $ first-cycle fuel
12 2 -0.001598 1 -2         u=2 imp:n=1 $ He-4
13 3 -6.56 2 -3             u=2 imp:n=1 $ clad
14 4 -0.7194 3              u=2 imp:n=1 $ water in fuel pin
15 0 12 -13 14 -15          u=20 fill=200 imp:n=1 $ assembly
16 0 6 -7 8 -9              lat=1 u=200 imp:n=1 $ fuel pin cell lattice
     fill=-9:9 -9:9 0:0
     6 18R
     6 2 2 2 2 2 2 2 2 2 2 2 2 2 2 2 2 2 6
     6 2 2 2 2 2 2 2 2 2 2 2 2 2 2 2 2 2 6
     6 2 2 2 2 2 7 2 2 7 2 2 7 2 2 2 2 2 6
     6 2 2 2 7 2 2 2 2 2 2 2 2 2 7 2 2 2 6
     6 2 2 2 2 2 2 2 2 2 2 2 2 2 2 2 2 2 6
     6 2 2 7 2 2 7 2 2 7 2 2 7 2 2 7 2 2 6
     6 2 2 2 2 2 2 2 2 2 2 2 2 2 2 2 2 2 6
     6 2 2 2 2 2 2 2 2 2 2 2 2 2 2 2 2 2 6
     6 2 2 7 2 2 7 2 2 7 2 2 7 2 2 7 2 2 6
     6 2 2 2 2 2 2 2 2 2 2 2 2 2 2 2 2 2 6
     6 2 2 2 2 2 2 2 2 2 2 2 2 2 2 2 2 2 6
```

```
     6 2 2 7 2 2 7 2 2 7 2 2 7 2 2 7 2 2 6
     6 2 2 2 2 2 2 2 2 2 2 2 2 2 2 2 2 2 6
     6 2 2 2 7 2 2 2 2 2 2 2 2 2 7 2 2 2 6
     6 2 2 2 2 2 7 2 2 7 2 2 7 2 2 2 2 2 6
     6 2 2 2 2 2 2 2 2 2 2 2 2 2 2 2 2 2 6
     6 2 2 2 2 2 2 2 2 2 2 2 2 2 2 2 2 2 6
     6 18R
17 6 -10.96 -1                  u=3 vol=224.88 imp:n=1  $ fresh fuel
18 2 -0.001598 1 -2             u=3 imp:n=1 $ He-4
19 3 -6.56 2 -3                 u=3 imp:n=1 $ clad
20 4 -0.7194 3                  u=3 imp:n=1 water in fuel pin
21 0 12 -13 14 -15              u=30 fill=300 imp:n=1 $ assembly
22 0 6 -7 8 -9                  lat=1 u=300 imp:n=1 $ fuel pin cell lattice
     fill=-9:9 -9:9 0:0
     6 18R
     6 3 3 3 3 3 3 3 3 3 3 3 3 3 3 3 3 3 6
     6 3 3 3 3 3 3 3 3 3 3 3 3 3 3 3 3 3 6
     6 3 3 3 3 3 7 3 3 7 3 3 7 3 3 3 3 3 6
     6 3 3 3 7 3 3 3 3 3 3 3 3 3 7 3 3 3 6
     6 3 3 3 3 3 3 3 3 3 3 3 3 3 3 3 3 3 6
     6 3 3 7 3 3 7 3 3 7 3 3 7 3 3 7 3 3 6
     6 3 3 3 3 3 3 3 3 3 3 3 3 3 3 3 3 3 6
     6 3 3 3 3 3 3 3 3 3 3 3 3 3 3 3 3 3 6
     6 3 3 7 3 3 7 3 3 7 3 3 7 3 3 7 3 3 6
     6 3 3 3 3 3 3 3 3 3 3 3 3 3 3 3 3 3 6
     6 3 3 3 3 3 3 3 3 3 3 3 3 3 3 3 3 3 6
     6 3 3 7 3 3 7 3 3 7 3 3 7 3 3 7 3 3 6
     6 3 3 3 3 3 3 3 3 3 3 3 3 3 3 3 3 3 6
     6 3 3 3 7 3 3 3 3 3 3 3 3 3 7 3 3 3 6
     6 3 3 3 3 3 7 3 3 7 3 3 7 3 3 3 3 3 6
     6 3 3 3 3 3 3 3 3 3 3 3 3 3 3 3 3 3 6
     6 3 3 3 3 3 3 3 3 3 3 3 3 3 3 3 3 3 6
     6 18R
99 4 -0.7194 -1000              u=101 imp:n=1 $  water
c Reactor Pressure Vessels
101  0 -100 -101 10 -11 -112 fill=13 imp:n=1  $ RPV outer
33 0 12 -13 14 -15              lat=1 u=13 imp:n=1 $ fuel pin cell lattice
     fill=0:8 0:8 0:0 $
       10 20 10 20 10 20 10 30 101
       20 10 20 10 20 10 30 30 101
       10 20 10 20 10 20 30 101 101
       20 10 20 10 20 30 30 101 101
       10 20 10 20 10 30 101 2R
       20 10 20 30 30 101 3R
       10 30 30 30 101 4R
       30 30 101 6R
       101 8R
102  4 -0.7194 -100 -101 11 -111 -112 imp:n=1 $ top water
103  4 -0.7194 -100 -101 -10 110 -112 imp:n=1 $ bottom water
104  7 -8.000 -100 -101 110 -111 112 -113 imp:n=1 $ barrel
100 0 (100:101:-110:111:113) imp:n=0 $ outside

c surface card
c fuel rod
1 cz 0.409575        $ fuel radius
2 cz 0.41775         $ clad in
3 cz 0.47475         $ clad out
4 cz 0.56134         $ Guide/Instrument tube in
5 cz 0.61214         $ Guide/Instrument tube out
```

```
6 px -0.63          $ left x boundary of the pin water (fuel pitch)
7 px  0.63          $ right x boundary of the pin water (fuel pitch)
8 py -0.63          $ left y boundary of the pin water (fuel pitch)
9 py  0.63          $ right y boundary of the pin water (fuel pitch)
10 pz -213.36       $ Fuel rod lenth
11 pz  213.36       $ Fuel rod length
12 px -10.71        $ assembly pitch not assembly size
13 px 10.71         $ assembly pitch not assembly size
14 py -10.71        $ assembly pitch not assembly size
15 py 10.71         $ assembly pitch not assembly size
16 cz 100           $ big cylinder
c Quarter of the core
*100   PX      0             $ Plane at x = 0 (reflective)
*101   PY      0             $ Plane at y = 0 (reflective)
110    PZ   -240             $ vessel height
111    PZ    240             $ vessel height
112    CZ    169.8625        $ Reator Vessel ID
113    CZ    174.9425        $ Reator Vessel OD
1000 cz 200                  $ water fill

c data card
mode n
mphys on
kcode 10000 1.3 50 250
ksrc -3.8043 -5.0287 0 -25.2243 -5.0287 0 -46.6443 -5.0287 0
        -68.0643 -5.0287 0 -89.4843 -5.0287 0
        -110.9043 -5.0287 0 -132.3243 -5.0287 0
        -153.7443 -5.0287 0 -3.8043 -26.4487 0
        -25.2243 -26.4487 0 -46.6443 -26.4487 0
        -68.0643 -26.4487 0 -89.4843 -26.4487 0
        -110.9043 -26.4487 0 -132.3243 -26.4487 0
        -153.7443 -26.4487 0 -3.8043 -47.8687 0
        -25.2243 -47.8687 0 -46.6443 -47.8687 0
        -68.0643 -47.8687 0 -89.4843 -47.8687 0
        -110.9043 -47.8687 0 -132.3243 -47.8687 0
        -3.8043 -69.2887 0 -25.2243 -69.2887 0
        -46.6443 -69.2887 0 -68.0643 -69.2887 0
        -89.4843 -69.2887 0 -110.9043 -69.2887 0
        -132.3243 -69.2887 0 -3.8043 -90.7087 0
        -25.2243 -90.7087  0 -46.6443 -90.7087  0
        -68.0643 -90.7087 0 -89.4843 -90.7087  0
        -110.9043 -90.7087  0 -3.8043 -112.1287 0
        -25.2243 -112.1287 0 -46.6443 -112.1287 0
        -68.0643 -112.1287 0 -89.4843 -112.1287 0
        -3.8043 -133.5487 0 -25.2243 -133.5487 0
        -46.6443 -133.5487 0 -68.0643 -133.5487 0
        -3.8043 -154.9687 0 -25.2243 -154.9687 0
BURN TIME = 0.3, 0.3, 0.4, 4, 25, 40 11r
         PFRAC = 1.0 16r
         POWER= 850
         MAT= 1, 5, 6
         MATVOL = 786630.24, 771788.16, 771788.16
         AFMIN = 1E-10 1E-10
         BOPT= 1.0 -24 1.0
c  157 Assemblies for AP 1000. 3400MWth/4 assemblies = 850 MWth.
m1 8016.82c -1.185E-01 90230.82c -8.511E-10
       92233.82c -2.195E-09 92234.82c -1.561E-04 92235.82c -1.008E-02
       92236.82c -3.220E-03 92237.82c -6.143E-06 92238.82c -8.363E-01
       92239.82c -4.549E-07 93236.82c -6.979E-10 93237.82c -2.558E-04
```

```
      93238.82c -6.800E-07 93239.82c -6.557E-05 94238.82c -6.453E-05
      94239.82c -5.240E-03 94240.82c -1.415E-03 94241.82c -8.534E-04
      94242.82c -2.057E-04 94243.82c -4.766E-08 94244.82c -3.444E-09
      95241.82c -2.038E-05 95242.82c -1.211E-07 95243.82c -2.605E-05
      95244.82c -1.700E-08 96242.82c -4.899E-06 96243.82c -6.926E-08
      96244.82c -5.150E-06 96245.82c -1.790E-07 96246.82c -8.658E-09 $ Second-cycle fuel
m2 2004.81c -1.0 $He-4 density: 0.001598g/cc, 600K
m3 8016.81c -0.0012 26054.81c -0.0000585
      26056.81c -0.0009175 26057.81c -0.0000212 26058.81c -0.0000028
      40090.81c -0.504776 40091.81c -0.110079 40092.81c -0.168259
      40094.81c -0.170515 40096.81c -0.027471 41093.81c -0.01
      50112.81c -0.00006499 50114.81c -0.00004422 50115.81c -0.00002278
      50116.81c -0.00097418 50117.81c -0.00051456 50118.81c -0.00162274
      50119.81c -0.00057553 50120.81c -0.00218286 50122.81c -0.00031021
      50124.81c -0.00038793 $ZIRLO=TM, 600K
m4 1001.81c -0.111894 8016.81c -0.888106 $Pressurized water, 600K
mt4 LWTR.01t
m5 8016.82c -1.186E-01 90230.82c -4.707E-10
      92233.82c -2.112E-09 92234.82c -1.703E-04 92235.82c -1.283E-02
      92236.82c -2.820E-03 92237.82c -8.650E-06 92238.82c -8.397E-01
      92239.82c -7.345E-07 93236.82c -4.777E-10 93237.82c -1.821E-04
      93238.82c -7.667E-07 93239.82c -1.057E-04 94238.82c -3.537E-05
      94239.82c -4.948E-03 94240.82c -1.146E-03 94241.82c -6.234E-04
      94242.82c -1.110E-04 $ First-cycle fuel
m6 8016.82c -0.118502 92234.82c -0.000235 92235.82c -0.029089
      92238.82c -0.852174  $ Fresh-fuel
m7 6012.81c -0.00039572 6013.81c -0.00000428 14028.81c -0.00461
      14029.81c -0.000235 14030.81c -0.000155 15031.81c -0.000230
      16032.81c -0.000132986 16033.81c -0.00000105 16034.81c -0.00000595
      16036.81c -0.000000014 24050.81c -0.0082555 24052.81c -0.1591991
      24053.81c -0.0180519 24054.81c -0.0044935 25055.81c -0.01
      26054.81c -0.041051205 26056.81c -0.643837275 26057.81c -0.014876676
      26058.81c -0.001964844 28058.81c -0.0629703 28060.81c -0.024256275
      28061.81c -0.0010545 28062.81c -0.003362375 28064.81c -0.00085655 $ SS 304
```

APPENDIX D

AN EXAMPLE OF CEνNS RESPONSE MODELING CODE

```
% Reaction Rate
% Detector Weight
mdetector = 100 *1e3; % kg to gram
NA=6.022e23;

% Atom density Ge70, Ge72, Ge73, Ge74 and Ge76 and (cm-3)
M_Ge70=69.924248757;
N_Ge70=0.2057*mdetector*NA/M_Ge70;
M_Ge72=71.922076084;
N_Ge72=0.2745*mdetector*NA/M_Ge72;
M_Ge73=72.923459215;
N_Ge73=0.0775*mdetector*NA/M_Ge73;
M_Ge74=73.921178037;
N_Ge74=0.3650*mdetector*NA/M_Ge74;
M_Ge76=75.921402756;
N_Ge76=0.0773*mdetector*NA/M_Ge76;

% Distance of detector from core
% m to cm
r=10 * 1E2;

% Fission Faction (FF) for each actinide
% U235, U238, Pu239, Pu241, and U239_capture are antineutrino spectrums
flux_U235         = U235.*U235FF.*(fission)./(4*pi*r*r);
flux_U238         = U238.*U238FF.*(fission)./(4*pi*r*r);
flux_Pu239        = Pu239.*Pu239FF.*(fission)./(4*pi*r*r);
flux_Pu241        = Pu241.*Pu241FF.*(fission)./(4*pi*r*r);
flux_U238_capture = U238_capture.*CaptureFF.*(fission)./(4*pi*r*r);

flux_total=(flux_U235+flux_U238+flux_Pu239+flux_Pu241+flux_U238_capture);
flux_total1=sum(flux_total,2)*0.01;

% Reaction Rate (R) for detector (Events/day)
%Germanium
R_Ge70=N_Ge70*sigma_Ge70.*flux_total*(1e-38)*86400;
R_Ge70(isnan(R_Ge70))=0;
R_Ge72=N_Ge72*sigma_Ge72.*flux_total*(1e-38)*86400;
R_Ge72(isnan(R_Ge72))=0;
R_Ge73=N_Ge73*sigma_Ge73.*flux_total*(1e-38)*86400;
R_Ge73(isnan(R_Ge73))=0;
R_Ge74=N_Ge74*sigma_Ge74.*flux_total*(1e-38)*86400;
R_Ge74(isnan(R_Ge74))=0;
R_Ge76=N_Ge76*sigma_Ge76.*flux_total*(1e-38)*86400;
R_Ge76(isnan(R_Ge76))=0;

R_Ge=(R_Ge70)+(R_Ge72)+(R_Ge73)+(R_Ge74)+(R_Ge76);
R_Ge_total=sum(R_Ge,2)*0.01;
```

APPENDIX E

AN EXAMPLE OF ANTINEUTRINO SPECTRUM MODELING CODE

```
% antineutrino spectrum Modeling
% Written by: Wei Eng Ang

% Energy bin 1 keV
E_v=0.01:0.01:14;
E_v1=repmat(E_v,1064,1);

% Calculate endpoint energy, E_beta
E_beta=Q+0.511;

% calculate total energy Ev for each Q value
Ev=E_v1;
Ev(E_v1>E_beta)=0;

% Calculate momentum
D=(E_beta-Ev).^2-0.511^2;
D( D<0 | ~Ev)=0;
p=sqrt(D);

% Calculate Fermi Function
% Structure Constant
alpha=(1/137);

% Gamma constant
gam=sqrt(1-((alpha*Z).^2));

% Radius
R=1.2*(A.^(1/3))*(1E-15);

% Convert meter to 1/MeV
R1=(5.076E12*R);

% y
y=alpha*Z.*(E_beta-Ev)./p;
y(~p)=0;

% Fermi function
Fermi= 4 * (2*p.*R1).^(-2+2*gam) .* (abs(gammai(gam+i*y)./gammai(2*gam+1)).^2) .* (exp(pi*y));
Fermi(~p)=0;
toc;

% Finite Size Correction
FS=(-8/5)*(Z.*alpha.*R1.*(E_beta-Ev)).*(1+(9/28)*((0.511^2)./((E_beta-Ev).^2)));

% Weak magnetism
WM=0.005*(E_beta-Ev);

% QED correction / Radiative correction
beta = p./(E_beta-Ev);
QED1 = (2*beta)./ (1+beta);
QED1(isnan(QED1))=0;
```

```
% dilog calculation
Li=mydilog(QED1);

abeta = atanh(beta);
hv= 3*log(938.272/0.511)+(23/4)-((8./beta).*Li)+((8)*((abeta./beta)-1).*log((2*(E_beta-
Ev).*beta)./0.511))+((4*abeta./beta).*(((7+(3*(beta.^2)))./8)-(2*abeta)));
hv(isnan(hv))=0;

QED2=alpha / (2*pi) * hv;

% Calculation of Antineutrino Spectrum
n1=p.*(Ev.^2).*(E_beta-Ev).*Fermi.*(1+FS+WM+QED2);
 n1(isnan(n1))=0;

% Integration
n2=n1*0.01;

% Normalized Antineutrino Spectrum with cumulative Yield (CY) and Transitions (P)
M=sum(n1,2);
n3=n1./M.*CY.*P;
n3(isnan(n3))=0;

% Calculation of Antineutrino Spectrum
n1=p.*(Ev.^2).*(E_beta-Ev).*Fermi;
 n1(isnan(n1))=0;

% Integration
n2=n1*0.01;

% Normalized Antineutrino Spectrum with cumulative Yield (CY) and Beta intensities (P)
M=sum(n1,2);
n3=n1./M.*CY.*P;
n3(isnan(n3))=0;
```

APPENDIX F

AN EXAMPLE OF PULSE HEIGHT DISTRIBUTION CODE

```
%Fermi Constant
Fermi = 1.1664E-5;

%Germanium
%Ge70
A_Ge70 = 70;
Z_Ge70 = 32;
N_Ge70 = A_Ge70 - Z_Ge70;
m_A_Ge70 = A_Ge70 * 931.5 * 1e-3;
qv_Ge70=(0.0298*Z_Ge70)-(0.5117*N_Ge70);
A1_Ge70=(Fermi*Fermi*qv_Ge70*qv_Ge70*m_A_Ge70)/(2*pi);

%Ge72
A_Ge72 = 72;
Z_Ge72 = 32;
N_Ge72 = A_Ge72 - Z_Ge72;
m_A_Ge72 = A_Ge72 * 931.5 * 1e-3;
qv_Ge72=(0.0298*Z_Ge72)-(0.5117*N_Ge72);
A1_Ge72=(Fermi*Fermi*qv_Ge72*qv_Ge72*m_A_Ge72)/(2*pi);

%Ge73
A_Ge73 = 73;
Z_Ge73 = 32;
N_Ge73 = A_Ge73 - Z_Ge73;
m_A_Ge73 = A_Ge73 * 931.5 * 1e-3;
qv_Ge73=(0.0298*Z_Ge73)-(0.5117*N_Ge73);
A1_Ge73=(Fermi*Fermi*qv_Ge73*qv_Ge73*m_A_Ge73)/(2*pi);

%Ge74
A_Ge74 =74;
Z_Ge74 = 32;
N_Ge74 = A_Ge74 - Z_Ge74;
m_A_Ge74 = A_Ge74 * 931.5 * 1e-3;
qv_Ge74=(0.0298*Z_Ge74)-(0.5117*N_Ge74);
A1_Ge74=(Fermi*Fermi*qv_Ge74*qv_Ge74*m_A_Ge74)/(2*pi);

%Ge76
A_Ge76 = 76;
Z_Ge76 = 32;
N_Ge76 = A_Ge76 - Z_Ge76;
m_A_Ge76 = A_Ge76 * 931.5 * 1e-3;
qv_Ge76 =(0.0298*Z_Ge76)-(0.5117*N_Ge76);
A1_Ge76=(Fermi*Fermi*qv_Ge76*qv_Ge76*m_A_Ge76)/(2*pi);

E_nu=(0.01:0.01:14)*1e-3;                    % in GeV
E_nu2 = reshape(E_nu',[],1);
TR_Ge = (1:1:6020);                          % in eV
TR_Ge1 = repmat(TR_Ge,1400,1);
```

```
%Maximum recoil energy
%GeV to eV
Tr_Ge70=(2.0*E_nu2.*E_nu2)./(m_A_Ge70 + 2*E_nu2)*1E9;
Tr_Ge72=(2.0*E_nu2.*E_nu2)./(m_A_Ge72 + 2*E_nu2)*1E9;
Tr_Ge73=(2.0*E_nu2.*E_nu2)./(m_A_Ge73 + 2*E_nu2)*1E9;
Tr_Ge74=(2.0*E_nu2.*E_nu2)./(m_A_Ge74 + 2*E_nu2)*1E9;
Tr_Ge76=(2.0*E_nu2.*E_nu2)./(m_A_Ge76 + 2*E_nu2)*1E9;

% Natural Germanium
% Conversion GeV^-3 to cm2/eV
dsigmadTGe70 = ((Fermi*Fermi*m_A_Ge70)/(2*pi))* ((qv_Ge70^2) + (qv_Ge70^2) * ((1- (TR1_Ge70*1E-
9)./E_nu2).^2) - ((m_A_Ge70*TR1_Ge70*1E-9*qv_Ge70^2)./(E_nu2.^2)));
dsigmadTGe70(~TR1_Ge70)=0;
dsigmadTGe72 = ((Fermi*Fermi*m_A_Ge72)/(2*pi))* ((qv_Ge72^2) + (qv_Ge72^2) * ((1- (TR1_Ge72*1E-
9)./E_nu2).^2) - ((m_A_Ge72*TR1_Ge72*1E-9*qv_Ge72^2)./(E_nu2.^2)));
dsigmadTGe72(~TR1_Ge72)=0;
dsigmadTGe73 = ((Fermi*Fermi*m_A_Ge73)/(2*pi))* ((qv_Ge73^2) + (qv_Ge73^2) * ((1- (TR1_Ge73*1E-
9)./E_nu2).^2) - ((m_A_Ge73*TR1_Ge73*1E-9*qv_Ge73^2)./(E_nu2.^2)));
dsigmadTGe73(~TR1_Ge73)=0;
dsigmadTGe74 = ((Fermi*Fermi*m_A_Ge74)/(2*pi))* ((qv_Ge74^2) + (qv_Ge74^2) * ((1- (TR1_Ge74*1E-
9)./E_nu2).^2) - ((m_A_Ge74*TR1_Ge74*1E-9*qv_Ge74^2)./(E_nu2.^2)));
dsigmadTGe74(~TR1_Ge74)=0;
dsigmadTGe76 = ((Fermi*Fermi*m_A_Ge76)/(2*pi))* ((qv_Ge76^2) + (qv_Ge76^2) * ((1- (TR1_Ge76*1E-
9)./E_nu2).^2) - ((m_A_Ge76*TR1_Ge76*1E-9*qv_Ge76^2)./(E_nu2.^2)));
dsigmadTGe76(~TR1_Ge76)=0;

%Background and Threshold %%%%%
mass = 100; %kg
DRU =100 ;
BG= DRU*mass/1000 ;
THRESHOLD_Ge=100; %eV

%Burnup
% 1=0GWD, 2=10GWD, 3=20GWD, 4=30GWD, 5=40GWD, 6=50GWD, 7=60GWD
BURNUP=1;
BG_Ge=repmat(BG,1,6020);

%transpose Cross-Section
sigma_Ge70_1 = transpose(sigma_Ge70);
sigma_Ge72_1 = transpose(sigma_Ge72);
sigma_Ge73_1 = transpose(sigma_Ge73);
sigma_Ge74_1 = transpose(sigma_Ge74);
sigma_Ge76_1 = transpose(sigma_Ge76);

%Probability of recoil energy for given antineutrino energy
dsigmadTdEGe70=dsigmadT1Ge70./(sigma_Ge70_1);
dsigmadTdEGe70_1=dsigmadTdEGe70./sum(dsigmadTdEGe70,2);
dsigmadTdEGe72=dsigmadT1Ge72./(sigma_Ge72_1);
dsigmadTdEGe72_1=dsigmadTdEGe72./sum(dsigmadTdEGe72,2);
dsigmadTdEGe73=dsigmadT1Ge73./(sigma_Ge73_1);
dsigmadTdEGe73_1=dsigmadTdEGe73./sum(dsigmadTdEGe73,2);
dsigmadTdEGe74=dsigmadT1Ge74./(sigma_Ge74_1);
dsigmadTdEGe74_1=dsigmadTdEGe74./sum(dsigmadTdEGe74,2);
dsigmadTdEGe76=dsigmadT1Ge76./(sigma_Ge76_1);
dsigmadTdEGe76_1=dsigmadTdEGe76./sum(dsigmadTdEGe76,2);
dsigmadTdEGe76=dsigmadT1Ge76./(sigma_Ge76_1);
dsigmadTdEGe76_1=dsigmadTdEGe76./sum(dsigmadTdEGe76,2);
dsigmadTdENatGe=dsigmadT1NatGe./(sigma_naturalGe_1);
dsigmadTdENatGe_1=dsigmadTdENatGe./sum(dsigmadTdENatGe,2);
```

```
%Pulse Height Distribution
%Germanium
R_Ge70_1= transpose(R_Ge70);
R_Ge72_1= transpose(R_Ge72);
R_Ge73_1= transpose(R_Ge73);
R_Ge74_1= transpose(R_Ge74);
R_Ge76_1= transpose(R_Ge76);

PHD_Ge70= dsigmadTdEGe70_1.*R_Ge70_1(:,BURNUP)*0.01;
PHD_Ge72= dsigmadTdEGe72_1.*R_Ge72_1(:,BURNUP)*0.01;
PHD_Ge73= dsigmadTdEGe73_1.*R_Ge73_1(:,BURNUP)*0.01;
PHD_Ge74= dsigmadTdEGe74_1.*R_Ge74_1(:,BURNUP)*0.01;
PHD_Ge76= dsigmadTdEGe76_1.*R_Ge76_1(:,BURNUP)*0.01;

PHD_Ge= PHD_Ge70+PHD_Ge72+PHD_Ge73+PHD_Ge74+PHD_Ge76;
PHD_Ge(isnan(PHD_Ge))=0;
PHD_Ge_sum= sum(PHD_Ge,1);
Final_PHD_Ge_gross = sum(PHD_Ge_sum,2);
PHD_Ge_BG = max(PHD_Ge_sum-BG_Ge,0);
Final_PHD_Ge_BG = sum(PHD_Ge_BG,2);
PHD_Ge_BG_Threshold = PHD_Ge_BG;
PHD_Ge_BG_Threshold(1:THRESHOLD_Ge)=0;
Final_PHD_Ge_BG_Threshold = sum(PHD_Ge_BG_Threshold,2);
```